Electronic structure of TiO_2-based photocatalysts active under visible light

A thesis submitted to the University of Oxford
for the degree of Doctor of Philosophy

Freddy Enrique Oropeza Palacio

Trinity Term 2011

Inorganic Chemistry Laboratory
Department of Chemistry

Pembroke College, University of Oxford

Dedicada a mi familia y la memoria de mi padre

Abstract

Electronic structure of TiO_2-based photocatalysts active under visible light

This thesis is concerned with furthering our understanding of the basis of visible region photocatalytic activity exhibited by doped TiO_2-based materials. A range of experimental techniques including high resolution X-ray photoemission spectroscopy and diffuse reflectance spectroscopy are used to investigate electronic structure and an attempt is made to link these results to the observed photocatalytic activity. Both anionic (N) and cationic (Rh and Sn) dopants are investigated.

Chapter 1 introduces the field of photocatalysis and considers strategies for inducing visible region photoactivity in doped TiO_2-based materials. Chapter 2 deals with the background to the range of experimental techniques used in the thesis, whilst chapter 3 describes the apparatus and methodologies employed in the subsequent experimental chapters 4 to 8.

Chapter 4 presents a critical re-evaluation of the mode of incorporation of N in doped TiO_2. A range of sol-gel synthesis conditions were used to prepare high area N-doped TiO_2 in the anatase phase. Bulk N doping levels were determined by an inert gas fusion method and were compared with surface N doping levels determined by x-ray photoelectron spectroscopy. Comparison was also made with the concentration of paramagnetic species measured by electron spin resonance spectroscopy. It was found that both surface and bulk doping levels were typically around 3 orders of magnitude higher than the concentration of paramagnetic N-containing species. All N-doped samples showed higher visible region (λ>395 nm) photocatalytic activity than undoped anatase itself. It is argued that catalytic activity is associated with the presence of nitrogen bound to lattice oxygen to give $(NO)_O^{'}$.

Chapter 5 explores the influence of antimony co-doping on the electronic structure of rhodium-doped rutile TiO_2 using X-ray photoemission spectroscopy (XPS) to explore the density of electronic states. Rh doping leads to the appearance of new Rh 4*d* electronic states just above the top of the O 2*p* valence band in XPS and the Fermi level shifts down from a position close to the conduction band minimum in undoped TiO_2 to just above the new Rh 4*d* band in rhodium doped TiO_2. Sb co-doping restores the Fermi level to its original position. These changes indicate a change in valence state from t_{2g}^5 Rh(IV) to t_{2g}^6 Rh(III) upon Sb co-doping.

Abstract

In chapter 6 the electronic and structural properties of dilute solid solutions of SnO_2 in TiO_2 prepared by conventional high-temperature solid state synthesis have been investigated. Samples of $Sn_xTi_{1-x}O_2$ with $0.0<x<0.1$ (i.e. 0 % to 10% Sn doping) were prepared by solid state reaction of SnO_2 and TiO_2 powders at 1200°C followed by rapid quenching. Narrowing of the bandgap at low Sn doping level was observed through both diffuse reflectance spectroscopy and valence band photoemission spectroscopy and we also observed surface states in the bulk bandgap associated with segregated Sn^{2+} cations.

The study of Sn doped TiO_2 is extended in chapter 7 where the influence of Sn doping on the anatase-to-rutile phase transition has is investigated in high area powders prepared by a sol-gel route involving alkoxide precursors. Sn doping facilitates conversion of anatase to rutile at lower temperatures than is observed for undoped material. At the same time Sn-doping inhibits sintering as gauged by line widths in X-ray diffraction and gas-adsorption surface area measurements. These observations are linked to the finding of pronounced segregation of Sn to the surface of rutile TiO_2 observed in X-ray photoemission spectra. Sn-doped TiO_2 is found to exhibit enhanced visible region photocatalytic activity as compared with undoped material in dye degradation experiments. This is attributed to narrowing of the bulk bandgap at low doping levels coupled with the introduction of surface states associated with segregated Sn ions in the divalent state similar to those seen in chapter 6.

The final experimental chapter 8 shows that the anatase phase of TiO_2 may be stabilised in epitaxial thin films grown on $SrTiO_3$(001) by a simple sol gel-route owing to the better lattice match of anatase with the substrate as compared with the match for the rutile phase. This allows preparation of highly crystalline Sn-doped anatase-TiO_2 thin films. In contrast to the behaviour found for Sn-doped rutile TiO_2, Sn doping leads to a monotonic increase in the bandgap.

The final chapter 9 presents an overview of the results and discusses the scope for further work in this area.

Freddy E. Oropeza Palacio

Acknowledgements

First of all I gratefully thank my supervisor, Professor Russell Egdell, for his constant help, encouragement and clever support not only in all matters related to the work presented in this thesis, but also in the development of my professional career. His ideas on how research is done made my D. Phil. experience productive and stimulating.

Secondly I would especially like to thank Dr. Robert Palgrave who helped supervise me on a day to day basis during the first year of my D. Phil. and Dr. David Payne who initiated me into the mysteries of high performance XPS at Daresbury Laboratory, ably assisted by Dr. Danny Law and Dr. Graham Beamson at the NCESS facility. I am also thankful to Dr. Jeff Harmer for help with the EPR experiments and to Dr. Vlado Lazarov for taking the electron microscopy images for me. Finally I am grateful to Dr. Rob Jacobs for his support in the use of the facilities of the in the surface analysis laboratory.

I must also acknowledge the support of my fellow D. Phil. student Zhang Hong Liang who was always generous with sharing his expertise in AFM and in preparation of thin sections for HRTEM. I would like to thank Part II students Hilni Harunsani and Bethan Davies. Hilni helped me with development of the preparation procedure used to make the solid state samples studied in chapter 6 and with XPS measurements at Daresbury Laboratory, while Bethan worked alongside me on visible region photocatalysis.

I also thank my friends/housemates Eduardo and Wills for their great friendship, support and encouragement throughout my D.Phil time and for having made a cold and poorly insulated house at 12 Chilswell Rd an excellent place to call home.

Por ultimo, pero no menos importante, dedico un par de lineas para agradecer grandemente a mi familia, especialmente Nora, Ernesto, Jesus, Eduardo y mis abuelas Carmen y Aura, por ese cariño incondicional y constante apoyo emocional que resulta de suma importancia cuando se esta fuera de casa, mas aun en esta etapa de mi vida llena de cambios

Publications

Reproduced by permission of the PCCP Owner Societies. Available from: http://doi.org/10.1039/B914733K

1. A critical evaluation of the mode of incorporation of nitrogen in doped anatase photocatalysts.*
   F. E. Oropeza, J. Harmer, R. G. Egdell and R. G. Palgrave
   Physical Chemistry Chemical Physics, 2010, **12**, 960.

Reprinted with permission. Copyright 2010 American Chemical Society. Available from: http://doi.org/10.1021/cm902970u

2. Electronic and structural properties of $Sn_xTi_{1-x}O_2$ ($0.0 \leq x \leq 0.1$) solid solutions.*
   M. H. Harunsani, **F. E. Oropeza**, R. G. Palgrave and R. G. Egdell
   Chemistry of Materials, 2010, **22**, 1551.

Reproduced by permissions of the PCCP Owner Societies. Available from http://doi.org/10.1039/C0CP02639E

3. Synthesis and properties of high area Sn-doped rutile TiO_2 photocatalysts.*
   F. E. Oropeza, B. Davies, R. G. Palgrave and R. G. Egdell
   Physical Chemistry Chemical Physics, 2011, **13**, 7882.

4. Control of valence states in Rh-doped TiO_2 by Sb co-doping: a study by high resolution X-ray photoemission spectroscopy.*
   F. E. Oropeza and R.G. Egdell
   Chemical Physics Letters, 2011, manuscript submitted.

5. Thickness dependence of the properties of epitaxial In_2O_3 thin films grown on Y-stabilised ZrO_2(111).
   K. H. L. Zhang, V. Lazarov, T. D. Veal, **F. E. Oropeza**, C.F. McConville, R.G. Egdell, Aron Walsh and R. Catlow
   Journal of Physics: Condensed Matter, 2011, manuscript accepted.

6. Domain matching epitaxial growth of In_2O_3 thin films on α-Al_2O_3(0001)
   K.H. L. Zhang, V.K. Lazarov, **F. E. Oropeza** and R.G. Egdell
   In preparation.

*These papers report work from this thesis

Contents

	Abstract	i
	Acknowledgements	iii
	Publications	iv
1.	**Introduction**	1
1.1	**Introduction to the challenge of achieving visible region photocatalysis with TiO_2.**	1
1.2	**The structures of the polymorphs of TiO_2.**	2
1.3	**Crystal morphology**	4
1.4	**The anatase to rutile phase transformation**	6
1.5	**Phase stability in doped TiO_2**	7
1.6	**The electronic structure of TiO_2**	9
1.7	**Tuning the band gap of TiO_2 for visible light photocatalysis**	15
1.8	**Scope of the current thesis.**	21
1.9	**References**	25
2.	**Background to experimental techniques**	27
2.1.	**X-ray Photoelectron Spectroscopy (XPS)**	27
2.1.1.	*Electron Mean Free Path and XPS sampling depth.*	30
2.1.2.	*Some fundamental aspects of core electron spectra*	32
	(a) Binding energy in solids: the equivalent core approach	32
	(b) Chemical shifts	33
	(c) Spin-orbit coupling splitting	34
	(d) Intensities	35
2.1.3.	*Some fundamental aspects of valence band electron spectra*	36
2.2.	**Diffuse Reflectance Spectroscopy (DRS)**	38
2.3	**Electron Spin Resonance Spectroscopy.**	41
2.3.1	*General considerations*	41
2.3.2	*Position of the spectrum*	42

2.3.3 Hyperfine structure 43

2.3.4 ESR spectra in the solid state 44

2.4 Raman spectroscopy 47

2.4.1 General considerations 47

2.4.2 Raman scattering by crystalline solids 48

2.5 Atomic Force Microscopy 49

2.5.1 Contact mode AFM 49

2.5.2 Tapping mode AFM 51

2.5.3 Non-contact mode AFM 52

2.6 Powder X-ray diffraction 54

2.7 Transmission Electron Microscopy 56

2.8 Surface area determination by physisorption analysis 58

2.9 Photocatalytic model tests 60

2.10 References 63

3. Experimental Apparatus and Techniques 65

3.1 High resolution X-ray photoelectron spectroscopy 65

3.1.1 Introduction 65

3.1.2 X-ray source: rotating anode and 7-crystal monochromator 67

3.1.3 Analysis chamber 67

3.1.4 ESCA 300 hemispherical analyser and channel plate detection system 68

3.2 UV/visible diffuse reflectance spectroscopy 68

3.3 Electron spin resonance spectroscopy 70

3.4 Raman spectroscopy 70

3.5 Atomic force microscopy 70

3.6 Powder X-ray diffraction 71

3.7 Transmission electron microscopy 71

3.8 Surface area determination by physisorption analysis 72

3.9 Photocatalytic model tests 72

3.10 References 74

4. Evaluation of the mode of incorporation of nitrogen in doped anatase photocatalysts 75

4.1 Introduction 75

4.2 Experimental section 77

4.2.1 Preparation of the solids 77

4.2.2 Characterization 78

4.2.3 Catalytic activity 80

4.3 Results and discussion 81

4.3.1 Crystallinity, particle size and surface area 81

4.3.2 Bulk and surface N doping levels 84

4.3.3 The influence of N doping on electronic structure and the mode of N incorporation. 85

4.3.4 Electron paramagnetic resonance (EPR) spectra 93

4.3.5 Catalytic activity 97

4.4 Conclusions 99

4.5 References 102

5. Control of valence states in Rh-doped TiO_2 by Sb co-doping: a study by high resolution X-ray photoemission spectroscopy. 105

5.1 Introduction 105

5.2 Experimental section 106

5.2.1 Preparation of solids 106

5.2.2 Characterization 106

5.3 Results and discussion 107

5.3.1 X-Ray Diffraction 107

5.3.2 X-ray photoelectron spectroscopy 108

5.3.3 UV/visible spectroscopy 113

5.4 Conclusions 114

5.5 References 116

6. Electronic and structural properties of $Sn_xTi_{1-x}O_2$ ($0.0 \leq x \leq 0.1$) solid solutions 118

6.1 Introduction 118

6.2 Experimental section 120

6.2.1 Preparation of the solids 120

6.2.2 Characterization 120

6.3 Results and discussion 122

6.3.1 X-Ray Diffraction 122

6.3.2 Raman Spectroscopy 124

6.3.3 Optical Band Gap 127

6.3.4 X-ray photoelectron spectroscopy 129

6.4 Conclusions 135

6.5 References 137

7 Electronic properties of high area Sn-doped rutile TiO_2 photocatalysts 140

7.1 Introduction 140

7.2 Experimental Section 141

7.2.1 Samples preparation 141

7.2.2 Characterization 142

7.2.3 Photocatalytic tests 142

7.3 Results and discussion 143

7.3.1 Influence of tin on the rutile to anatase phase transition and powder particle size 143

7.3.2 Sn concentrations on $Sn_xTi_{1-x}O_2$ surfaces 148

7.3.3 The influence of Sn doping on electronic structure 150

(a) Valence band XPS 150

(b) Diffuse reflectance spectra 152

7.3.4 Photocatalytic activity of $Sn_xTi_{1-x}O_2$ solid solutions 154

7. 4 Conclusions 158

7.5 References 160

8. Structural and electronic properties of anatase $Sn_xTi_{1-x}O_2$ films epitaxially grown on $SrTiO_3$ (001) 163

8.1 Introduction 163

8.2 Experimental Section 164

8.2.1 Preparation of the films 164

8.2.2 Characterization 165

8.3 Results and discussion 166

8.3.1 Epitaxial growth of undoped TiO_2 by sol-gel routes 166

8.3.2 Tin incorporation in anatase epitaxial TiO2 174

(a) Characterization of the epitaxial growth 174

(b) Sn concentrations on anatase $Sn_xTi_{1-x}O_2$ surfaces 176

(c) Limits of stabilization of epitaxial anatase 177

8.3.3 The influence of Sn doping on electronic structure of anatase TiO_2: a valence band XPS study 179

8.4 Conclusions 180

8.5 References 183

9 Concluding remarks 185

9.1 Visible light absorption versus visible light photocatalysis 185

9.2 Areas for future work 187

9.3 Reference 191

1. Introduction

1.1 Introduction to the challenge of achieving visible region photocatalysis with TiO_2.

Fossil fuels supply the energy required to sustain the modern world. However, the use of fossil fuel produces CO_2, with associated problems of global warming. In addition, the fact that these sources of energy are non-renewable means that they are destined to run out. This accentuates the need to search for alternative energy sources suitable for the sustenance and development of future generations. The growing international consensus that there must be restrictions in the level of greenhouse gas emissions demands these new sources to be abundant, renewable and clean. These characteristics are met by solar energy. Following the discovery by Fujishima and Honda of the photocatalytic splitting of water on titanium dioxide (TiO_2) electrodes in 1972,[1] heterogeneous photocatalysis, particularly with TiO_2, began to be widely studied as a viable means of exploiting the energy of the sun. Furthermore, in recent years, the application of TiO_2 to environmental cleanup by using solar energy has become another active research field for this material.[2] TiO_2 is the most common compound of the 9th most abundant element in the earth's crust and TiO_2 is both a *cheap* material and *non-toxic*.[2] All these characteristics place TiO_2 photocatalytic technologies as very promising alternatives to the currently used fossil fuel-based technologies. The additional attractive options in the environmental cleanup field have made this material worthy of intensive research in different areas of science and technology.

As described below in more detail, TiO_2 is a $3d^0$ semiconductor oxide whose valence band (VB) is mainly O 2*p* in character and whose conduction band (CB) is mostly Ti

3*d* in character.[3] Photocatalytic processes using TiO_2 depends on the photoexcitation of electrons from the VB into the CB so that a redox electron/hole ($e^-_{TiO_2}/h^+_{TiO_2}$) pair is formed. The holes have the ability to act as an oxidising agent and the electrons as reducing agents in redox reactions with species adsorbed on the TiO_2 surfaces. The photocatalytic reactions that can be induced include oxidation of organic pollutant compounds (for cleanup technologies) and water splitting.

There is however a major limitation in the photocatalytic performance of TiO_2 for solar applications. The band-gaps for the two most important phases of TiO_2, namely rutile and anatase, are respectively 3.06 eV and 3.20 eV. This means that TiO_2 only absorbs and utilizes UV light, which leaves it rather inefficient in solar applications because UV radiation represents only 5% of the solar spectrum.[1,2,4-7] Extending absorption of the TiO_2 into the visible region is a prerequisite for the efficient exploitation of solar energy. This can be achieved in principle by modifying the electronic structure of the TiO_2 by means of cationic and anionic doping.[7] Therefore, a detailed understanding of how the dopants can modify the electronic structure of pure TiO_2 is crucial for the development of TiO_2-based photocatalysts active under visible light. In this introductory chapter the basic ideas about the effect that impurities has on the structural and electronic properties of TiO_2 is reviewed along with the latest advances in the field. It is also the intention of this chapter to clarify the motivations and aims of this thesis.

1.2 The structures of the polymorphs of TiO_2.

Crystalline titanium dioxide has three major polymorphs, namely rutile, anatase and brookite. The rutile structure has tetragonal symmetry and belongs to the space group $D_{4h}^{14} - P4_2/mmm$ with cell parameters $a = b = 4.584$ Å, $c = 2.953$ Å ($Vol_{cell} = 62.05$

Å^3) and two TiO_2 molecules per unit cell, i.e. Z = 2. The anatase structure also has tetragonal symmetry and space group $D_{4h}^{19} - I4_1/amd$, with a = b =3.782 Å, c = 9.502 Å (Vol_{cell} = 135.91 Å^3) and Z = 4. Finally the brookite structure has orthorhombic symmetry and belongs to space group $D_{2h}^{15} - Pbca$, with a =5.436 Å b =9.166 Å, c = 5.135 Å (Vol_{cell} = 255.86 Å^3) and Z = 8.[8] There are other less common structures that have been synthesized under special conditions. Of these, cotunnite TiO_2, is one of the hardest polycrystalline materials known and is obtained at high pressure.[9] However, only rutile and anatase polymorphs play any significant role in photocatalytic application of TiO_2,[1] and therefore more detailed consideration of these two structures is given below.

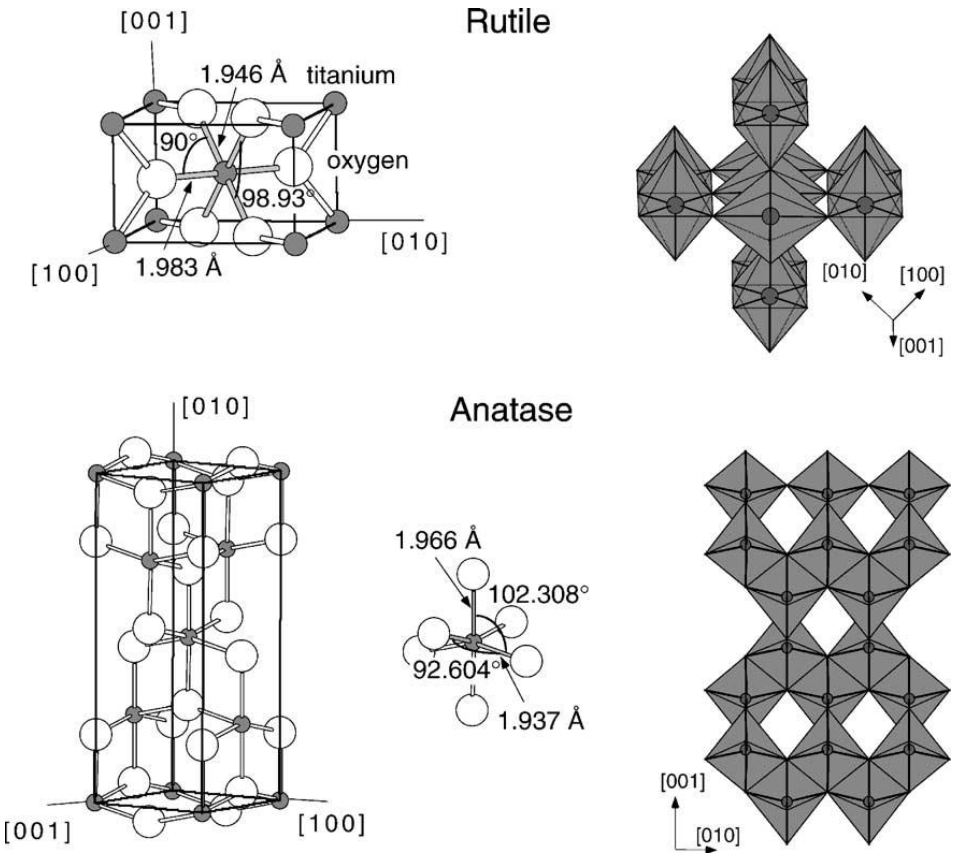


Figure 1.1 Bulk structures of rutile and anatase.[8] Both tetragonal structures are represented in ball-and-stick models, showing the distorted octahedra in each case. The stacking of octahedra in both structures is shown to the right side.

Figure 1.1 shows the unit cell structures of rutile and anatase. Each Ti^{4+} ion is surrounded by six O^{2-} ions in an approximately octahedral arrangement. The two crystal structures differ in the distortion of each octahedron and by the connectivity of the octahedra. The octahedral coordination in rutile is not regular and there is local D_{2h} symmetry with two distinct Ti-O bond lengths. The octahedra in anatase are more distorted than in rutile with bond angles significantly different from 90°, which reduces the local coordination symmetry to D_{2d}. The Ti-O distances in anatase are shorter than in rutile (1.937 Å and 1.966 Å in anatase vs 1.946 Å and 1.983 Å in rutile).[8] It can be also seen in figure 1.1 that in the rutile structure each octahedron is in contact with 10 neighbouring octahedra, with 8 corners shared along the <110> directions and edge sharing along the [001] direction. The direction of the long axis in the edge sharing ribbons alternates by 90° in alternate ribbons. In the anatase structure each octahedron is in contact with 8 neighbours and the octahedra are connected with their edges to the plane of octahedra below; corner-sharing is within the (001) planes. In both structures Ti is sixfold coordinated, but the number of shared octahedral edges increases from two in rutile to four in anatase. These differences in lattice structures cause different mass densities and electronic band structures between the two forms of TiO_2, as will be explained later in this chapter.

1.3 Crystal morphology

The rutile crystals normally found in nature or prepared in the laboratory have a morphology dominated by a prismatic form with 4-fold rotational symmetry, while anatase crystals exhibit a square bipyramidal form, normally truncated with square facets in the (001) and $(00\bar{1})$ planes. Comparison between theoretical calculations based on first principle methods and experimental observations have shown the crystal

shape to be governed by the total energies of the surfaces exposed.[10,11] Ramamoorthy et. al.[12] used self-consistent *ab initio* calculation to estimate the energy of stoichiometric (1 x 1) (110), (100), (001) and (011) surfaces of rutile TiO_2. The results showed that rutile surface energies (γ_R) follow the sequence $\gamma_{R,001} > \gamma_{R,011} > \gamma_{R,100} > \gamma_{R,110}$.

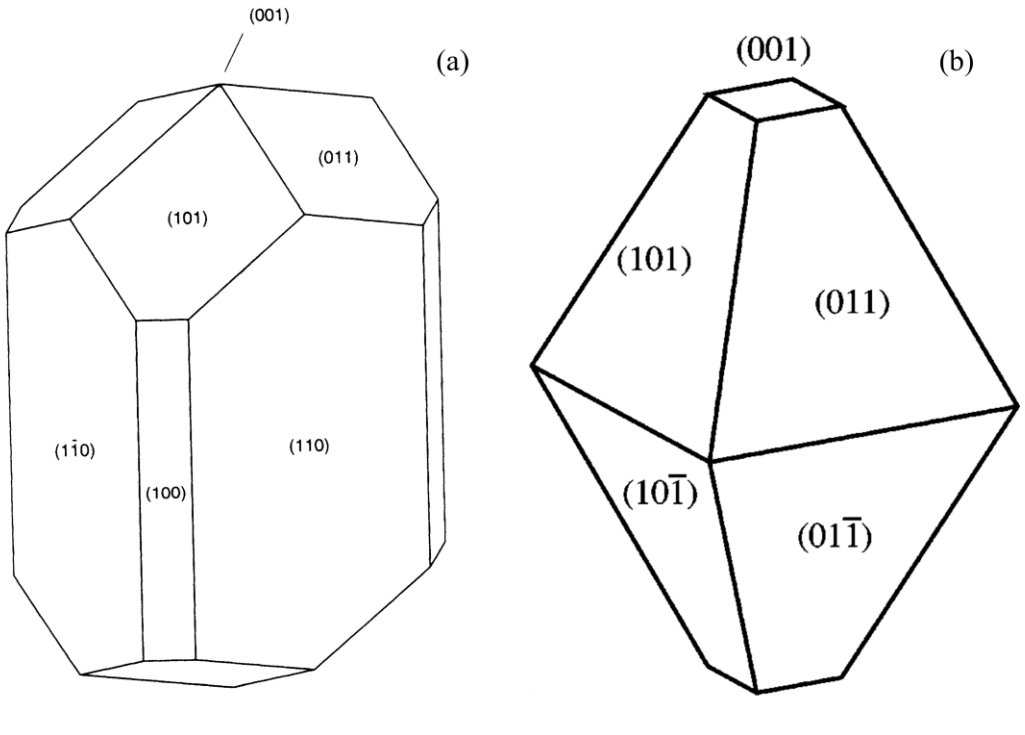


Figure 1.2 The equilibrium shape of macroscopic (a) rutile TiO_2 crystals[12] and (b) anatase TiO_2 crystals[13] using the Wulff construction.

From the calculated energies a three-dimensional Wulff plot was constructed, as shown in figure 1.2.a. The *Wulff construction* shown here is a method for determining the equilibrium shape of crystals based on arguments that minimize the total surface energy so that the area of a given surface type is inversely related to the surface energy.[14] Similarly, Lazzeri et. al.[13] found surface energy values for anatase crystal surfaces (γ_A) to follow the order $\gamma_{A,110} > \gamma_{A,001} > \gamma_{A,100} > \gamma_{A,101}$, which results in the Wulff construction shown in figure 1.2.b. These two shapes are in good agreement with the

shapes of macroscopic crystals found for the TiO_2 polymorphs rutile and anatase. It is well know however that different synthesis conditions brings about difference in the crystal shape and size, but again it has been demonstrated that these changes respond to changes in the relative stability of the crystal surfaces under varying conditions.[10]

1.4 The anatase to rutile phase transformation

On a macroscopic level, rutile is thermodynamically more stable than to anatase with an enthalpy difference of about 0.67 kJ/mole between the two phases. Anatase is metastable at room temperature and converts exothermically and irreversibly to rutile at elevated temperature,[15-19] with a typical activation energy of around 22 kJ/mol. The rate of transformation of high purity commercial anatase powder is immeasurably slow at 600°C but rapid above 730°C.[15,17] However the kinetics of the phase transition are strongly influenced by the presence of impurities and the surface area and particle size of the sample[16,20,21].

On the other hand, anatase has often been found to be a majority product in synthesis of TiO_2 nanoparticles prepared by precipitation from solutions as well as in many mineral samples. Several authors have shown that the synthesis of nanocrystalline TiO_2 generally resulted in the anatase polymorph, which transformed to rutile upon sintering.[22-24] More recent experimental and theoretical work has demonstrated that the anatase-to-rutile phase transition is size-dependent.[10,22] In a kinetic study of anatase to rutile conversion, A. A. Gribb and J. F. Banfield found a negligible conversion in a 800-hour test run for anatase particles under 10nm in size at temperatures up to 525°C while for larger particle conversion reaches up to 60%.[22] This suggests thermodynamic stabilization of the anatase phase relative to the rutile phase on a nanoscopic scale, but

the order of thermodynamic stability is reversed when particle size reaches a specific value. This particle size-dependence in the relative stability of anatase and rutile was explained by A. S. Barnard and L. A. Curtiss in a theoretical study, where they also predicted the particle size at which rutile starts to be the most stable phase at different pH conditions. The transition size varies from 22.7 nm in acidic conditions to 6.9 nm in alkaline conditions. However, the precise transition size depends on other parameters such as temperature, reaction atmosphere, and synthesis conditions as well.[10]

1.5 Phase stability in doped TiO_2

Pronounced changes in the anatase-to-rutile transition are brought about by introducing impurities in the lattice of TiO_2, i.e. by doping TiO_2 with different species.[20,25-27] Whether the presence of the foreign ion on a Ti^{4+}, O^{2-} or interstitial sites in TiO_2 enhances or inhibits the transformation from anatase to rutile will depend on the ability of the two phases to compensate the stress brought about by a differently sized ion and/or to compensate the charge when the ion charge is different from +IV (cations) or –II (anions). Anatase has a less dense unit cell and can accommodate a large number of impurities; however, traditional crystal chemical theory argues that shared edges should lead to cation–cation repulsion and structural destabilization, which makes this polymorph less stable toward bigger cation dopants. A good example of this can be seen in sol-gel $Sn_xTi_{1-x}O_2$ solid solutions discussed in chapter 7, where the presence of a bigger Sn^{4+} cation accelerates the anatase to rutile conversion. When it comes to charge compensation the ability of the structure to tolerate the formation of vacancies plays a major role, as it is explained later in this chapter. The presence of a cation vacancy should be better tolerated in the anatase structure, due to a better charge defect compensation by neighbouring Ti cations. J. Arbiol et.al. found a large anatase phase

stabilization in sol-gel TiO_2 samples doped with Nb^{5+}, whose incorporation depends mainly on charge compensation by cation vacancies since it has a similar cation radius to Ti^{4+} ($r_{Nb^{5+}} = 0.70$ Å and $r_{Ti^{4+}} = 0.68$ Å).[20] R. Arroyo et.al. found Mn^{2+} doping to inhibit the anatase to rutile conversion, which starts to occur together with Mn^{2+} oxidation to Mn^{4+} at temperatures over 600°C. It was concluded that the anatase phase is stable in the presence of Mn^{2+} but not in presence of Mn^{4+}, where charge compensation is no longer needed.[25] In the case of anionic doping, changes in the relative stability of anatase and rutile is normally not governed by differences in charge compensation as the tolerance to the formation of oxygen vacancies is fairly similar in the two polymorphs. The formation energy of an O vacancy is 4.2 eV for anatase and 4.3 eV for rutile according to theoretical calculations.[28] As an example, N-doped TiO_2, a system where a species NO^{3-} sits on O^{2-} sites (as discussed in chapter 3), has been successfully synthesized via sol-gel routes in both anatase and rutile polymorphs.[29]

For thin film materials, the substrate strongly influences the crystallization temperature and favoured phase of TiO_2. Although, as discussed above, macroscopic TiO_2 is only thermodynamically stable in the rutile phase, epitaxial films of anatase TiO_2 have been grown on $SrTiO_3$ (001) substrates with thickness up to 1μm. The films are stable at temperatures up to 1000°C. The large anatase phase stabilization is due to a lower lattice mismatch between anatase and $SrTiO_3$ structures in the (001) plane (-3.1%) compared to that between rutile and $SrTiO_3$ (9%).[30] This large epitaxial stabilization can be used to study the properties of systems in the anatase phase which are otherwise unstable.

1.6 The electronic structure of TiO_2

The classical band theory approach to electronic structure, which explore how the states of a free electron are perturbed by the periodic potential of a crystal lattice, is not a useful starting point for transition metal oxides such as TiO_2, because *d* states cannot be easily represented using a free electron basis.[31] A simpler and more appealing chemical perspective is based on a linear combination of atomic orbital (LCAO), an approach similar to that used in molecular orbital (MO) theory. This is referred to as tight binding method. An approximation to periodic tight binding theory that helps to visualize how the electronic structure of a metal oxide arises, is the cluster model. This model considers the overlap of orbitals within a limited number of atoms to generate molecular orbitals Ψ in the form:

$$\Psi = \sum_i c_i \varphi_i$$

where the φ are the wave function of an individual atomic orbital (AO) and the c are LCAO coefficients.

In the case of TiO_2, the near octahedral coordination around Ti^{4+} cation discussed allows one to define a local cluster unit TiO_6^{8-} that repeats throughout the crystal. A qualitative molecular orbital diagram of this octahedral unit is shown in figure 1.3. This qualitative molecular orbital scheme is constructed by firstly deriving the different possible symmetry-adapted linear combination of oxygen orbitals followed by mixing with metal orbitals of appropriate symmetry. Mixing between these O 2*p* and Ti 3*d* orbitals produces bonding MOs, localized more on oxygen, and antibonding MOs more on titanium. For example,

$$\Psi_{\text{bonding}} = \alpha\varphi_{Ti\ 3d:e_g} + \beta\varphi_{O\ 2p:e_g}$$

and

$$\Psi_{\text{antibonding}} = \gamma\varphi_{Ti\ 3d:e_g} - \delta\varphi_{O\ 2p:e_g}$$

where α, β, γ and δ are positive coefficients. Of particular interest are the e_g and t_{2g} combinations of O 2*p* orbitals that can combine with the appropriate Ti 3*d* orbitals. The ligand field causes a splitting of the Ti 3*d* orbital into two bands. The e_g orbitals point directly toward the oxygen ligands forming σ-type antibonding orbitals, while t_{2g} orbitals point between neighbouring oxygen atoms and form less antibonding π-type orbitals.

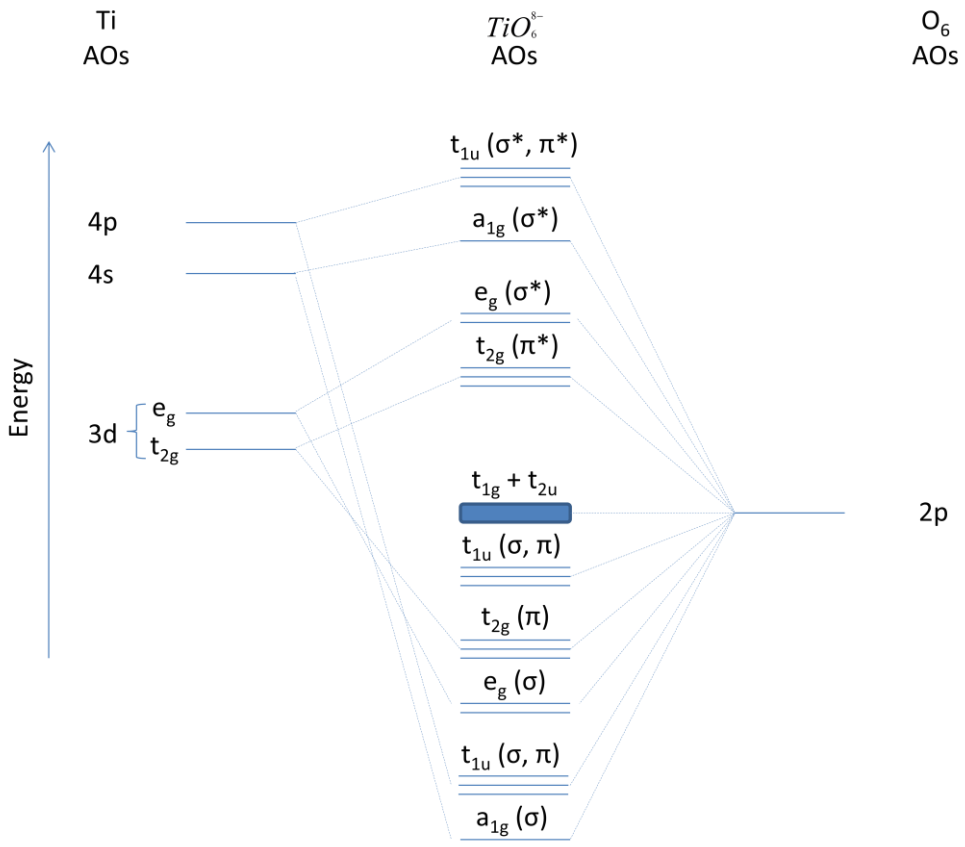


Figure 1.3 Qualitative molecular orbital diagram for Ti^{4+} in an octahedron of six O^{2-}. Symmetry labels used correspond to irreducible representations of the O_h point group.[31]

Although figure 1.3. shows a large number bonding and non-bonding MOs derived from O 2p levels, the total number of these is just the number of original AOs. The electron count appropriate to a d^0 metal oxide such as TiO_2 is therefore just enough to fill the bonding and non-bonding MOs derived mainly from O 2*p* orbitals. In an extended solid these MOs will merge to generate a virtually continuous filled *valence* band with dominant O 2*p* character, while antibonding MOs form an empty *conduction* band mainly Ti 3*d* in character. In-between these two bands there is a region of forbidden electronic states that constitutes the *band gap* of the material. Detailed studies on the electronic structure of TiO_2 have been carried out by theoretical and experimental means.[8,32,33] As expected from the discussion above, the common description of TiO_2 electronic structure given in all these studies is that the filled valence band is derived largely from O 2*p* levels and the conduction band from Ti 3*d* orbitals, although considerable mixing of these atomic levels takes place. Figure 1.4 shows the calculated total density of electronic states (1.4a) and the contribution of O 2*s*, O 2*p* and Ti 3*d* orbitals (1.4b, 1.4c and 1.4d respectively) for both anatase and rutile polymorphs plotted on a relative energy scale where the valence band maximum is taken as 0 eV.[33] At high binding energy, electronic states derived from O 2*s* orbitals can be seen. These have only weak hybridisation with O 2*p* and Ti 3*d* states and essentially no states derived from O 2*s* orbitals are observed in the valence or conduction bands as seen in figure 1.4b for both structures. At higher energy, the valence band presents a double-peak structure originating from the separation of bonding and nonbonding O 2*p* states. As shown in figure 1.4c, although O 2p states contribute most strongly to the valence band, they also provide a small contribution to the conduction band. The lowest conduction band consists of two sets of Ti 3*d* bands, which have their atomic origin from the hybridised states of t_{2g} and e_g local symmetry

Figure 1.4d shows Ti 3*d* hybridisation with O 2*p* mainly around the lowest band that is the bonding O 2*p*.

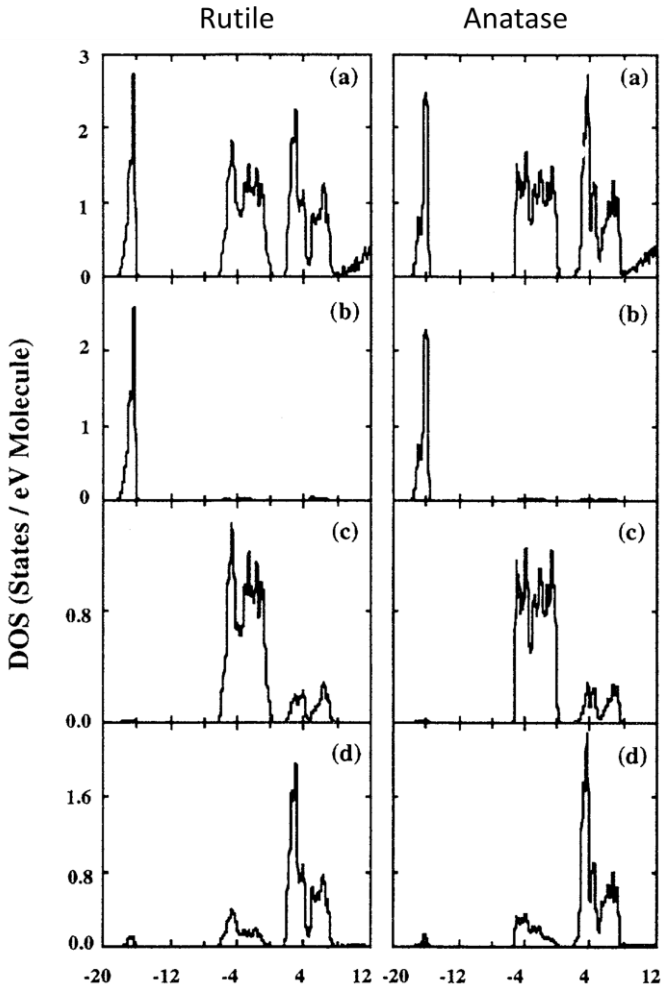


Figure 1.4 Calculated total and partial DOS of rutile (left panel) and anatase (right panel): (a) total, (b) O 2s, (c) O 2p, and (d) Ti 3d.[33]

This theory has been found in reasonable agreement with experimental measurements.[31,34,35] In the *O* K_α X-ray *absorption* spectrum of TiO_2, where final state should be of O 2*p* character, there is substantial intensity at energies corresponding to excitation into the the conduction band, which reflects the contribution of oxygen to the conduction band.[34] On the other hand, the *Ti* K_α *emission* spectrum shows peaks deriving from the valence band and the lower energy oxygen 2*s* band, which suggests that some orbital mixing occurs, giving a Ti contribution to the predominantly oxygen-

derived valence band.[35] In addition, the Ti L_{23} absorption spectrum involving transitions from Ti 2*p* states clearly shows the crystal-field splitting of the Ti 3*d*-like states into e_g and t_{2g} components.[8]

The UV-visible absorption spectrum of TiO_2 is related to inter band transitions. Measurements indicate that the characteristic absorption of TiO_2 in the near UV regon of the electromagnetic spectrum corresponds to a band-gap transition.[31] The near coincidence of the edge of the optical absorption with that of the photoconductivity spectrum shows that the UV-visible absorption produces free carriers, and corresponds to a true band-gap transition without formation of a strongly bound exciton.[36] The nature of this band-gap transition and its magnitude depends on the crystalline structure of TiO_2. Figure 1.5 shows the calculated band structures along the symmetry lines of the Brillouin zone for rutile and anatase As seen in figure 1.5.a, the rutile polymorph has a direct band-gap,[33] i.e. the conduction band minimum (CBM) and the valence band maximum (VBM) are both at centre of the centre of the Brillouin zone (Γ) so that the transition occurs whilst conserving the wave vector ($\boldsymbol{k}$) and therefore satisfying the selection rule for electronic states in band-to-band transitions:[3]

$$\Delta \boldsymbol{k} = 0$$

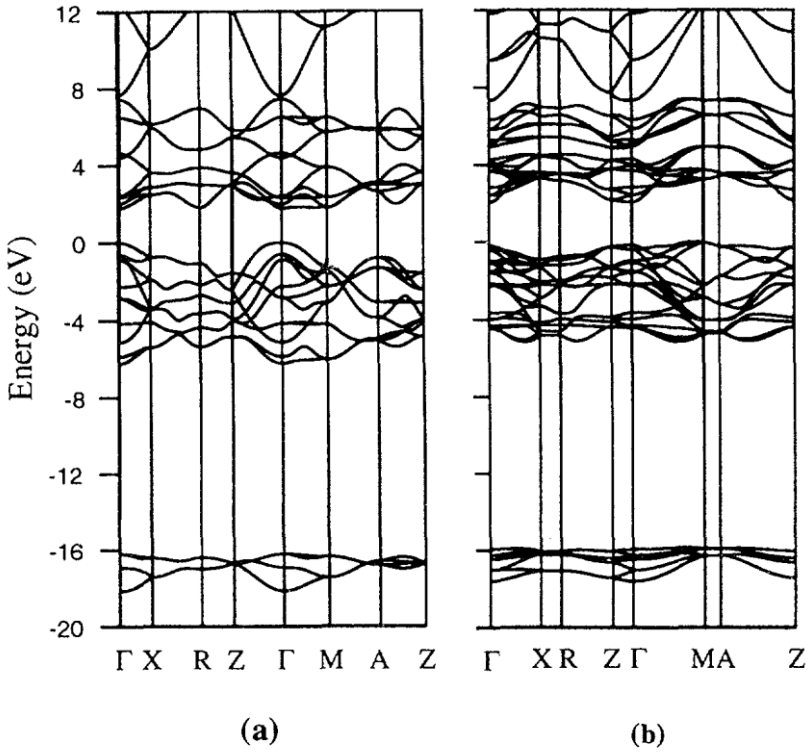


Figure1.5 Calculated band structures of (a) rutile and (b) anatase. The fractional coordinates of the high-symmetry points of de Brillouin zone used are: Γ=0,0,0; Z=0,0,1/2; A=1/2,1/2,1/2; M=1/2,1/2,0; X=0,1/2,0; R=0,1/2,1/2.[33]

As in the case of symmetry-based selection rules for localized transitions, the selection rule for band-to-band transitions can be broken by the intervention of appropriate vibrational modes, which is required when the CBM and VBM are not at the same wavevector. Figure 1.5.b show that this is the case for the anatase polymorph of the TiO_2 since the CBM is at Γ and the VBM is at the M point so that indirect band-gap transitions are expected to occur in anatase TiO_2. However, the energy levels of the VB at Γ is less than 0.2 eV lower than the VBM, which has made some authors consider the band-gap transition in anatase TiO_2 to be approximately direct.[32,33] Experimentally determined values of the magnitude of the band-gap at room temperature for these two structure of TiO_2 are typically 3.06 eV for rutile and 3.20 eV for anatase TiO_2.

Pure and stoichiometric TiO_2 is an insulating oxide because the large band-gap means there is no significant thermal inter-band excitation and the concentration of free charge carriers is negligible at room temperature. However, as for many transition metal oxides the conduction in TiO_2 is dominated by impurities and/or defects arising from non-stoichiometry. The formation of oxygen vacancies at room temperature is accompanied by the partial reduction of Ti^{4+} to Ti^{3+}, whose 3*d* electronic states lie just below the conduction band minimum. They are close enough in energy for electrons to be thermally excited into the conduction band. This generates negatively charged carriers and gives rise to the well-known n-type conductivity of TiO_2.

The conductivity σ in a n-type semiconductor is given by:

$$\sigma = ne\mu_e$$

where n is the electron concentration, e the electron charge and μ_e is the electron mobility. While n depends on the concentration and nature of the impurities or defects present in the semiconductor, μ_e is an intrinsic property of the material and its structure. The two common TiO_2 polymorphs have significant differences in electron mobility, with quoted values of ~1cm^2/Vs for rutile and ~10cm^2/Vs for the anatase.[8] This has important implications the use of TiO_2 such as a photocatalysts, as discussed later in this chapter.

1.7 Tuning the band gap of TiO_2 for visible light photocatalysis

When TiO_2 is irradiated with photons whose energies are larger than the band gap, electrons in the VB are excited to higher energy levels in the CB so that a redox electron/hole ($e^-_{TiO_2}/h^+_{TiO_2}$) pair is formed. The holes have the ability to act as an

oxidising agent and the electrons as reducing agents. Thus the photo excited $e^-_{TiO_2}/h^+_{TiO_2}$ pair can subsequently participate in redox reactions with surface adsorbed species. This leads to a net conversion of the incident energy of the photons into chemical energy. The main characteristic of a photocatalyst is that it mediates processes of this sort. Redox processes involving electrons or holes depend upon the respective positions of the band edges for the conduction and valence bands relative to the standard reduction potential levels of target substrate species.

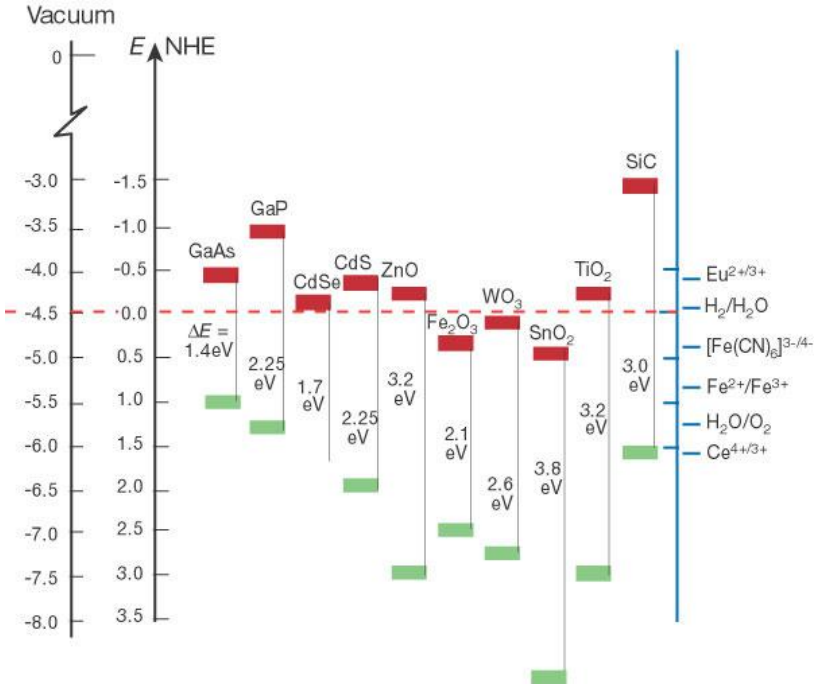


Figure 1.6 Band positions of several semiconductors relatve to some redox potentials.[37]

Figure 1.6 shows the band edge energy positions of several semiconductors in an aqueous solution at pH = 1 relative to the standard reduction potentials of some common redox couples. It can be seen that on the scale where the normal hydrogen electrode reduction potential is set at zero (second scale from the left), the holes generated in the TiO_2 VB have a reduction potential in excess of +3V. This makes them strong oxidizing agents, which is the key element in pollutant degradation. It can also

be seen that the electrons promoted into the CB can reduce protons to hydrogen as the position of the CB lies just above H_2/H^+ couple so that an electron in the CB has a more negative reduction potential than the H_2/H^+ couple. The holes in the valence band can also oxidize H_2O to O_2 (the standard reduction potential for O_2 is +1.23V at pH = 0) to complete the water splitting reaction.

Photocatalysis with TiO_2 itself depends on interband excitations that only occur when the photon energy exceeds 3.0 eV (rutile) or 3.2 eV (anatase). This corresponds to wavelengths under 400 nm, which defines the onset of the ultraviolet (UV) region of the electromagnetic spectrum. Figure 1.7 shows the power spectrum of solar radiation reaching the earth's surface. It can be seen that only a small fraction of the total spectrum falls in the UV and is therefore harvestable in TiO_2 mediated photocatalytic processes. This limits the potential usefulness of TiO_2 for solar applications.

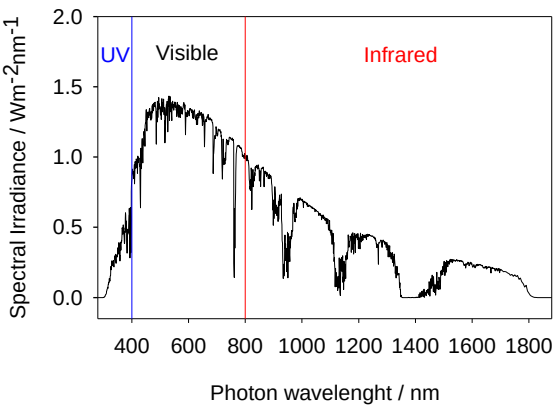


Figure 1.7 Spectal irradiance of sun light at the earth's surface as a function of wavelength.

The limitations of TiO_2 in solar energy technologies due to its large band-gap means that materials modification is required in order to shift the energy of the interband transitions into the visible region. This region encompasses more than 50% of the solar spectrum. The basic strategy is to introduce impurities or dopants that produce

electronic states within the band-gap of TiO_2. These may be filled states above the VB maximum or empty states below the CB minimum. It is moreover useful to distinguish between cationic and anionic doping. As regards cationic doping, more the 20 metal ions (most of them transition metals) have been studied and very well established theories about their action have been developed.[7] Doping with metal ions could expand the photo-response of TiO_2 into the visible spectrum. As metal ions are incorporated into the TiO_2 lattice, impurity energy levels in the band gap of TiO_2 are formed, as indicated below:

$$M^{n+} + h\nu \rightarrow M^{(n+1)+} + e^-_{CB}$$

$$M^{n+} + h\nu \rightarrow M^{(n-1)+} + h^+_{VB}$$

where M^{n+}represent the metal ion dopant. However, metal ion dopants can trap electrons or holes and therefore act as recombination centres:

$$M^{n+} + e^-_{CB} \rightarrow M^{(n-1)+}$$

$$M^{n+} + h^+_{VB} \rightarrow M^{(n+1)+}$$

The energy level of $M^{n+}/M^{(n-1)+}$ should be less negative (i.e. lower relative to the vacuum level) than that of the CB edge of TiO_2, while the energy level of $M^{n+}/M^{(n+1)+}$ should be less positive (i.e. higher relative to the vacuum level) than that of the VB edge of TiO_2. For photocatalytic reactions, carrier separation and transport are as important as carrier trapping. Photocatalytic reaction can only occur if the trapped electron and hole are transferred to the surface. Therefore, metal ions should be incorporated near the surface of TiO_2. If dopants are only found deep in the bulk, metal ions are likely to behave as recombination centres, since electron/hole transfer to the

interface is more difficult. Furthermore, there is an optimum concentration of metal dopant ions, above which the photocatalytic activity decreases due to the increase of electron-hole recombination rate.

Anionic doping is a novel method that, unlike metal ion doping, does not necessarily introduce recombination centres. Therefore, anionic doping is a more effective way to enhance photocatalytic activity.[7,38] Figure 1.8.b-d illustrate various scenarios of changes that can occur in the valence band of TiO_2 (figure 1.8.a) on anionic doping. The presence of localized states near the valence band edge has been suggested to be the origin of the visible-light activity of anion-doped TiO_2. Excitation from such states to the conduction band, illustrated in figure 1.8.b, would correspond to a shift of the absorption edge to lower energies. However, whether this shift implies "band gap narrowing" or not is widely debated in the literature.[5,38,39] The debate centres around whether states above the valence band edge are localized or delocalized. Anionic dopants can also enhance formation of defects states within the band gap that can contribute to the absorption in the visible as shown in figure 1.8.d.[5,38] True band gap narrowing through broadening of the VB (as illustrated in figure 1.6.c) has been proposed for different anion-doping system like N-doped TiO_2[4] and S-doped TiO_2,[40] has whether this concept is applicable for low doping concentration has been called into question.[38,39] A true narrowing of the original band gap of TiO_2 would require a heavy

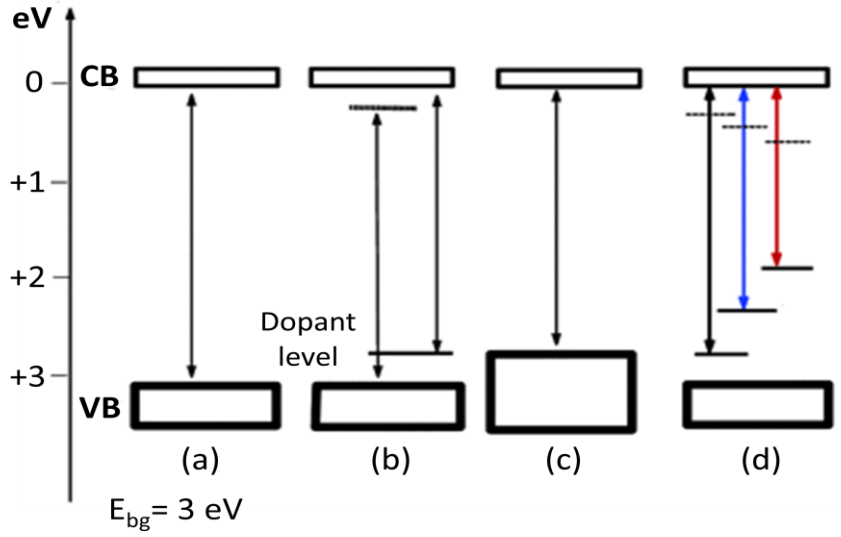


Figure 1.8 Illustration of possible changes that might occur to the band gap structure of TiO_2 on doping with various materials: (a) band gap of pure TiO_2; (b) doped TiO_2 with localized dopant levels near the VBM and the CBM; (c) band gap narrowing resulting from VB broadening; and (d) localized dopant levels and defect levels with transitions to the CB.[38]

anionic or cationic doping so that TiO_2 and dopant states merge. In this case, however, it could be questionable whether TiO_2 retains its original integrity.

Asahi et al.[4] studied the effects of substitutional replacement of O by C, N, F, P and S in anatase TiO_2. They found nitrogen to be the most successful dopant, and suggested that a mixing of N 2*p* states and O 2*p* states shifted the VB edge upwards to narrow the band gap of TiO_2 and did not create localized states within the band-gap. However, after the publication of Asahi several papers have suggested other means by which the N doping could shift the response of TiO_2 into the visible range. These include the formation of localized states within the TiO_2 band-gap. Moreover, the actual N species responsible for photoabsorption shifts was not completely understood.[2,5,6] .

1.8 Scope of the current thesis.

Following this introductory chapter, chapter 2 gives a background to the experimental techniques used in the current work. Chapter 3 describes details of the apparatus and instrumentation used but details of synthesis and preparation procedures are presented in the subsequent chapters. X-ray photoelectron spectroscopy (XPS) is the most widely used technique in the study of the N species that are present in N-doped TiO_2 and their effect on the electronic structure of TiO_2. However many ambiguities remain. Chapter 4 describes a study of N doping in TiO_2 by XPS with much better signal to noise and energy resolution than in previous work using the ESCA 300 spectrometer at the National Centre for Electron Spectroscopy and Surface Analysis (NCESS) at Daresbury Laboratory. Moreover, the Inorganic Chemistry Laboratory houses the Centre for Advanced Electron Spin Resonance (CAESR) which facilitated the study of paramagnetic nitrogen species that have been reported to have an effect on the catalytic performance of N-doped TiO_2. [6,41] The results from these two techniques are combined with determination of bulk nitrogen levels using a novel inert gas fusion technique. It is shown that catalytic activity is associated with the presence of nitrogen bound to lattice oxygen to give $(NO)'_O$ which can be photoexcited to give $(NO)^{x}_O$.

When TiO_2 is doped with transition metals, control of the oxidation state of the dopant ions to maintain charge balance in the crystal structure is important for the photocatalytic properties.[42] For example, when Rh^{3+}, Cr^{3+} and Ni^{2+} ions are partly substituted for Ti^{4+} sites in the crystal lattice of TiO_2 and $SrTiO_3$ hosts, charge compensation by codoping with high-valent ions such as Sb^{5+}, Ta^{5+}, and Nb^{5+} improves the photocatalytic activities under visible light irradiation.[42-45] It has been reported that platinum-loaded $SrTiO_3$ doped with Rh is a highly active visible-light-driven

photocatalyst for H_2 production in the presence of methanol as an electron donor.[46] The visible-light response of rhodium-doped $SrTiO_3$ is due to the electron transition from the electron donor levels formed by doped Rh^{3+} ions to the conduction band of $SrTiO_3$. Based on EPR studies, R. Niishiro et.al. suggest that a higher photocatalytic activity of Rh/Sb-codoped TiO_2 compared with Rh-doped TiO_2 is caused by suppression of the formation of paramagnetic Rh^{4+} due to charge compensation from Sb^{5+}.[42] Chapter 5 describes an experimental study of the electronic structure of Rh-doped TiO_2 and Rh/Sb-codoped TiO_2.

Another issue that strongly impacts the photocatalytic activity of TiO_2 is the $e^-_{TiO_2}/h^+_{TiO_2}$ pair recombination time. Anatase TiO_2 is generally found to be a better catalyst than rutile TiO_2 as a consequence of the fact that the bandgap of anatase is indirect whereas rutile has a direct but forbidden bandgap, which coupled with higher electron mobility in anatase enables more efficient separation of electron hole pairs. Attempts to suppress quick $e^-_{TiO_2}/h^+_{TiO_2}$ pair recombination by deposition of metals such as Pt, Au, Pd, Rh, Ni, Cu and Ag onto the TiO_2 surface have been widely studied.[1,7] The electron promoted into the CB from the VB in the TiO_2 is transferred into the metal CB so that it is separated from the hole, which remains in the semiconductor. This dramatically reduces the possibility of electron-hole recombination and leads to higher photocatalytic activity. Another alternative for increasing the charge separation is the use of semiconductors heterojunctions in composite systems.[1,7] In this type of system a second semiconductor is coupled to the TiO_2, and charge separation is achieved in a similar way to that found with metal loading. After formation of the $e^-_{TiO_2}/h^+_{TiO_2}$ pair, either electron or hole can be transferred into the coupled semiconductor's CB or VB respectively. Guided by this idea our group has been studying the coupling of tin oxide

(SnO_2) with TiO_2 by growing thin films of SnO_2 on TiO_2 single crystals by molecular beam epitaxy (MBE). It was recently found that, using different deposition conditions, either heterostructures or solid solutions of the two oxides could be produced.[47] Both types of samples have shown an improved photocatalytic activity compared with pure TiO_2. The heterostructure semiconductors have improved performance under UV irradiation, while solid solutions present a better catalytic behaviour under visible irradiation. Although enhanced photocatalytic activity upon doping TiO_2 powders with tin has been reported in the literature,[48,49] the basis of this behaviour remains unclear. Chapter 6 describes a detailed study of the properties of Sn-doped TiO_2 ceramics prepared by high temperature solid state synthetic procedures. It is shown that Sn doping in $Sn_xTi_{1-x}O_2$ leads to a narrowing of the bulk bandgap at low doping levels along with the introduction of Sn-related surface states that sit above the main valence band maximum. This work is extended in chapter 7 to a study of high area $Sn_xTi_{1-x}O_2$ prepared by a sol-gel route. It is shown that Sn doping promotes the anatase to rutile phase transformation at very much lower temperatures than found in undoped TiO_2. At the same time Sn doping inhibits particle sintering, allowing preparation of high area Sn-doped TiO_2 rutile photocatalysts. The Sn-doped rutile photocatalysts are shown to display superior photocatalytic activity to N-doped anatase. The final experimental chapter 8 presents a study of epitaxial growth of Sn-doped anatase on $SrTiO_3$. As mentioned above it is not possible to study this phase in bulk material but epitaxial stabilisation renders Sn-doped anatase stable over a wide temperature range. In contrast to Sn-doped rutile, Sn doping in the anatase phase leads to a monotonic increase in the bandgap as gauged by the position of the band edge in X-ray photoelectron spectroscopy. The thesis finishes with a brief final chapter 9, which compares results from the systems studies and lays down suggestions for future work.

1.9 References

(1) Linsebigler, A. L.; Lu, G. Q.; Yates, J. T. *Chemical Reviews* **1995**, *95*, 735.

(2) Qiu, X. F.; Burda, C. *Chemical Physics* **2007**, *339*, 1.

(3) Cox, P. A. *Electronic Structure and Chemistry of Solids*; Oxford University Press: Oxford, 1987.

(4) Asahi, R.; Morikawa, T.; Ohwaki, T.; Aoki, K.; Taga, Y. *Science* **2001**, *293*, 269.

(5) Batzill, M.; Morales, E. H.; Diebold, U. *Physical Review Letters* **2006**, *96*.

(6) Livraghi, S.; Paganini, M. C.; Giamello, E.; Selloni, A.; Di Valentin, C.; Pacchioni, G. *Journal of the American Chemical Society* **2006**, *128*, 15666.

(7) Ni, M.; Leung, M. K. H.; Leung, D. Y. C.; Sumathy, K. *Renewable & Sustainable Energy Reviews* **2007**, *11*, 401.

(8) Diebold, U. *Surface Science Reports* **2003**, *48*, 53.

(9) Dubrovinsky, L. S.; Dubrovinskaia, N. A.; Swamy, V.; Muscat, J.; Harrison, N. M.; Ahuja, R.; Holm, B.; Johansson, B. *Nature* **2001**, *410*, 653.

(10) Barnard, A. S.; Curtiss, L. A. *Nano Letters* **2005**, *5*, 1261.

(11) Yang, H. G.; Sun, C. H.; Qiao, S. Z.; Zou, J.; Liu, G.; Smith, S. C.; Cheng, H. M.; Lu, G. Q. *Nature* **2008**, *453*, 638.

(12) Ramamoorthy, M.; Vanderbilt, D.; Kingsmith, R. D. *Physical Review B* **1994**, *49*, 16721.

(13) Lazzeri, M.; Vittadini, A.; Selloni, A. *Physical Review B* **2001**, *63*, 9.

(14) Zangwill, A. *Physics at Surfaces*: Cambridge, 1988.

(15) Czanderna, A. W.; Rao, C. N. R.; Honig, J. M. *Transactions of the Faraday Society* **1958**, *54*, 1069.

(16) Yoganarasimhan, S. R.; Rao, C. N. R. *Transactions of the Faraday Society* **1962**, *58*, 1579.

(17) Czanderna, A. W.; Clifford, A. F.; Honig, J. M. *Journal of the American Chemical Society* **1957**, *79*, 5407.

(18) Iida, Y.; Ozaki, S. *Journal of the American Ceramic Society* **1961**, *44*, 120.

(19) Shannon, R. D.; Pask, J. A. *Journal of the American Ceramic Society* **1965**, *48*, 391.

(20) Arbiol, J.; Cerda, J.; Dezanneau, G.; Cirera, A.; Peiro, F.; Cornet, A.; Morante, J. R. *Journal of Applied Physics* **2002**, *92*, 853.

(21) Byun, C.; Jang, J. W.; Kim, I. T.; Hong, K. S.; Lee, B. W. *Materials Research Bulletin* **1997**, *32*, 431.

(22) Gribb, A. A.; Banfield, J. F. *American Mineralogist* **1997**, *82*, 717.

(23) Zhang, H. Z.; Banfield, J. F. *Journal of Materials Chemistry* **1998**, *8*, 2073.

(24) Zhang, H. Z.; Finnegan, M.; Banfield, J. F. *Nano Letters* **2001**, *1*, 81.

(25) Arroyo, R.; Cordoba, G.; Padilla, J.; Lara, V. H. *Materials Letters* **2002**, *54*, 397.

(26) Francisco, M. S. P.; Mastelaro, V. R. *Chemistry of Materials* **2002**, *14*, 2514.

(27) Fresno, F.; Tudela, D.; Coronado, J. M.; Fernandez-Garcia, M.; Hungria, A. B.; Soria, J. *Physical Chemistry Chemical Physics* **2006**, *8*, 2421.

(28) Di Valentin, C.; Pacchioni, G.; Selloni, A.; Livraghi, S.; Giamello, E. *Journal of Physical Chemistry B* **2005**, *109*, 11414.

(29) Livraghi, S.; Czoska, A. M.; Paganini, M. C.; Giamello, E. *Journal of Solid State Chemistry* **2009**, *182*, 160.

(30) Gorbenko, O. Y.; Samoilenkov, S. V.; Graboy, I. E.; Kaul, A. R. *Chemistry of Materials* **2002**, *14*, 4026.

(31) Cox, P. A. *Transition Metal Oxides - An Introdution to their Electronic Structure and Properties*; Clarendon Press: Oxford, 1995.

(32) Asahi, R.; Taga, Y.; Mannstadt, W.; Freeman, A. J. *Physical Review B* **2000**, *61*, 7459.

(33) Mo, S. D.; Ching, W. Y. *Physical Review B* **1995**, *51*, 13023.

(34) Grunes, L. A.; Leapman, R. D.; Wilker, C. N.; Hoffmann, R.; Kunz, A. B. *Physical Review B* **1982**, *25*, 7157.

(35) Tsutsumi, K.; Aita, O.; Ichikawa, K. *Physical Review B* **1977**, *15*, 4638.

(36) Cronemeyer, D. C. *Physical Review* **1952**, *87*, 876.

(37) Gratzel, M. *Nature* **2001**, *414*, 338.

(38) Serpone, N. *The Journal of Physical Chemistry B* **2006**, *110*, 24287.

(39) Di Valentin, C.; Finazzi, E.; Pacchioni, G.; Selloni, A.; Livraghi, S.; Paganini, M. C.; Giamello, E. *Chemical Physics* **2007**, *339*, 44.

(40) Umebayashi, T.; Yamaki, T.; Itoh, H.; Asai, K. *Applied Physics Letters* **2002**, *81*, 454.

(41) Livraghi, S.; Votta, A.; Paganini, M. C.; Giamello, E. *Chemical Communications* **2005**, 498.

(42) Niishiro, R.; Konta, R.; Kato, H.; Chun, W. J.; Asakura, K.; Kudo, A. *Journal of Physical Chemistry C* **2007**, *111*, 17420.

(43) Ishii, T.; Kato, H.; Kudo, A. *Journal of Photochemistry and Photobiology a-Chemistry* **2004**, *163*, 181.

(44) Kato, H.; Kudo, A. *Journal of Physical Chemistry B* **2002**, *106*, 5029.

(45) Niishiro, R.; Kato, H.; Kudo, A. *Physical Chemistry Chemical Physics* **2005**, *7*, 2241.

(46) Konta, R.; Ishii, T.; Kato, H.; Kudo, A. *Journal of Physical Chemistry B* **2004**, *108*, 8992.

(47) Palgrave, R. G.; Bourlange, A.; Payne, D. J.; Foord, J. S.; Egdell, R. G. *Crystal Growth & Design* **2009**, *9*, 1793.

(48) Kutty, T. R. N.; Avudaithai, M. *Chemical Physics Letters* **1989**, *163*, 93.

(49) Sayilkan, F.; Asiltuerk, M.; Tatar, P.; Kiraz, N.; Sener, S.; Arpac, E.; Sayilkan, H. *Materials Research Bulletin* **2008**, *43*, 127.

Chapter 2 Background to Experimental Techniques

2.1. X-ray Photoelectron Spectroscopy (XPS)

X-ray photoelectron spectroscopy (XPS) is a technique based on the photoelectric effect, as enunciated by Einstein in 1905. Early experimental observations showed that there is a threshold in frequency below which light, regardless of intensity, fails to eject electrons from a metallic surface. This is a natural consequence of the postulate that light consists of photons of energy *E*

$$E = h\nu$$

where h is the Planck's constant and ν is the frecquency.[1] The energy associated with the threshold frequency ν_c is a measure of the strength of the potential barrier at the surface of the metal that prevents conduction electrons from escaping into empty space. This is called the work function ϕ,[2] so that

$$\phi = h\nu_c.$$

Typical values of work function are in the range 2 to 6 eV.

At frequencies above ν_c, the excess energy of the photon above ϕ provides photoelectrons with a kinetic energy, whose maximum value is

$$E_{kin}^{max} = h\nu - \phi.$$

The maximum kinetic energy is associated with electrons emitted from the Fermi level E_F, i.e. from the highest lying occupied electronic states of the metal. Electrons whose energy levels lie below the E_F emerge with correspondingly less kinetic energy

$$E_{kin} = h\nu - \phi - E_B$$

where E_B is the electron binding energy.

With photon energies in the ultraviolet region of the electromagnetic spectrum only loosely bound valence band electrons can be ionized, but under irradiation with soft X-rays both core and valence levels are accessible. Laboratory based x-ray photoelectron spectroscopy (XPS) experiments are commonly carried out using Al Kα or Mg Kα lines, with photon energies of 1486.6 eV and 1253.6 eV respectively. Core level binding energies are essentially characteristic of an element so that core XPS provides a means of chemical analysis.

Figure 2.1 shows an energy level diagram for a photoemission experiment from a metal surface. The contact potential between the sample and the spectrometer modifies the alignment of the Fermi level relative to the vacuum level. However, knowledge of the value of the work function is not essential in standard photoelectron spectroscopy measurements because, conventionally, the electron binding energy is measured with respect to the Fermi level of the metal that the sample holder is made of, which is also aligned with the Fermi level of the metal forming the spectrometer. For samples with reasonable conductivity, the Fermi level of the sample lines up upon contact with that of the holder.

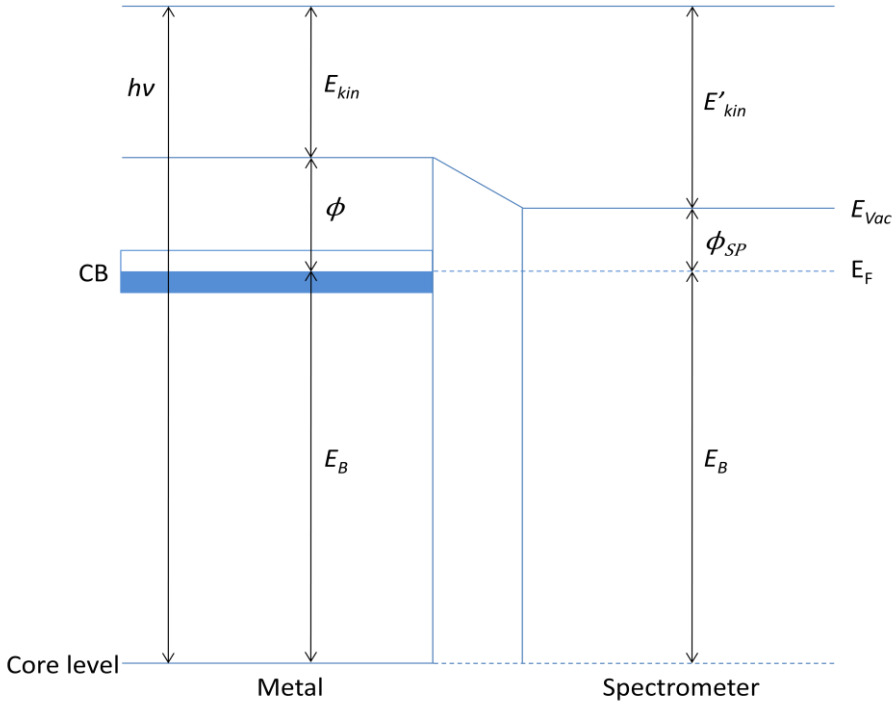


Figure 2.1. Energy level diagram for photoemission from a metal. The contact potential between sample and spectrometer, $e(\varphi - \varphi_{SP})$, changes the kinetic energy of the electrons as it enters in the spectrometer. Therefore only spectrometer work function is needed to calculate E_B.[1]

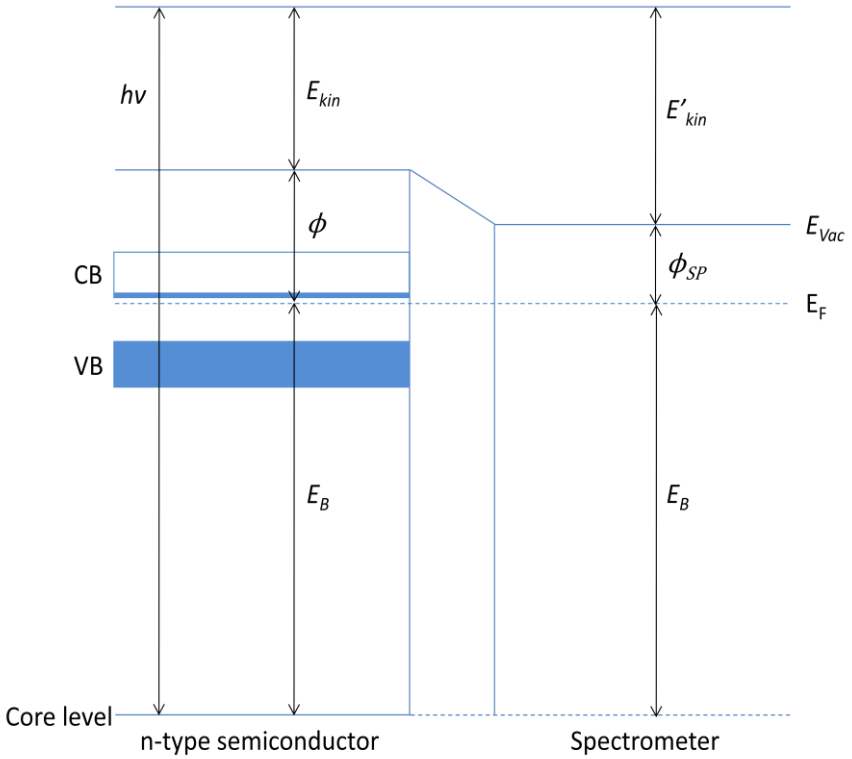


Figure 2.2. Energy level diagram for photoemission from a n-type semiconductor. Note that the level of the Fermi energy defined by the position of filled level at the bottom of the conduction band.

For n-type semiconducting samples such as TiO_2 the Fermi level is pinned by defect states at the bottom of the conduction band, as illustrated in figure 2.2.

2.1.1. Electron Mean Free Path and XPS sampling depth.

Soft X-rays may penetrate several hundreds of nanometres into a solid, so that photoelectrons are generated with a significant flux quite deep into the bulk of the solid. However, the electrons may be inelastically scattered as they propagate toward the surface. The electron mean free path λ is a measure of the mean distance that an electron travels before suffering an inelastic scattering event inside a solid. The photoelectron flux is attenuated from a value I_0 at a distance d beneath the surface to a value I at the surface according to a Beer Lambert type attenuation law

$$I = I_0 e^{-d/\lambda}.$$

90% of flux comes from a region within 3λ of the surface. Figure 2.3 shows the electron mean free path λ as a function of kinetic energy for a few selected materials.[3] It can be seen that in the kinetic energy range of interest in XPS measurements (5 eV to 1500 eV) the mean free path of electrons varies from about 5 Å to 15 Å. This means that the peaks in X-ray photoelectron spectra are due to those electrons generated within the first few atomic layers of the material. This gives rise to the characteristic surface sensitivity of XPS when applied to solids.

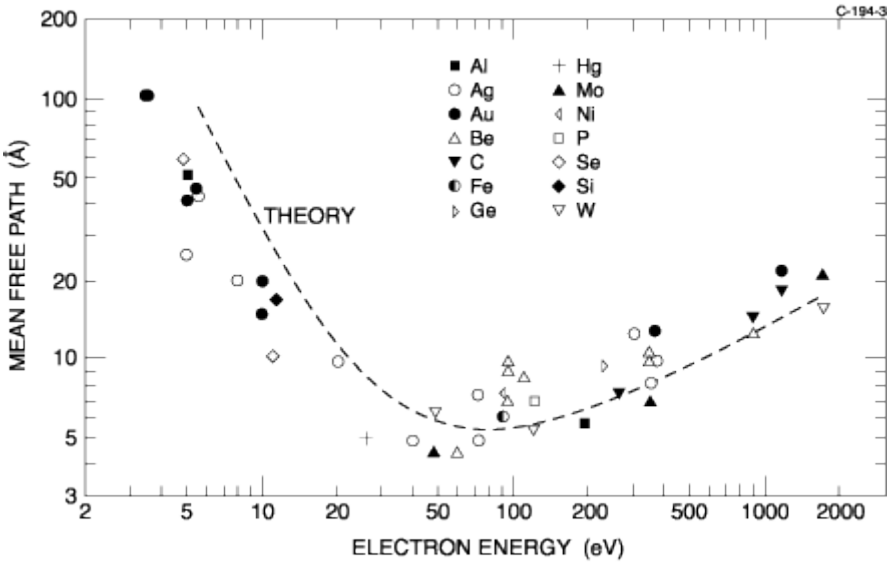


Figure 2.3. Mean-free paths in different elements as a function of kinetic energy. The general trend is called "universal curve" since the data shows no systematic dependence on the nature of the solid.

X-ray photoelectron spectroscopic methods for the study of solids have grown parallel to the development of routine techniques to obtain ultra-high vacuum (UHV) conditions. Given the low values of electron mean free paths it can be seen that in order to obtain information about the intrinsic properties solids, atomically clean surfaces are required so as to prevent interferences from adsorbed contaminants. UHV conditions are needed to keep solid surfaces clean over an extended time span so that meaningful measurements can be carried out. For example, with a sticking coefficient $S = 1$ (which means that every molecule or atom that impacts on a surfaces also sticks there) a contaminant monolayer would build up in about 1000 seconds at a pressure of 10^{-9} torr. Sticking coefficients close to one are common for very reactive surfaces like alkali metals. However, sticking coefficients on oxide surfaces for residual UHV gases such as H_2 and CO are much lower than one so that pressure up to 10^{-9} torr are adequate for XPS experiments extending over several hours.

2.1.2. Some fundamental aspects of core electron spectra

(a) *Binding energy in solids: the equivalent core approach*.

A rigorous theory of binding energies makes use of first principle methods to calculate the difference between the total energy of a final state (N-1) and its initial *ground* state N.[3] However, a simple approach for the estimation of the changes of binding energies of core electrons in ionic solids referring only to macroscopic thermodynamic quantities is based on a Born-Haber cycle and the so-called equivalent core approximation.

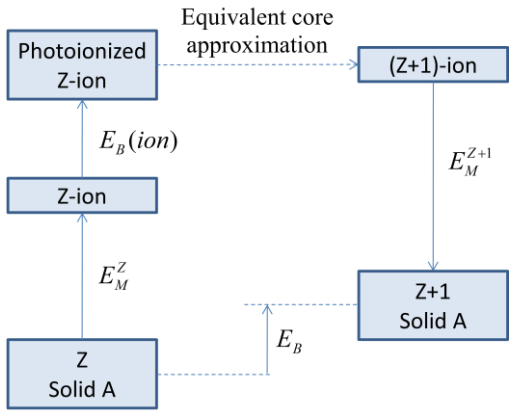


Figure 2.4. Born-Harber cycle describing photoionization of an insulator, which includes the equivalent core approximation.

Figure 2.4 depicts this method for a crystalline insulator. If an ion of nuclear charge Z is taken out of the solid, its energy changes by the Madelung energyE_M^Z. The resulting free ion is then photoionized, a process that requires the binding energy of the orbital under consideration in the free ion E_B(ion). In the "equivalent core approximation", the photoionized ion is a approximated by a (Z+1)-ion: the equivalent-core approximation model assumes that provided the spatial extension of a core electron is small compared to that of the valence electrons, the photoionization of a core level can be approximated

by the hypothetical addition of a proton to the nucleus. The ion is put back into the lattice, gaining the Madelung energy for the (Z+1)-ion. The sum of the energies of the cycle estimates the binding energy measured by XPS for the chosen orbital in the solid. It is the sum of the binding energy of that orbital in the free ion and the Madelung term for unit charge.

(b) *Chemical shifts*.

In XPS studies of solids, the absolute binding energy of a particular core level helps to identify an element but is of less interest than the change in binding energy between two different chemical forms the same atom. This energy difference is called the *chemical shift*.

Siegbahn et.al. have shown that chemical shifts are simply related to the effective charge at the atom.[4] In general, the higher the formal oxidation state of an atom and the higher the electronegativity of atoms in its coordination environment, the higher the binding energy of its core electrons. Consider the simple case of the 1*s* core level in Li.[3] In elemental lithium metal, the 2*s* electrons form a band which is delocalised throughout the solid with significant 2*s* electron density on each Li site. However, in lithium oxide Li_2O each lithium atom effectively donates its 2*s* electron into the oxygen 2*p* shell, so that the Li 2*s* electron density on a lithium atom is much reduced. The 1*s* electrons in lithium oxide therefore experience a stronger Coulomb interaction with the nucleus than in the metal, where the $1s^2$ shell is partially screened from the nucleus by the 2*s* valence electrons. Therefore the binding energy of the Li 1s level is larger in Li_2O than in Li metal, and a chemical shift is observed in the spectra.

Chemical shifts in crystalline solids are in general less predictable than in molecules because final state screening and the Madelung potential can greatly vary from one material to another. In general however the expectation that core level binding energies increase with the oxidation state is normally fulfilled. Typical examples are found in the oxides of Ti, V, Nb and W where the binding energy is highest for the group oxidation state, but there are some simple cases which violate this rule, for example the oxides of Sn and Pb.[5-7] The inversed shift from PbO to PbO_2 has been shown to arise from a difference in the Madelung potential.[6,7]

(c) *Spin-orbit coupling splitting*.

Spin-orbit coupling is the interaction of the spin magnetic moment of an electron with the magnetic field caused by its own orbital motion relative to the nucleus. The total angular momentum of an electron is the vector sum of its spin and orbital momenta, and can be expressed in the form

$$\hat{j} = \hat{l} + \hat{s}$$

This coupling breaks the spin degeneracy of electrons in a particular orbital to produce two states with $|j| = \left|l \pm {}^{1}/_{2}\right|$, each of which has $2j + 1$ degenerate substates characterized by m_j values $j, j-1 \ldots -j$. For $l = 0$ (*s* orbital), the only permitted value of j is $j = {}^{1}/_{2}$ due to the lack of any other source of momentum in the system apart from that of the spin angular momentum. When $l = 1$ (*p* orbital), j is either ${}^{3}/_{2}$ or ${}^{1}/_{2}$ producing 4 and 2 m_j substates respectively. Therefore photoemission from an electronic state with non-zero orbital angular momentum produces a "spin-orbit doublet"; as exemplified by the Ti 2*p* spectrum of TiO_2 shown in figure 2.5. The two

signals correspond to Ti 2*p* states with $j = {}^{1}/_{2}$ and $j = {}^{3}/_{2}$. The intensity ratio is given by the ratio of degeneracies, i.e. $\frac{2\left(1+\frac{1}{2}\right)+1}{2\left(1-\frac{1}{2}\right)+1} = \frac{3+1}{1+1} = 2:1$

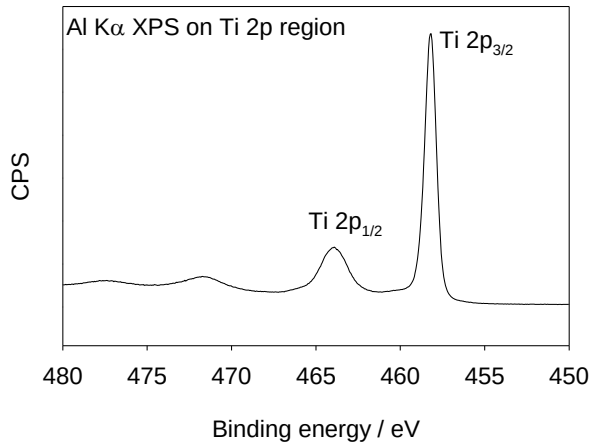


Figure 2.5. Photoemission spectrum of TiO_2 over Ti 2p region. Spin-orbit coupling splits the peak into two.

(d) Intensities

Lines intensities (or areas) in XPS are of interest for quantitative surface chemical analysis. The intensity ratio between two peaks from different elements A and B in XPS of a homogenous material are proportional to the relative concentrations A and B.

$$\frac{I_A}{I_B} = \frac{[A]\sigma_A\zeta_A\lambda_A\eta_A}{[B]\sigma_B\zeta_B\lambda_B\eta_B}$$

where the σ are the photoelectric cross sections, the ζ are the fraction of photoionisation events free from intrinsic plasmon or other satellite excitation, the λ are electron mean free-paths and the η are the kinetic energy dependent transmission terms of the spectrometer detection system.

Satisfactory theoretical cross section values σ can be found in the literature. Alternatively it is possible to use empirical atomic sensitivity factors which group together the four terms discussed above.[8-11] Values of the mean free-path λ may be estimated from "universal curve" shown in figure 2.3. η is a parameter that depends on the electron optics of the spectrometer. For example, in spectrometers employing retardation, η is roughly proportional to the reciprocal of the kinetic energy.[1] On the other hand, ζ is difficult to estimate in solids since intrinsic loss structure, due for example to plasmon excitation, is superimposed on structure due to extrinsic loss making the two difficult to untangle. The simplest assumption is to set ζ to 1. This assumption introduces a significant error in calculations since ζ is not necessarily the same for two elements in a compound. For example, in a metal oxide such as MgO with an O 2*p* - derived valence band, intrinsic plasmons are more likely to be excited during emission from an oxygen 1*s* core level than during emission from Mg core states, which would lead to an underestimation of the oxygen concentration. This makes truly quantitative chemical analysis very difficult.

2.1.3. *Some fundamental aspects of valence band electron spectra*

The treatment of valence-level photoemission involves two new considerations.[12] The first is that the electronic states are characterised by both energy and wavevector, and the photoemission process involves *k* conservation. This forms the basis for angle resolved PES of single crystals. Obviously issues of *k* conservation can be largely ignored when dealing with photoemission from polycrystalline samples. Also at high photon energies unless very special care is taken to measure spectra over a narrow angular range, spectra will usually sample the whole of Brillouin Zone. The second is that electronic states at a given energy will in general involve a mixture of atomic

orbitals from the different atoms contributing to the valence levels. At sufficiently high photon energies (typically ~1 keV or above) the Gelius model[13] provides a simple way of calculating the valence level spectra.

The model was first developed to deal with molecular systems. The model can be quantified in terms of cross-sections for constituent atomic orbitals within a molecule, in which the cross section σ_j^{MO} for the j^{th} MO is given by:

$$\sigma_j^{MO} = \sum_{A,i} P_{j,iA}\sigma_i^A$$

Where σ_j^A are one electron atomic cross-sections. The summation extends over different atomic orbitals (*i*) at different atom centres (A), and so the $P_{j,i,A}$ are factors describing the weight of the contribution of the atomic orbitals to the molecular orbitals. If the basis set is properly orthonomalised for different atomic centres it follows that $P_{j,i,A} = (c_{j,i,A})^2$

In a similar way, for solids the total density of states $N_{tot}(E)$ at energy E, may be broken down into contributions from different atomic orbitals (i) on the different atoms (A) present in the solid so we have a sum of partial densities of states.

$$N_{tot}(E) = \sum_{i,A} N_i^A(E)$$

The Gelius model now gives:

$$N_{tot}^W(E) = \sum_{i,A} N_i^A(E)\sigma_i^A$$

2.2. Diffuse Reflectance Spectroscopy (DRS)

The simple theories of absorption spectroscopy applicable to dilute species in the gas phase or in solution consider only absorption and transmission of light. Solids however show strong reflectivity of light; indeed it is often only possible to study the optical properties of solids by light reflected from surfaces, rather than transmitted.[14] This is especially true for powders where there is a high surface to volume ratio.

The behaviour of light at the interface of a solid is determined by the complex refractive index ($\tilde{n}$), which provides information about absorption, refraction and reflection and is defined through:

$$\tilde{n} = n + ik$$

where n is refractive index and k is the extinction coefficient. The fraction of light reflected back (R) from a solid at normal incidence under conditions of specular reflection is given by the formula:

$$R = \left|\frac{\tilde{n} - 1}{\tilde{n} + 1}\right|^2 = \frac{(n-1)^2 + k^2}{(n+1)^2 + k^2}$$

This relationship is the basis for the study of the optical properties from reflectivity measurements.[15]

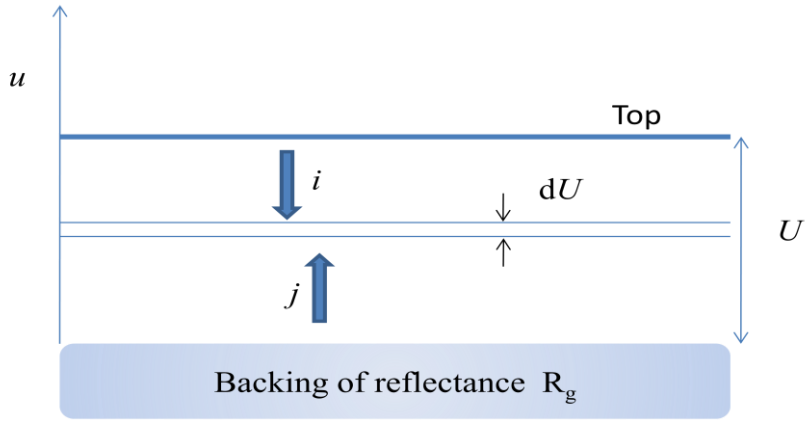


Figure 2.6. Schematic diagram of a cross section of a layer of a material

In 1931 Kubelka and Munk gave a theoretical treatment of diffuse reflection from rough surfaces that resulted in very useful expression to calculate an approximate absorption spectrum.[16] The theory assumes that a material layer of thickness U, capable of both scattering and absorbing electromagnetic radiation, is irradiated in the u direction with a diffuse monochromatic radiation flux as shown in figure 2.6. The model considers two fluxes: one downward (i) and the other upward (j). On passing through a differential of U, $\mathrm{d}U$, the i flux decreases by an amount $Ki\,\mathrm{d}U$ due to absorption and $Si\,\mathrm{d}U$ due to scattering, which partially reverses the direction of the flux to form the j flux. The K and S values are related to the absorption and scattering coefficients, respectively. In summary, the changes in the upward and downward fluxes can be written as:

$$dj = -(S+K)j\,dU + Si\,\mathrm{d}U$$

$$-di = -(S+K)i\,dU + Sj\,\mathrm{d}U$$

dj and di show different algebraic signs because of the different directions of the two fluxes.

Kubelka obtained explicit hyperbolic solutions for these equations.[17] The most general solution is

$$R = \frac{1 - R_g(a - bcoth\ bSU)}{a - R_g + b\coth bSU}$$

where R is the reflectance from the layer over a background reflectance R_g, $\coth bSU$ is the hyperbolic cotangent of bSU, a is $(1 + {}^{K}/_{S})$ and b is $\sqrt{a^2 - 1}$.

In the limiting case of the layer being thick enough that further increase in thickness does not change the reflectance, the background has no influence and the equation becomes:

$$R = \frac{S}{K + S\sqrt{K(K + 2S)}}$$

that can be rewritten as:

$$\frac{K}{S} = \frac{(1 - R)^2}{2R} = F(R)$$

According to Kubelka-Munk theory K and S are parameters that vary linearly with the absorption (α) and scattering (*s*) coefficients respectively. This last expression is widely used for the study of optical properties of ceramic and powder materials, as well as soils. However, the Kubelka-Munk function has been found to fail in the description of systems composed by an absorption-dominated material and a scattering-dominated one such as ink-paper. In order to take account of this, a revised theory has been proposed that includes a statistical analysis of light propagation, thus taking into

account the effect of scattering on the path length of light propagation (path variation). This leads to new relationships between K and S coefficients and the intrinsic absorbing (α) and scattering (s) coefficients of a material that indicate a nonlinear dependence.[18] Nevertheless, the Kubelka-Munk function remains as most popular method of analysing diffuse reflectance data from powder materials.

2.3 Electron Spin Resonance Spectroscopy.

2.3.1 General considerations

The electron has a magnetic moment due to its spin, and in presence of an external applied field the two permitted orientations, say β and γ, have different energies. The electron spin resonance (ESR) experiment is the observation of the energy required to reverse the direction of an electron spin in the presence of a magnetic field. An electron can be induced to reverse its orientation if electromagnetic radiation of the appropriate frequency is applied. For example if a free electron is placed in a 3000 G magnetic field, the spin up β-state would lie 0.3 cm^{-1} above the spin down γ-state, which matches with the energy of electromagnetic radiation with a frequency of around 9 GHz. This is in the so-called X-band region of the microwave spectrum. An X-band ESR spectrometer consists of a magnet capable of producing a homogeneous magnetic field in the vicinity of 3000 G, a source of microwave in the X-band region and a detector of microwave intensity. In the ESR experiment microwave radiation of a constant frequency is fed into a resonant cavity containing the sample and the magnetic field is swept until the incident radiation is absorbed, as shown in figure 2.7. At this field the separation between β and γ states exactly matches (or is in resonance with) the

radiation frequency.[19] In most ESR experiments the applied field is subject to a small modulation and lock in techniques are used to measure the derivative of the absorption spectrum.

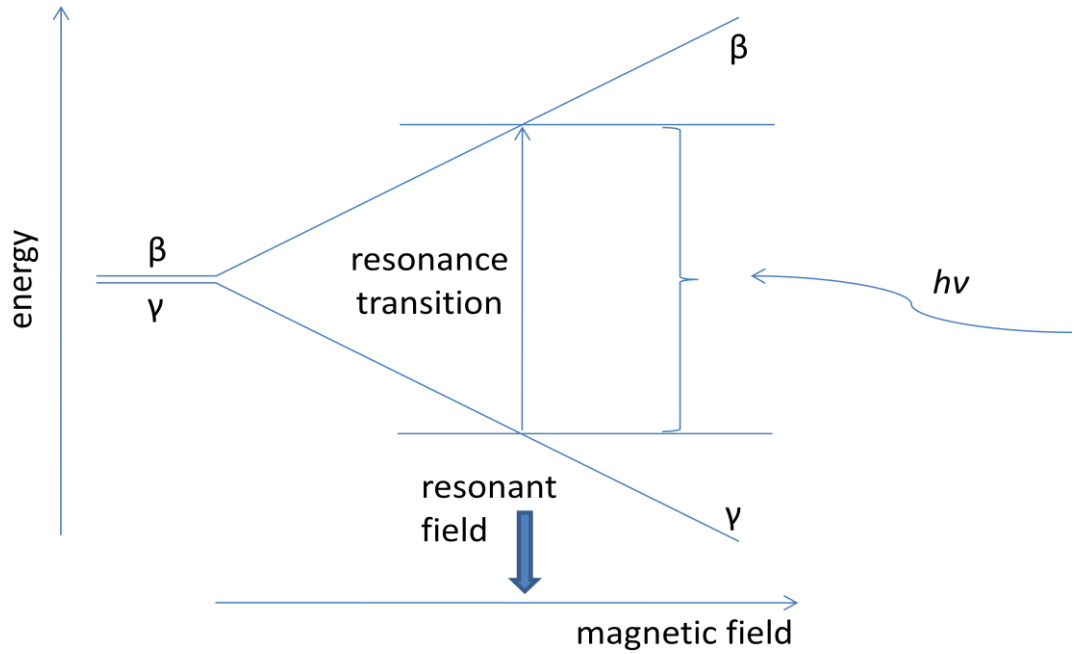


Figure 2.7. Schematic diagram of an electron spin resonance transition.

The essential pieces of information that emerge from an ESR experiment are the following: (1) the position of the spectrum in a field sweep; (2) hyperfine structure in the spectrum; and (3) the shape of the spectral lines.

2.3.2 Position of the spectrum

An unpaired electron will absorb microwave radiation of frequency ν at a applied field B when

$$g\mu_B B = h\nu$$

where μ_B is the Bohr Magneton $(e/2m)\hbar$ and the so called g factor defines the relationship between the magnetic moment of the electron and its angular momentum. For a free electron the angular momentum comes entirely from spin and has a value $\hbar\sqrt{S(S+1)}$ where S=1/2. The Dirac equation predicts that the g value associated with electron spin should be 2.00, although this value is modified to 2.002319 due to quantum electrodynamic effects. For angular momentum associated with orbital motion of an electron g = 1.00. The orbital angular momentum found for free atoms is quenched to varying extents in molecules and solids and in general g values can take on a range of values dependent on the orbital contribution to the angular momentum. For most organic free radicals g values are usually close to 2.0 but for transition metal or lanthanide ions g values span a much wider range. In solids where the site associated with the unpaired electron has lower than cubic symmetry the g-factor may show anisotropy, in which case the resonance condition depends on the orientation of the paramagnetic species in the crystal relative to the external field.

2.3.3 Hyperfine structure

Hyperfine interactions between the electron spin and magnetic moments associated with nuclei where $I \neq 0$ magnetic give a splitting of the ESR signal into $2I$ + 1 components. The nuclear magnetic moment gives rise to a local magnetic field, which can increase or decrease the local field experienced by the electron spin. This means that the ESR spectrum of a hydrogen atom will have a pair of lines, instead of one characterized by the resonant field $B_r = h\nu/g\mu_B$. For a proton $I = 1/2$, and M_I has

the two allowed values $M_I = \pm 1/2$. Therefore at the electron there will be two possible local values for the field and the resonance is split into two peaks. In the case of ^{14}N $I = 1$ and $M_I = -1, 0, 1$, so that a paramagnetic species containing such a nucleus should display three signals. The separation between the lines that define the hyperfine structure depends on the amplitude of the spatial wavefunction of the orbital occupied by the unpaired electron at the magnetic nucleus.

The hyperfine structure has both isotropic and anisotropic components. The isotropic structure is characteristic of *s*-orbitals and is a consequence of the nonzero probability of finding *s*-electrons at the nucleus as described by the Fermi contact interaction. Anisotropic hyperfine interactions involve orbitals of higher angular momentum.

2.3.4 ESR spectra in the solid state

In ESR spectra from solution phase species, rapid molecular rotation ensures that the g-factor and hyperfine coupling constants are scalar constants of the system. However, solid state ESR spectra of non cubic materials are in general strongly dependent on the orientation of the crystalline axes with respect to the magnetic field. In a powder sample there is short-range order, but the principal axes of the paramagnetic system will assume all possible angles relative to the direction of the applied magnetic field. Even in absence of hyperfine splitting, the ESR spectrum of such samples will be spread over a field range ΔB determined by the principal components of the g tensor of the system.

An simple illustrative example is that of the resonance of a paramagnetic species in a site with axial symmetry in the absence of hyperfine splitting. B_r for such a species will vary between limits of $B_{||}$ (the field corresponding to $g_{||}$) and $B_{\perp}$ (the field

corresponding to $g_{\perp}$). The resonant field B_r for an arbitary angle θ between the axial symmetry axis and the magnetic field direction is given by [20]

$$B_r = \frac{h\nu}{g_{eff}\mu_B} = \frac{h\nu}{\mu_B}\frac{1}{(g_{||}^2 cos^2\theta + g_{\perp}^2 sin^2\theta)^{\frac{1}{2}}} \quad .$$

Wertz and Bolton derived an expression that describes the probability $P(B)$ of a randomly orientated sample with axial symmetry to be at a resonant field B between $B_{||}$ and $B_{\perp}$:[20]

$$P(B) \propto \frac{\mu_B}{h\nu}\frac{(g_{||}^2 cos^2\theta + g_{\perp}^2 sin^2\theta)^{\frac{3}{2}}}{(g_{||}^2 - g_{\perp}^2)cos\,\theta} \quad .$$

This can be simplified to:

$$P(B) \propto \left(\frac{h\nu}{\mu_B}\right)^2 \frac{1}{B_r^3\left(g_{||}^2 - g_{\perp}^2\right)\cos\theta}.$$

Owing to the $\cos\theta$ term in the denominator, $P(B)$ rises monotonically toward infinitity as $\theta \rightarrow {}^{\pi}/_{2}$. This condition represents a system with its principal axis perpendicular to the magnetic field. The discontinuity is removed when accoiunt is taken of broadening due to lifetime or other effects but nonetheless the distribution of signal intensity across the magnetic field range between $B_{||}$ and $B_{\perp}$ is not uniform, being more intense close to $B_{\perp}$. This behaviour is illustrated in figure 2.8 which shows an idealized absorption line

shape for a system with axial symmetry system and how this line shape evolves as a function of spectral broadening.

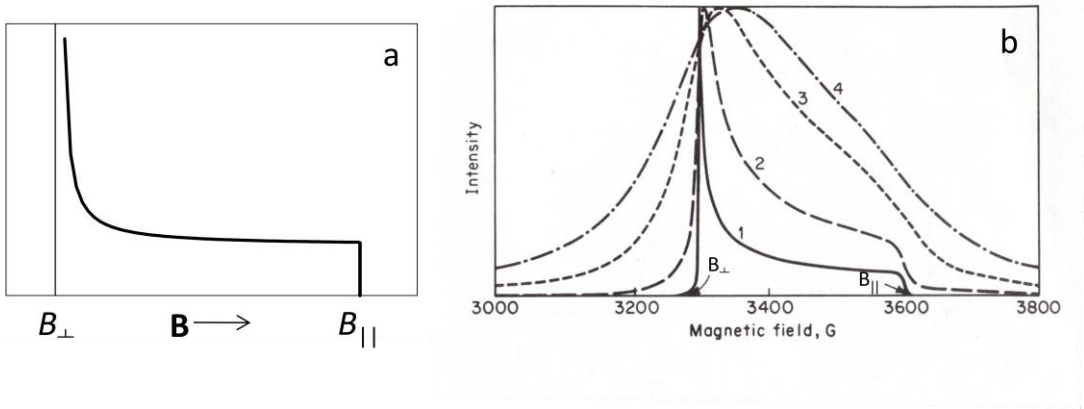


Figure 2.8. (a) Idealized absorption shape for a randomly orientated system having an axis of symmetry and no hyperfine interaction ($g_\perp > g_{||}$). (b) Computational simulation of a the line absorption shape for a randomly orientated system having axial symmetry. The component Lorentzian lines are given widths of 1, 10, 50 and 100G respectively.[20]

For an orthorhombic system there are three principal components of the g tensor giving schematic line shapes such as illustrated in figure 2.9. Here it is assumed that g_{YY} is intermediate between g_{ZZ} and g_{XX}. [21]

With inclusion of anisotropic hyperfine interactions the complexity of the spectra increases and computational simulation is usually required in order to extract useful information regarding the paramagnetic species from ESR spectra.

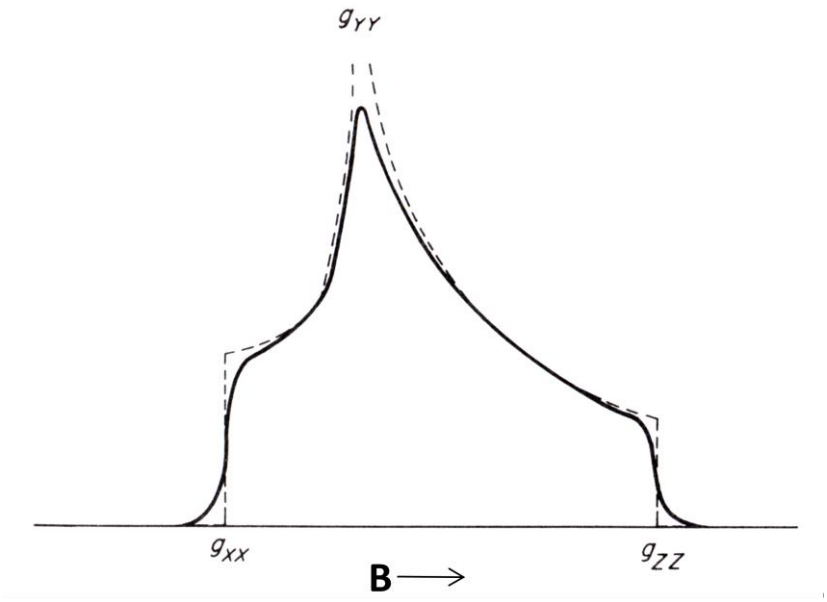


Figure 2.9. Idealized absorption shape for a randomly orientated system having orthorhombic symmetry and no hyperfine interaction (dashed line), and computational simulation of the line absorption shape for a randomly orientated system having orthorhombic symmetry (continue line).[20]

2.4 Raman spectroscopy.

2.4.1 General considerations.

The Raman process involves the inelastic scattering of light by matter. A photon may lose energy by electronic, vibrational or (for gases) rotational excitation to give rise to so-called Stokes structure; or photons may gain energy from thermally excited states to give anti-Stokes structure. There is always a strong elastically scattered Rayleigh line. The technique is applied most often to study vibrational excitations. Since vibrational modes are quantized the energy transfer is also quantised and the scattered light contains frequency components that are shifted from the incident frequency by discrete amounts. The frequency distribution of the scattered light constitutes the Raman spectrum of a species. Owing to the low cross sections for inelastic light scattering an intense radiation source is required, typically a laser operating in the visible region.

In Stokes scattering the incident electric fields produce an oscillating polarisation in the scattering medium, which then re-emits radiation at the incident frequency minus a vibrational frequency. Raman activity is governed by the *polarisability tensor,* which relates the dipole induced in x, y and z directions to electric fields E_x, E_y and E_z.

$$\begin{pmatrix} \mu_x \\ \mu_y \\ \mu_z \end{pmatrix} = \begin{pmatrix} \alpha_{xx} & \alpha_{xy} & \alpha_{xz} \\ \alpha_{yx} & \alpha_{yy} & \alpha_{yz} \\ \alpha_{zx} & \alpha_{zy} & \alpha_{zz} \end{pmatrix} \begin{pmatrix} E_x \\ E_y \\ E_z \end{pmatrix}$$

The components of the polarisability tensor transform like x^2, y^2, xy, xz etc. or linear combinations of them. Since xy and yx, xz and zx and yz and zy have the same transformation properties, there are 6 components of the polarisability tensor to worry about. One component is always totally symmetrical, whilst the other 5 components behave like the d orbitals. Raman active modes must transform as one component of the polarisability tensor and in centrosymmetric systems Raman active modes are therefore of gerade symmetry. This contrasts with infrared spectroscopy which probes ungerade modes transforming like x, y or z.

2.4.2 Raman scattering by crystalline solids

In the solid state, Raman scattering involves inelastic light scattering from optical phonons. Since a visible region photon has a low momentum, light scattering techniques can only probe phonons with wave vectors ($\boldsymbol{q}$) close to 0.[15] Therefore, Raman scattering gives little information on the dispersion of the optical phonons and its main use is to determine frequencies of transverse and longitudinal optical phonons near the centre of the Brillouin zone of the crystal where $\boldsymbol{q} \approx 0$. Raman spectroscopy

may be applied as a finger printing technique for qualitative identification of crystalline phases.

2.5 Atomic Force Microscopy

Atomic force microscopy (AFM) is a scanning probe microscopy (SPM) technique where a sharp probe is scanned on or close to a surface of the sample while the force between the probe and the sample is monitored. Typically the probe is attached to the free end of a cantilever and is brought very close to a surface. Attractive or repulsive forces resulting from interactions between the probe and the surface will the cantilever to bend. The displacement is detected by means of a laser beam, which is reflected from the back side of the cantilever. The lateral scanning is controlled by means of piezoelectric crystals, which are ceramic materials that expand or contract in the presence of an applied field, and conversely, they develop an electrical potential in response to mechanical pressure. Typically a feedback loop is used to control the z displacement so as to maintain a constant force or constant displacement.

There are three modes in which AFM can be operated: contact mode, tapping mode and non-contact mode.

2.5.1 Contact mode AFM

Contact mode AFM operates by scanning a tip attached to the end of a cantilever across the sample surface while monitoring the change in cantilever deflection with a split photodiode detector as schematically shown in figure 2.10. When AFM is performed under ambient conditions, the tip contacts the surface through an adsorbed fluid layer on the sample surface that could be just air or liquids. A feedback loop maintains a constant distance between the cantilever and the sample by vertically moving the

scanner at each (x,y) data point to maintain a set deflection so that the force between the tip and the sample, which normally ranges from 1 nN to 1 μN, remains constant. The distance the scanner moves vertically (z) at each (x,y) data point is stored in a computer and used to construct a topographic image of the sample surface.

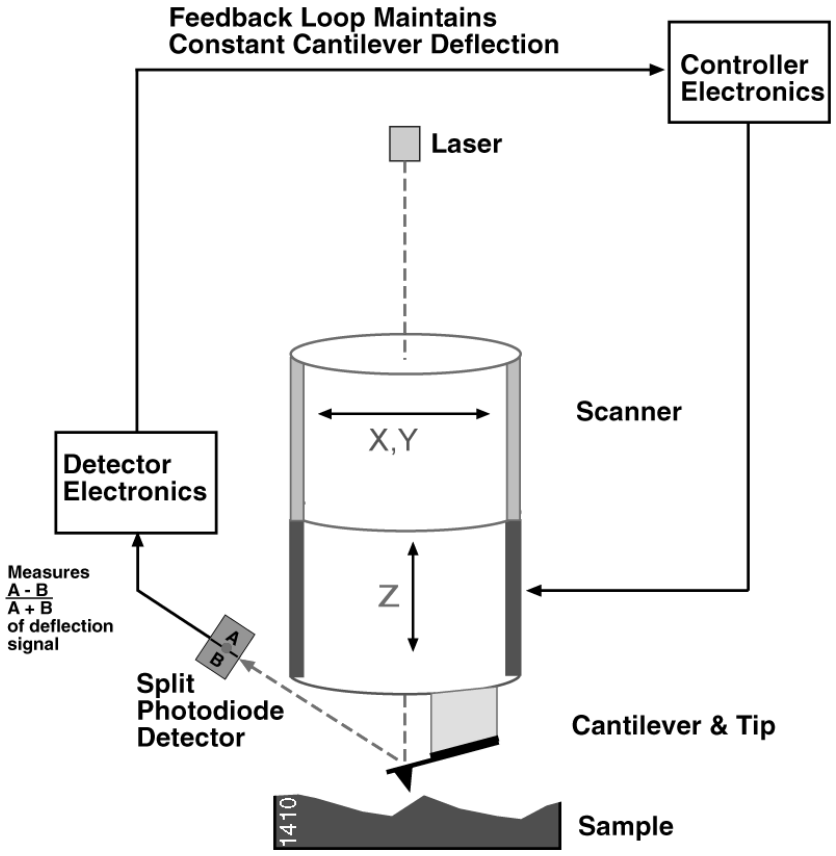


Figure 2.10. Scheme of an AFM apparatus showing the feedback loop used in contact mode.[22]

Contact mode AFM allows study of rough samples. However, lateral forces can distort features in the image. Also, forces normal to the tip-sample interaction can be high in air due to capillary forces from the adsorbed fluid layer on the sample surface, which combined with lateral forces can result in reduced spatial resolution and may damage soft samples (such as biological samples, polymers or silicon) due to the scraping between the tip and sample.

2.5.2 Tapping mode AFM

The tapping mode AFM operates by scanning a tip attached to the end of an oscillating cantilever across the sample surface. The cantilever is oscillated at or close to its resonance frequency with an amplitude ranging typically from 20nm to 100nm. The tip lightly taps on the sample surface during scanning, getting in contact with the surface at the bottom of its swing as shown in figure 2.11. In this case the feedback loop maintains a constant oscillation amplitude by maintaining a constant RMS of the oscillation signal acquired by the split photodiode detector so that a constant tip-sample interaction is maintained during imaging. The vertical position (z) of the scanner at each (x,y) data point in order to maintain a constant set amplitude is stored by a computer to construct the topographic image of the sample surface.

Tapping mode AFM offers the advantages of higher lateral resolution on most samples (1 nm to 5 nm) and less damage to soft samples imaged in air as lateral forces are virtually eliminated and forces normal to the tip-sample interaction are less strong, so there is no scraping. However, the images must be recorded at a slower scan speed than contact mode AFM.

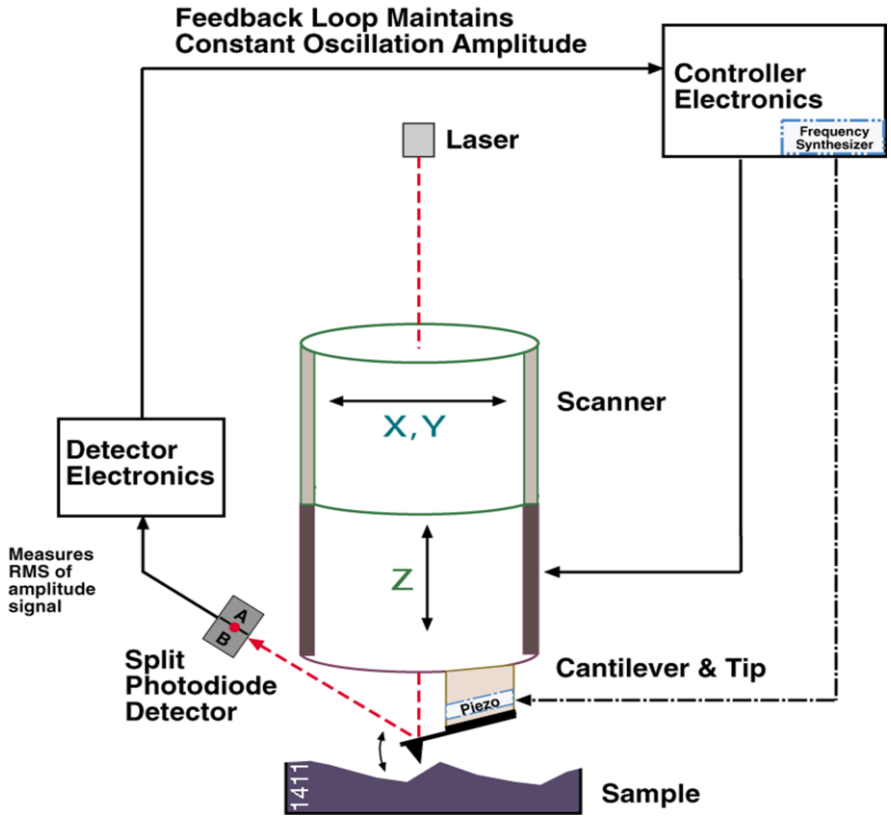


Figure 2.11. Scheme of an AFM apparatus showing the feedback loop used in tapping mode.[22]

2.5.3 Non-contact mode AFM

In non-contact mode, the cantilever is forced to oscillate at a frequency which is slightly above the resonance frequency, typically with an amplitude of a few nanometers (<10nm), in order to obtain an AC signal from the cantilever. The tip does not contact the sample surface, but oscillates above the adsorbed fluid layer on the surface during scanning, as shown in figure 2.12. In the proximity of a surface the resonant frequency is reduced by van der Waals forces which extend from 1 nm to 10 nm above the adsorbed fluid layer, and by other long range forces which extend above the surface. The decrease in resonant frequency causes the amplitude of oscillation to decrease. The feedback loop maintains a constant oscillation amplitude or frequency by vertically (z) moving the scanner at each (x,y) data point until the set amplitude or

frequency is reached. The distance the scanner moves vertically (z) at each (x,) data point is stored by the computer to form the topographic image of the sample surface.

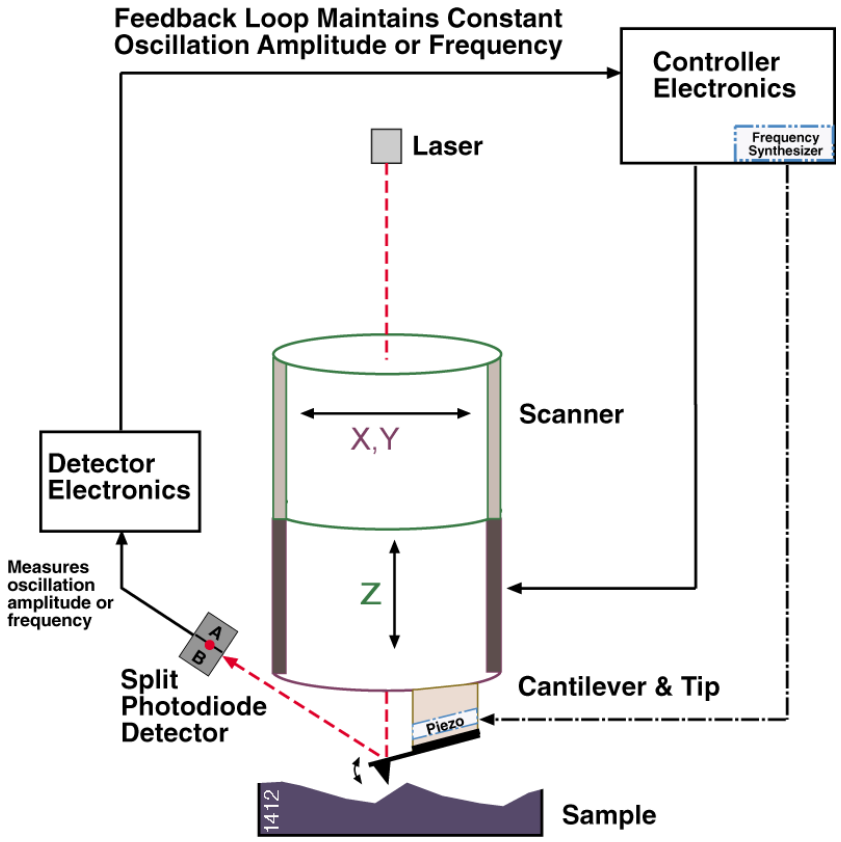


Figure 2.12. Scheme of an AFM apparatus showing the feedback loop used in non-contact mode.[22]

Although the non-contact AFM mode brings about the advantage of not exerting any force on the sample surface, applications for non-contact mode AFM imaging in ambient conditions have been limited because of low lateral resolution and the need for slower scan speeds than in tapping mode or contact mode imaging. Also, the non-contact AFM mode usually only works on extremely hydrophobic samples, where the adsorbed fluid layer is at a minimum. If the fluid layer is too thick, the tip becomes trapped in the adsorbed fluid layer causing unstable feedback and scraping of the sample.

2.6 Powder X-ray diffraction

X- rays irradiating a crystal are scattered in a specular fashion by atoms in lattice planes of the crystal. X-rays scattered from successive crystallographic planes (hkl) will interfere constructively if the path length difference is equal to an integer multiple of the wavelength. The path difference between two waves undergoing constructive interference is given by $2d\sin\theta$, as illustrated in figure 2.13. This leads to Bragg's law in the form:

$$n\lambda = 2d_{hkl}sin\theta$$

where λ is the wavelength of the X-ray and θ is the incidence angle and d_{hkl} the characteristic interplanar spacing of a set of planes with hkl Miller index.

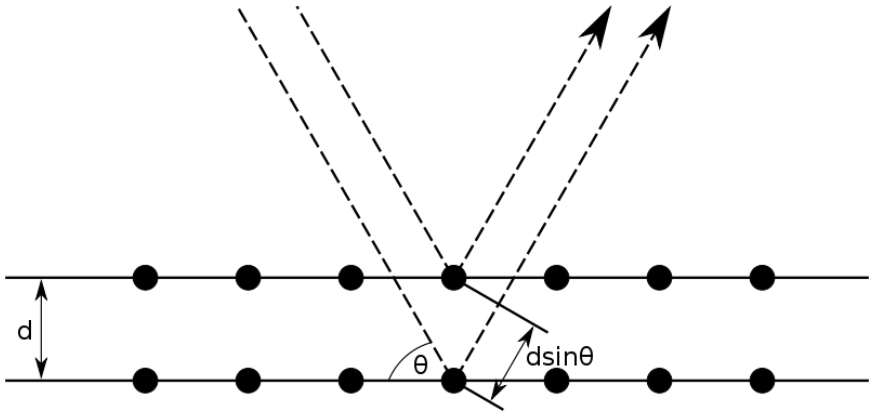


Figure 2.13. Bragg's diffraction.

Diffracted X-ray beams make an angle of 2θ with the incident beam. Because the crystallites can lie in all directions while still maintaining the Bragg condition, the reflections lie on the surface of cones whose semi-apex angles are equal the reflection angles 2θ. The diffraction pattern of a powder sample is taken in automatic diffactometers that use scintillation or CCD detectors to record angle and intensity of the diffracted beams. The source of the X-rays, the sample and the detector are placed in a Bragg-Brentano (θ-2θ) arrangement that utilizes a parafocusing geometry to

increase intensity and angular resolution, as shown in figure 2.14. The sample at the centre of the diffractometer circle *O* rotates in such a way that the specimen remains tangential to a focusing circle where the angle between the X-ray source (*S)*, sample (*O*) and focusing point (*F*) at the detector doubles the incident angle throughout the scan.

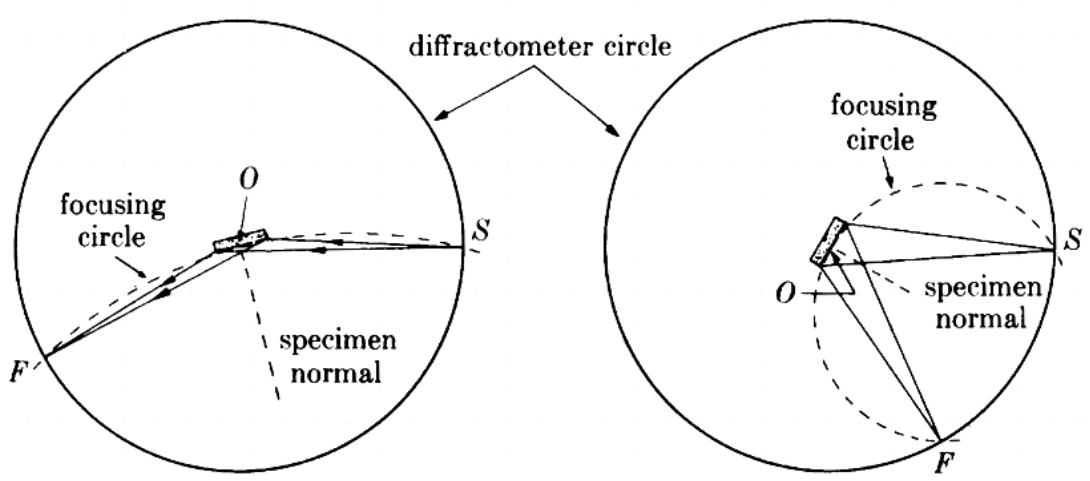


Figure 2.14. Parafocusing geometry of the Bragg-Brentano diffractometer. *O* is the centre of the diffractometer circle, *S* represents the source of X-ray and *F* the focusing point at the detector

The X-ray powder diffraction of a compound provides a convenient and characteristic fingerprint which can be used in qualitative analysis. Values of d_{hkl} spacings line intensities can be compared with those listed in the Powder Diffraction File, which contains entries for more than 500,000 inorganic compounds over 400,000 organic compounds, up to year 2010.[23] The lattice parameters are readily obtained from d_{hkl}-spacings with the help of computer programs that have been developed for this purpose, although for cubic and tetragonal systems simple manual analysis is possible.[24]

Powder X-ray diffraction data are also useful in the analysis of the relative concentration of different phases in a mixture and in the elucidation of phase diagrams.

The phases of a mixture can be identified using the procedure describe above, and their proportions can be determined by comparing the intensities of the characteristic lines from each phase to those from a standard. Additionally when phases are soluble in each other, the solubility limits can be determined by following the shifts of the cell parameters

2.7 Transmission Electron Microscopy

Electron microscopy exploits the short wavelength of high energy electrons to achieve spatial resolution superior to that of optical microscopy. In transmission electron microscopy (TEM) electrons generated by thermionic emission are accelerated to a kinetic energy of around 100 KeV or greater and pass through a thin slice of sample. The de Broglie wavelength at 100 KeV is about 0.037 Å. Electrons are scattered by the atomic potentials of the atoms in the specimen and form a diffraction pattern. The pattern can be directly transformed into an image by magnetic lenses. Either the diffraction pattern or the real space image can be projected onto a viewing screen, as shown in figure 2.15. Single-crystal diffraction patterns can be obtained by appropriately orientating a specimen of thickness under 1 μm. It is possible to select individual crystallites from a powder sample, and produce single crystal diffraction patterns.[25]

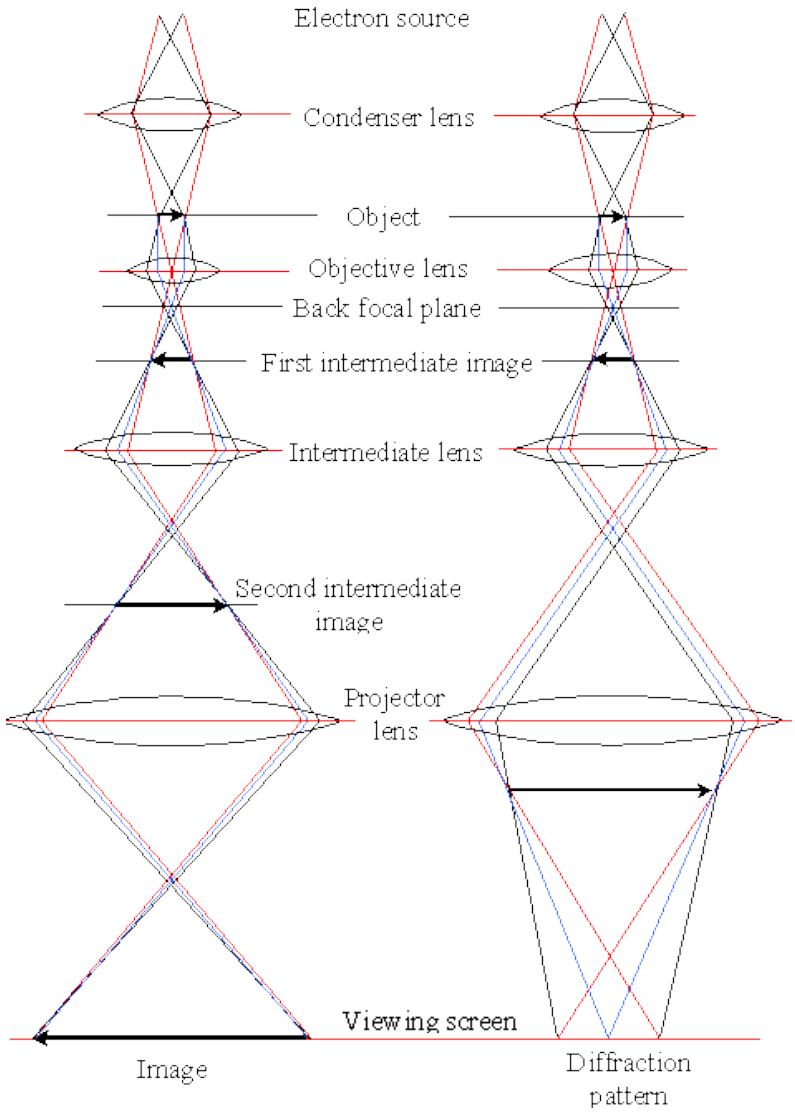


Figure 2.15. Ray diagrams for the generation of images (left) and diffraction patterns (right) in a transmission electron microscope.

It is possible to obtain images with atomic resolution by permitting an optimum number of diffracted beams to contribute to the image. The resolving power d_{min} depends on both wavelength and the quality of the objective lens, which produces the first image, as

$$d_{min} \propto C_S^{\frac{1}{3}} \lambda^{\frac{2}{3}}$$

C_S is a lens parameter called spherical abberation coefficient. The image will also be sensitive to the thickness of the crystal and the focusing conditions.

2.8 Surface area determination by physisorption analysis

When a surface is formed from a bulk material chemical bonds are broken. The formation of new bonds with gas phase species gives rise to chemisorption. However, even in the absence of specific chemical interactions, a gas will in general adsorb on the solid surface of a material due to weak van der Waals type interactions. The volume of adsorbed gaseous species will depend on both pressure and temperature as well as the surface area of the solid. After saturation of the first monolayer of adsorbate, further adsorption may occur on top of this layer, but typically with a lower heat of adsorption.

Surface area determination by gas adsorption involves determination of the volume of an inert gas (typically nitrogen) adsorbed on a solid surface at low temperatures as a function of increasing pressure. Any possible hysteresis is revealed by also recording adsorbed volume as the pressure is reduced back to zero. Six standard types of adsorption isotherm defined by IUPAC are shown in figure 2.16. The Type I isotherm is typical of systems where there is strong chemisorption which saturates at one monolayer coverage. This type of isotherm may also be observed for microporous solids. Type II isotherms are typical of physisorption on finely divided non-porous solids where multilayers may build on top of the first adsorbate monolayer. Type III and type V isotherms are typical of adsorption where the heat of adsorption onto the adsorbate itself exceeds the heat of adsorption onto the substrate, as found with water on hydrophobic materials. Type VI and V isotherms feature a hysteresis loop generated by the capillary condensation of the adsorbate in the mesopores of the solid. Finally, the

rare type VI step-like isotherm is shown by nitrogen adsorption on some carbonaceous materials.[26]

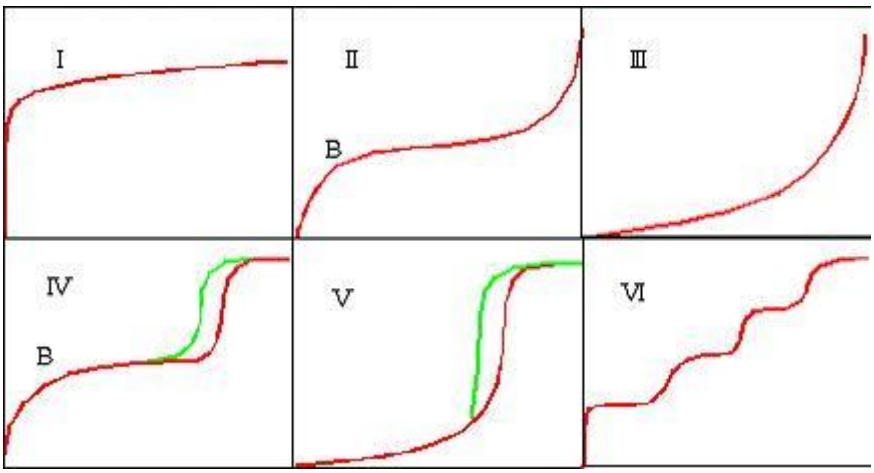


Figure 2.16. Six standard types of adsorption isotherm defined by IUPAC.

If adsorption saturates at monolayer coverage the surface area is easily determined from the Langmuir adsorption isotherm which assumes that equilibrium coverage is achieved when rates of adsorption and desorption are equal.[26] However, the most common method of measuring the surface area of powder is that developed by Brunauer, Emmett and Teller using the so called BET method.[27] In essence, the BET isotherm is an extension of the Langmuir isotherm that also considers multilayer adsorption. As in the Langmuir approach the heat of adsorption for the first monolayer is assumed to be independent of coverage. The heat of adsorption for layers other than the first is assumed to be equal to the heat of liquefaction of the adsorbed gas. Summation over an infinite number of adsorbed layers gives the final expression

$$\frac{P}{V(P_0 - P)} = \frac{1}{V_m C} + \frac{(C-1)P}{V_m C P_0}$$

where V is the volume of gas adsorbed at pressure P, V_m is the volume of the monolayer, P_0 is the saturation pressure of the absorbate, and C is a constant related exponentially to the heats of adsorption and liquefaction of the adsorbate as

$$C = e^{(q_1 - q_L)/RT}$$

where q_1 is the heat of adsorption of the first layer and q_L is the heat of liquefaction of the asorbate. In general the larger the value of C the more the isotherm approaches the type II form and the more accurate the surface area can be determined.

According to the BET isotherm defined above, plots of $P/V(P_0 - P)$ versus P/P_0 should give straight lines whose slope and intercept can be used to evaluate V_m and C. From volume of the monolayer (V_m) and the cross-section area of the absorbate the total surface area of the absorbent can be estimated.

2.9 Photocatalytic model tests

As discussed in chapter 1, organic molecules may be oxidised by the holes generated by photoexcitation in a wide gap semiconductor while oxygen is reduced by the electrons promoted to the conduction band. Although interest may ultimately fall on destruction of organic pollutants, dyes are commonly used as probe molecules in screening for photocatalytic activity, mainly because their concentration can be easily monitored using visible region absorption spectroscopy. Methylene blue and methyl orange have been widely used in the field of oxide photocatalysis[28-34] Their structures are shown in figure 2.17. Although in an idealised picture dye oxidation involves complete mineralisation of the dye (i.e conversion to H_2O, CO_2, NO_3-, SO_4^{2-} etc.) there

is a growing realisation that stable intermediate organic compound may form.[35] In the case of methylene blue it is also possible that under oxygen free conditions dye decolouration may involve reduction of the dye by electrons.[36]

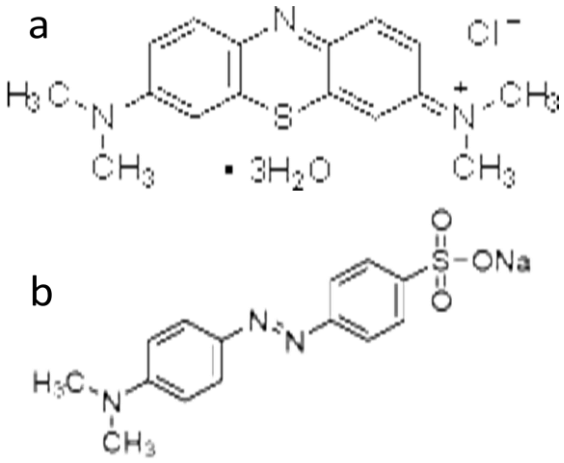


Figure 2.17. Chemical structure of (a) methylene blue and (b) methylene orange.

Kinetic studies of the decomposition of organic compounds mediated by TiO_2 under UV irradiation have established the factors that influence the rate of degradation.[37,38] Although there is not a general consensus as to the mechanism of organic dye degradation it is generally believed that dye oxidation is mediated by formation of the strongly oxidising $OH^{\cdot}$ radicals rather than by direct reaction between holes and dye molecules. Moreover it is widely agreed that the corresponding reduction of O_2 to H_2O proceeds via superoxide ions O_2^- so that the initial steps in the photocatalytic cycle are:

$$h^+ + H_2O(ads) \rightarrow H^+ + OH^{\cdot}$$

$$e^- + O_2(ads) \rightarrow O_2^-$$

The fact that dyes themselves absorb visible light has led to the suggestion that dye degradation may under some conditions be mediated by a so-called by a sensitization mechanism. This mechanism involves electron injection from a photo excited dye molecule into the photocatalyst and subsequent degradation of the resulting oxidized dye cation. This mechanism does not involve photoinduced charge separation in the photocatalyst as a result of interband excitation.[39,40] The influence of photon absorption by dyes and subsequent reaction of the excited state should be excluded when evaluating the photocatalytic activity of the solids. A way to establish that degradation of dyes is due to bandgap excitation and not due to photosensitization is to establish that there is a wavelength dependence of the photocatalytic response in the region close to the onset of the photocatalyst light absorption but not in the region where the dye absorbs light.[41]

2.10 References

(1) Wertheim, G. K. In *Solid State Chemistry. Techniques*; Cheetham, A. K., Day, P., Eds.; Oxford University Press: Oxofrd, 1988.

(2) Cardona, M.; Ley, L. In *Topics in Applied Pysics: Photoemission in Solids I*; Cardona, M., Ley, L., Eds.; Springer: Stuttgart, 1978; Vol. 26.

(3) Hüfner, S. *Photoelectron Spectroscopy: principles and aplications*; Third edition ed.; Springer: Beling, 2003.

(4) Siegbahn, K.; Nordling, C.; Fahlman, A.; Nordberg, R.; Hamrin, K.; Hedman, j.; Johansson, C.; Bergmark, S.-E.; Lindgren, I.; Lindgren, B. *In Nova Acta Regia Society of Science* **1967**, *20*.

(5) Themlin, J. M.; Chtaib, M.; Henrard, L.; Lambin, P.; Darville, J.; Gilles, J. M. *Physical Review B* **1992**, *46*, 2460.

(6) Payne, D. J.; Egdell, R. G.; Hao, W.; Foord, J. S.; Walsh, A.; Watson, G. W. *Chemical Physics Letters* **2005**, *411*, 181.

(7) Payne, D. J.; Egdell, R. G.; Law, D. S. L.; Glans, P. A.; Learmonth, T.; Smith, K. E.; Guo, J. H.; Walsh, A.; Watson, G. W. *Journal of Materials Chemistry* **2007**, *17*, 267.

(8) Manson, S. T. In *Photoemission in solids*; Cardona, M., Ley, L., Eds.; Springer: Berlin, 1978; Vol. 1.

(9) Scofield, J. H. *Journal of Electron Spectroscopy and Related Phenomena* **1976**, *8*, 129.

(10) Yeh, J. J.; Lindau, I. *Atomic Data and Nuclear Data Tables* **1985**, *32*, 1.

(11) Wagner, C. D. In *Practical surface analysis*; second ed.; Briggs, D., Seah, M. P., Eds.; Wiley; Vol. 1.

(12) Hüfner, S. *Photoelectron Spectroscopy: Principles and Applications*; 3rd ed.; Springer-Verlag: Berlin, 2003.

(13) Gelius, U.; Siegbahn, K. *Faraday Disc. Chem. Soc.* **1972**, *54*, 257.

(14) Cox, P. A. *Electronic Structure and Chemistry of Solids*; Oxford University Press: Oxford, 1987.

(15) Fox, M. *Optical properties of solids*; Oxford University press: Oxford, 2008.

(16) Kubelka, P.; Munk, F. *Zeitschrift für technische Physik* **1931**, *12*, 593.

(17) Kubelka, P. *Journal of the Optical Society of America* **1948**, *38*, 448.

(18) Yang, L.; Kruse, B. *Journal of the Optical Society of America a-Optics Image Science and Vision* **2004**, *21*, 1933.

(19) Atkins, P. W. *Quanta. A handbook of concepts*; Oxford University Press: Oxford, 1974.

(20) Wertz, J. E.; Bolton, J. R. *Electron Spin Resonance: elementary theory and practical applications*; Chapman and Hall: New York, 1986.

(21) Kneubuhl, F. K. *Journal of Chemical Physics* **1960**, *33*, 1074.

(22) Digital Instruments, Veeco Metrology Group. *Scanning Probe Microscopy. Training Notebook*: Santa Barbara, 2000.

(23) Asahi, R.; Taga, Y.; Mannstadt, W.; Freeman, A. J. *Physical Review B* **2000**, *61*, 7459.

(24) Visser, J. W. *Journal of Applied Crystallography* **1969**, *2*, 89.

(25) Cheetham, A. K. In *Solid State Chemistry. Techniques*; Cheetham, A. K., Day, P., Eds.; Oxford University Press: Oxofrd, 1988.

(26) Satterfield, C. N. *Heterogeneous catalysis in practice*; McGraw-Hill: Boston, 1980.

(27) Brunauer, S.; Emmett, P. H.; Teller, E. *Journal of the American Chemical Society* **1938**, *60*, 309.

(28) Mills, A.; Wang, J. S. *Journal of Photochemistry and Photobiology a-Chemistry* **1999**, *127*, 123.

(29) Asahi, R.; Morikawa, T.; Ohwaki, T.; Aoki, K.; Taga, Y. *Science* **2001**, *293*, 269.

(30) Sathish, M.; Viswanathan, B.; Viswanath, R. P.; Gopinath, C. S. *Chemistry of Materials* **2005**, *17*, 6349.

(31) Livraghi, S.; Paganini, M. C.; Giamello, E.; Selloni, A.; Di Valentin, C.; Pacchioni, G. *Journal of the American Chemical Society* **2006**, *128*, 15666.

(32) Yang, W. D.; Lin, W. C.; Yang, C. H.; Chung, Z. J.; Huang, I. L. *Journal of Materials Research* **2009**, *24*, 2574.

(33) Livraghi, S.; Chierotti, M. R.; Giamello, E.; Magnacca, G.; Paganini, M. C.; Cappelletti, G.; Bianchi, C. L. *Journal of Physical Chemistry C* **2008**, *112*, 17244.

(34) Dvininov, E.; Joshi, U. A.; Darwent, J. R.; Claridge, J. B.; Xu, Z. L.; Rosseinsky, M. J. *Chemical Communications*, *47*, 881.

(35) Clark, J. H.; Dyer, M. S.; Palgrave, R. G.; Ireland, C. P.; Darwent, J. R.; Claridge, J. B.; Rosseinsky, M. J. *Journal of the American Chemical Society*, *133*, 1016.

(36) Kang, X. W.; Chen, S. W. *Journal of Materials Science* **2010**, *45*, 2696.

(37) Sivalingam, G.; Nagaveni, K.; Hegde, M. S.; Madras, G. *Applied Catalysis B-Environmental* **2003**, *45*, 23.

(38) Xu, N. P.; Shi, Z. F.; Fan, Y. Q.; Dong, J. H.; Shi, J.; Hu, M. Z. C. *Industrial & Engineering Chemistry Research* **1999**, *38*, 373.

(39) Vinodgopal, K.; Wynkoop, D. E.; Kamat, P. V. *Environmental Science & Technology* **1996**, *30*, 1660.

(40) Nasr, C.; Vinodgopal, K.; Fisher, L.; Hotchandani, S.; Chattopadhyay, A. K.; Kamat, P. V. *Journal of Physical Chemistry* **1996**, *100*, 8436.

(41) Yan, X. L.; Ohno, T.; Nishijima, K.; Abe, R.; Ohtani, B. *Chemical Physics Letters* **2006**, *429*, 606.

Chapter 3 Experimental Apparatus and Techniques

This chapter describes the apparatus and techniques used to generate the data presented in subsequent chapters. The details of sample preparation are however specific to each of the systems that were studied and are included in each of the "results" chapters 4-8 rather than in this chapter.

3.1 High resolution X-ray photoelectron spectroscopy

3.1.1 Introduction

High resolution X-ray photoelectron spectra were measured in a Scienta ESCA 300 located in the National Centre for Electron Spectroscopy and Surface Analysis (NCESS) at Daresbury Laboratory.

The spectrometer is housed in an ultra-high vacuum (UHV) system incorporating an analysis chamber, a preparation chamber and a fast entry lock. The analysis and preparation chambers are pumped by separate oil diffusion pumps connected to their respective chambers through liquid nitrogen cooled traps, whilst the entry lock is pumped by a turbomolecular pump. Monochromatic X-rays are obtained from a rotating anode X-ray source and a 7-crystal monochromator. The X-ray beam enters the analysis chamber through an aluminium window and photoelectrons emitted from the sample pass through a retarding lens system and hemispherical analyzer onto a channel plate electron detection system. A schematic diagram of the spectrometer is shown in figure 3.1.

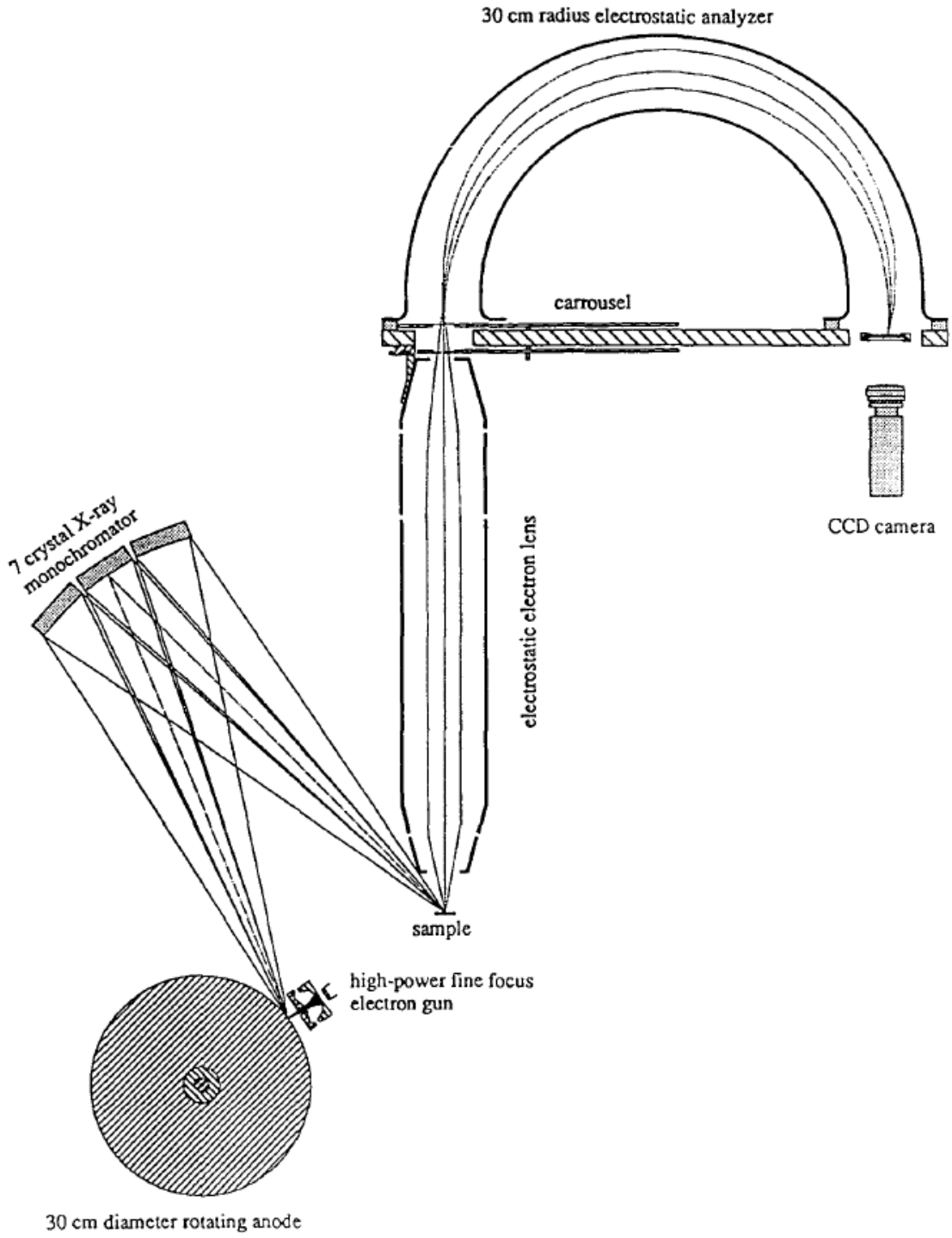


Figure 3.1. Outline of the Scienta ESCA300 spectrometer.[1]

3.1.2 X-ray source: rotating anode and 7-crystal monochromator.

The rotating anode source is a 300 mm diameter water-cooled titanium disc, which spins at about 1000 rpm. A two stage fine-focus gun produces an electron beam that is directed onto an aluminium band on the border of the disc anode under an acceleration voltage of 14 KV. The emission current can be set as high as 200 mA.

The X-rays pass into the monochromator chamber through a thin beryllium window that prevents secondary high energy electrons from bombarding the crystals of the monochromator. The wide-angle monochromator consists of seven toroidally bent α-quartz ($10\bar{1}0$) crystals, each 76 cm in diameter. These are arranged in a Rowland circle of 650 mm diameter and area of 319 mm^2.[1] The inherent resolution resulting from the finite number of atomic planes involved in the Bragg diffraction combined with the total aberration effects due to the geometry of the monochromator, give a total spread of the monochromated Al Kα radiation of about 0.26 eV.[2]

After monochromatization the X-rays pass through a thin Al foil between the monochromator and the analysis chamber. The X-rays from the the monochromator are focused at the sample position into a line ~0.5 mm wide by 6 mm long.[1]

3.1.3 Analysis chamber

The analysis chamber has a base pressure of 1×10^{-9} mbar. Samples are mounted on an XYZΘ high precision manipulator, with a geometry such that the sample, X-ray beam, and lens axis lie in a plane with the X-ray beam at 45° to the lens axis. The analysis chamber is also equipped with a VSW electron flood gun which can deliver electrons at

energies up to 10 eV. This enables stabilization of surface charge on insulating samples.

Samples are introduced into the system through a turbomolecular pumped fast entry airlock that has a based pressure of 1×10^{-6} mbar. Samples are transferred to the preparation chamber using wobble sticks and a rack and pinion railway. The preparation chamber has a base pressure below 10^{-8} mbar and is equipped with a rear-face electron beam heater and argon ion gun which allow in situ sample cleaning.

3.1.4 ESCA 300 hemispherical analyser and channel plate detection system.

Photoelectrons from the sample are collected by a multi-element lens and focused to a slit/aperture arrangement at the entrance plane of the hemispherical electron energy analyser. The slit is arranged parallel to the x-ray line on the sample. The lens may be operated in two modes giving either high transmission or high spatial resolution.[1] All spectra reported in this thesis were measured in the high electron transmission mode. The lens system retards the photoelectrons to a fixed "pass energy" energy before they enter the analyser.

The hemispherical electron energy analyser (HMA) has a 300 mm mean radius with gap of 100 mm between the hemispheres. The multichannel detector consists of a chevron assembly of two 40 mm diameter microchannel plates, a phosphor screen and a CCD TV camera.

3.2 UV/visible diffuse reflectance spectroscopy

Diffuse reflectance spectra were measured in a Perkin-Elmer Lambda 750S instrument incorporating a 60 mm integrating sphere. The spectrometer operates in a wavelength

range from 200 nm to 2500 nm with a wavelength resolution between 0.17 nm and 5.00 nm in the UV/visible region, and 0.20 nm to 20.00 nm in the near infrared.

UV-visible radiation from deuterium and tungsten halogen light sources passes through two double holographic grating monochromators, which minimize the presence of stray light.[3]

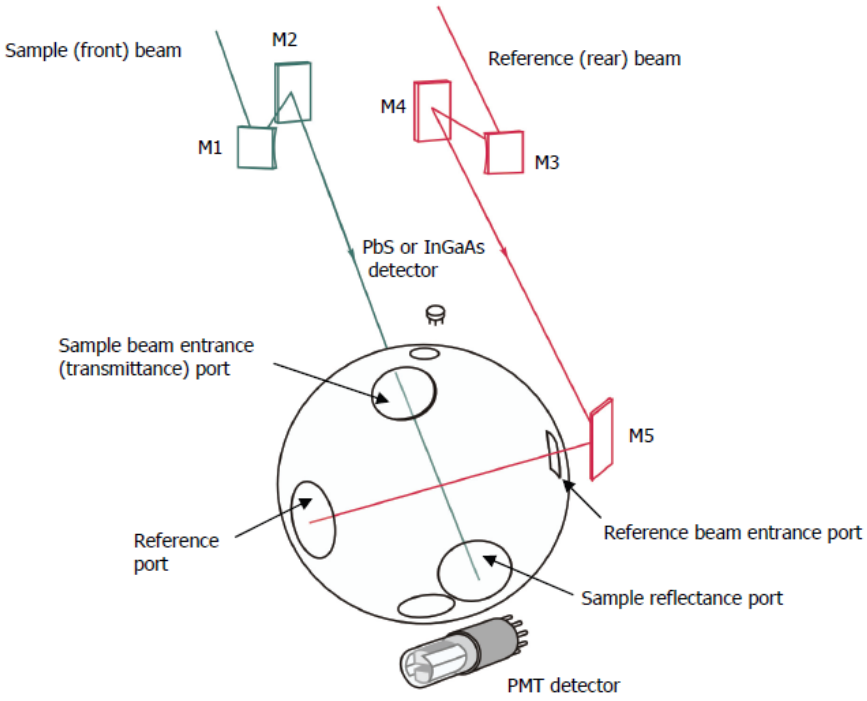


Figure 3.2. Optical beam paths inside the 60mm integrating sphere accessory.[4]

The optical arrangement is illustrated in figure 3.2. The monochromated beam is alternately directed by an arrangement of mirrors and a chopper onto one of two entrance ports on the integrating sphere: the reference beam entrance port and the sample beam entrance port. Mirrors labelled M1and M2 guide the sample beam through the sample beam entrance onto the sample reflectance port at 0° angle of incidence. Mirrors M3, M4 and M5 direct the reference beam through the rectangular reference beam entrance port onto the reference port.[4] Spectra of powders studied in

this thesis were recorded on pellets of catalyst pressed onto 13 mm diameter KBr supports. A block of Teflon with a rough surface was used as the reflectivity reference.

3.3 Electron spin resonance spectroscopy

X-band CW EPR experiments were performed on a Bruker BioSpin GmbH EMX spectrometer equipped with a high sensitivity Bruker probehead and a low-temperature Oxford Instruments CF935 helium-flow cryostat. The magnetic field was calibrated at room temperature with an external 2,2-diphenyl-1-picrylhydrazyl standard (g = 2.0036). Experiments were conducted, with ~9.4 mW microwave power, and with a 0.5 G field modulation amplitude at a modulation frequency of 100 kHz.

3.4 Raman spectroscopy

Raman spectra were measured in a Perkin-Elmer RamanStation 400F spectrometer with excitation by a He/Ne laser (785 nm) that delivers up to 100 mW radiative power at the sample in a 100μm spot size. The scattered radiation is detected by a high sensitivity charge coupled device (CCD) detector incorporating a 1024 × 256 pixel sensor hermitically sealed in vacuum. The detector is air-cooled to the operation temperature of -50 ºC. The equipment offers a pixel-limited resolution of 1 cm^{-1} in the spectral range from 95cm^{-1} to 3500cm^{-1}. The samples were mounted on a microscope slide. The stage also accommodates a USB CCD camera for the sample alignment.[5]

3.5 Atomic force microscopy

The AFM images were recorded with a Digital Instruments Multimode SPM instrument. This was operated in contact mode with a ‘J’ scanner having a lateral range

of approximately 100 μm and a vertical range of 6 μm. Silicon nitride probes (Nascatec GmbH model NST NCHFR), with a thin coating of gold to act as a mirror for the laser beam, were used. The microscope is calibrated by scanning a 10 mm pitch 200 nm 3D reference from Digital Instruments. Digital Nanoscope software (version 5.12) was used to analyse and process the AFM topographic images. All the images were treated with the 'flatten' command and are presented using one of the standard colour palettes of the Nanoscope software.

3.6 Powder X-ray diffraction

Powder X-ray diffraction patterns were measured using a PANanalytical X'pert PRO powder diffractometer. This uses a monochromatic Cu $K\alpha_1$ X-ray source and a X'Celerator detector placed in a standard Bragg-Brentano (θ-2θ) geometry. The voltage on the anode was fixed at 40 KV and the emission current was set to 45 mA. X-rays were monochromated using a curved Ge (111) crystal. The slit which defines the incident beam was programmed so that X-rays irradiated the whole sample throughout the scan, but the slit for the diffracted X-rays was kept fixed at 0.25 mm. The scan step size was set at all experiments at 0.0042° and a counting time at 0.162 s was used at each step in a scan. Measurements were made on a spinner stage which rotated the sample at 1 rev/s.

3.7 Transmission electron microscopy

Cross-sectional TEM images were collected using a JEOL3000F microscope operating at 300 KeV. Digital Micrograph image software was used to process the TEM images. Bragg filtering was applied to the TEM images in order to remove some of the

background noise and contrast adjustment was applied uniformly across the images where necessary to enhance the display quality. Specimens for cross-sectional TEM were prepared by cutting and mechanical grinding down to 5–10 μm, followed by thinning to electron transparency by Ar ion beam milling using a Gatan 691 Precision Ion Polishing System (PIPS).

3.8 Surface area determination by physisorption analysis

Specific surface area, pore volume and pore size distributions of the samples were determined from the adsorption–desorption isotherms of nitrogen at 77 K using a ThermoQuest Sorptomatic 1990 series adsorption apparatus. Prior to analysis, the samples were degassed at 150 °C for 10 h under vacuum. The specific surface area of the samples was calculated by the BET method based on the N_2 adsorption isotherm data in the P/P_0 range from 0.1 to 0.3. The pore volume was calculated from the amount of N_2 adsorbed at a relative pressure of 0.95.

3.9 Photocatalytic model tests

The photocatalytic activity was evaluated by monitoring the photo-decolourisation of an aerated aqueous solution of methylene blue[6] with a concentration of 10 ppm. This simple method of assessing photoactivity has proved a very popular and convenient method for screening catalysts[7-11]. A 150 W Xe lamp was used as the radiation source. The short wavelength components of the lamp output were removed using optical filters with cutoffs at $\lambda < 395$ nm ($h\nu > 3.14$ eV), $\lambda < 400$ nm ($h\nu > 3.10$ eV) and $\lambda <$ 420nm ($h\nu > 2.95$ eV). In a typical photocatalytic experiment, a total of 40 mg of catalyst powder was added to 40 cm^3 of the methylene blue solution in a borosilicate

tube. Prior to irradiation, the suspensions were magnetically stirred in the dark for 60 minutes to ensure the establishment of equilibrium coverage of the catalyst powder by the dye. At measured time intervals, aliquots of around 3 cm^3 were extracted and filtered through a 0.20 μm membrane filter to remove the catalyst particles. The filtrates were analyzed by recording variations in the absorbance at 665 nm (the peak maximum in the absorption spectra) in a Libra S6 Visible Spectrophotometer relative to the initial reading. The percentage of methylene blue degradation was plotted against the time of irradiation to provide a quantitative indication of the activity of the catalyst. Dye degradation tests were also carried out using a similar procedure but with a 10 ppm solution of methyl orange[12,13]. The concentration of this dye was monitored using the absorption peak at 480 nm. This dye underwent photodecomposition at a lower rate than methylene blue and experiments were conducted using the output of a 300 W solar simulator lamp with a 400 nm cutoff filter.

3.10 References

(1) Beamson, G.; Briggs, D.; Davies, S. F.; Fletcher, I. W.; Clark, D. T.; Howard, J.; Gelius, U.; Wannberg, B.; Balzer, P. *Surface and Interface Analysis* **1990**, *15*, 541.

(2) Payne, D. J. *The electronic structure of post-transition metal oxide*. D. Phil Thesis, University of Oxford, 2008.

(3) PerkinElmer *the new LAMBDA™ 750 UV/Vis/NIR spectrophotometer from PerkinElmer*, 2007.

(4) PerkinElmer *Sphere accessories user's guide*, 2007.

(5) PerkinElmer *RamanStation 400 series. Getting started guide*, 2007.

(6) Mills, A.; Wang, J. S. *Journal of Photochemistry and Photobiology a-Chemistry* **1999**, *127*, 123.

(7) Asahi, R.; Morikawa, T.; Ohwaki, T.; Aoki, K.; Taga, Y. *Science* **2001**, *293*, 269.

(8) Sathish, M.; Viswanathan, B.; Viswanath, R. P.; Gopinath, C. S. *Chemistry of Materials* **2005**, *17*, 6349.

(9) Livraghi, S.; Paganini, M. C.; Giamello, E.; Selloni, A.; Di Valentin, C.; Pacchioni, G. *Journal of the American Chemical Society* **2006**, *128*, 15666.

(10) Yang, W. D.; Lin, W. C.; Yang, C. H.; Chung, Z. J.; Huang, I. L. *Journal of Materials Research* **2009**, *24*, 2574.

(11) Livraghi, S.; Chierotti, M. R.; Giamello, E.; Magnacca, G.; Paganini, M. C.; Cappelletti, G.; Bianchi, C. L. *Journal of Physical Chemistry C* **2008**, *112*, 17244.

(12) Brown, G. T.; Darwent, J. R. *Journal of Physical Chemistry* **1984**, *88*, 4955.

(13) Song, X. M.; Wu, J. M.; Yan, M. *Thin Solid Films* **2009**, *517*, 4341.

Chapter 4 Evaluation of the mode of incorporation of nitrogen in doped anatase photocatalysts.

4.1 Introduction.

Following the observation of Asahi et al.[1] that N doping in TiO_2 leads to enhanced visible region photoactivity, there have been around 1000 studies of this and related anion doped systems. Asahi et al. achieved nitrogen doping by sputtering a TiO_2 target in an Ar/N_2 gas mixture. Nitrogen doping may also be accomplished by N ion bombardment,[2,3] by MBE growth or chemical vapour deposition using a plasma containing a nitrogen source,[4-7] or by post-treatment of TiO_2 thin films, crystals or powders with NH_3 at elevated temperature.[8-13] Alternatively a very large number of papers have described preparation of N-doped photocatalysts using wet chemical methods involving nitrogen containing precursors.[13-29] Although these different procedures can all lead to N doped material showing visible region photocatalytic activity, there is still no consensus as to the optimal mode of incorporation of N in doped TiO_2 and there is an ongoing debate about the nitrogen species responsible for visible region photoactivity.[6,13-15,25] However there is a growing belief that the "correct" mode of incorporation of nitrogen is critical to optimal catalytic performance.[6]

Two main techniques have been used to investigate the incorporation of nitrogen in TiO_2, but neither is able to provide information on the *total bulk* nitrogen doping level and in almost all experimental studies to date the concentration of bulk nitrogen has not been determined. The more popular of the two techniques is X-ray photoemission

spectroscopy (XPS). The intensity of the photoemission feature associated with the N 1s core level provides a means of determining the absolute surface nitrogen doping level within the sampling range of XPS. In addition the binding energies of the N 1s core electrons give insight into the chemical state of the N dopant.[4-9,14,15,17,22,23,25] N 1s structure in XPS observed with binding energies around 396-398 eV is usually ascribed to "substitutional nitrogen". This assignment is based in part on N 1s binding energies for simple nitrides such as CrN (396.8 eV) and Si_3N_4 (397.7 eV) given in standard tabulations.[30] There is however no universal agreement as to the charge state of the substitutional nitrogen species in TiO_2. Thus in many papers N-doped TiO_2 is loosely described as $TiO_{2-x}N_x$,[7,9,13,15-17,21,25,26] which implies that N^{2-} replaces O^{2-} in a substitutional site. A consequence of such a formulation is that there must be holes in the O 2p / N 2p valence band of the doped material and the Fermi level will be found at the top of the valence band rather than at the bottom of the conduction band as in nominally undoped TiO_2, where oxygen vacancy defect states pin the Fermi level close to the bottom of the conduction band, as described in section 1.2. N 1s structure at higher binding energies around 400 ± 1 eV is ascribed in a number of papers to "interstitial nitrogen". Density functional calculations carried out by Pacchioni and co-workers suggests that interstitial N will in fact bind to lattice O^{2-} to give a species in which an NO-like unit is bonded sideways to three Ti atoms[14,20,24,31]. However, a number of authors describe interstitial nitrogen as "Ti-N-O"[6] or "Ti-O-N"[19,21,25], but without defining the specific geometrical arrangement of the atoms. Alternatively the higher binding energy structure has been taken to be diagnostic of adsorbed or interstitial NH_3 or other species containing N-H bonds[9,32]. As described in chapter 2, XPS is a surface sensitive technique due the relatively small inelastic mean free path lengths λ of low energy electrons in solids. The surface sensitivity of XPS coupled

with the observation that the nitrogen detected in XPS appears to be quite labile has led to the suggestion that the species observed by this technique are purely confined to the near surface region and are not therefore connected with bulk photoabsorption or photocatalysis.[14] The second technique widely applied for the study N in TiO_2 is electron paramagnetic resonance spectroscopy (EPR).[14,18,20,24,26,31,33-38] EPR probes both surface and bulk species. However the technique is "blind" to N dopant centres which are not paramagnetic.

In the present chapter XPS and EPR analysis of N doping in TiO_2 is combined with the determination of the overall bulk doping level by conventional bulk chemical analysis of N using an inert gas fusion technique. It emerges that bulk and surface doping levels are in most cases quite close to each other but that the paramagnetic species observed by EPR have concentrations around 3 orders of magnitude lower than the bulk doping level. Based on the experimental observations a mechanism for incorporation of interstitial nitrogen into TiO_2 is suggested using balanced Kröger-Vink equations which define the formal charge states of the species involved.

4.2 Experimental section

4.2.1 Preparation of the solids

A sol-gel method based on literature was used to prepare the N-doped TiO_2 samples. Common procedures previously reported involve the precipitation from solutions of titanium isopropoxide in alcohol by hydrolysis with aqueous solution of source of nitrogen (such as NH_3 or NH^{4+} salts) followed by thermal sintering.[20,34,39,40] In preliminary work, a range of sintering temperatures between 350°C and 450°C was

explored. The minimum temperature needed to bring about adequate crystallisation in the anatase phase during a one hour anneal was 380 °C. Sintering at higher temperatures led to a marked reduction in sample surface area and catalytic activity. Thus all subsequent sintering was carried out at 380 °C for 1 hour. Sample A was prepared as follows. 20 cm^3 of the ammonia solution (ammonium hydroxide, 25% Aldrich Chemicals Co) was added drop-wise into 60 cm^3 of a solution of titanium isopropoxide ($Ti[OCH(CH_3)_2]_4$, 97% Aldrich Chemicals Co.) in anhydrous isopropanol (15:85 volume ratio) previously acidified using HNO_3 (HNO_3/Ti molar ratio 0.15). The suspension formed was continuously stirred for 60 minutes and then dried at 80°C, followed by calcination at 380°C for one hour. Sample B was prepared using the same conditions but with a longer period of stirring (180 minutes). A third sample labelled C was prepared by adding stoichiometric amount of distilled water into the $Ti[OCH(CH_3)_2]_4$ solution prior the treatment with ammonia solution and subsequent steps as above, with 60 minutes stirring as in A. The fourth sample labelled as D was prepared from $Ti[OCH(CH_3)_2]_4$ solution in ethanol (15:85 volume ratio) which was saturated with ammonia gas at 5°C and hydrolyzed with dilute HNO_3 (so that HNO_3/Ti ratio=0.15). After adding the acid solution the suspension generated was treated as above with 60 minutes stirring followed by drying at 80°C and calcination at 380°C. To provide a reference material, undoped TiO_2 was prepared under the same conditions as sample A but hydrolysis was carried out using distilled water without addition of NH_3. This sample is labelled as U. After calcination, all N-doped samples showed the pale yellow colour characteristic of N-doped TiO_2.

4.2.2 Characterization

The bulk N doping level was determined by an inert gas fusion method carried out by

LSM Analytical Services (Rotherham, UK) using a LECO TC436 analyser. This laboratory holds UKAS accreditation under International Standard ISO/IEC 17025:2005. Around 1 g of a powder sample was placed into a graphite crucible and fused with an excess of a high purity Ni flux at 3000 °C (3273 K) under flowing high purity He gas. Under the highly reducing conditions of the graphite lined furnace, the oxides of nitrogen NO, N_2O and NO_2 are all thermodynamically unstable with respect to formation of CO and N_2. Although NH_3 has a negative standard enthalpy of formation ($\Delta H_f^0(NH_3) = -45.94$ kJ mol^{-1}) there is a very large entropic driving force toward decomposition and the free energy of decomposition of $2NH_3$ into N_2 and $3H_2$ at 3000°C is around -550 kJ mol^{-1} (of N_2). Thus *all* the nitrogen present in the samples should be released as N_2. The CO and any H_2 (which could derive from moisture, ammonia or hydrocarbon contamination) also evolved were oxidised to CO_2 and H_2O respectively by passage over a rare earth doped copper oxide catalyst and were trapped out using a proprietary Lecosorb/anhydrone trap. The remaining N_2 in the carrier gas was then quantified by measurement of the thermal conductivity.

X-ray diffraction (XRD) patterns of all samples were collected in the range $20° < 2\theta < 70°$ using a Phillips X'Pert diffractometer with a monochromated Cu $K\alpha_1$ X-ray source, operated at 40 kV and 40 mA. Specific surface area, pore volume and pore size distributions of the samples were determined from the adsorption/desorption isotherms of nitrogen at 77 K using a ThermoQuest Sorptomatic 1990 series adsorption apparatus. Prior to analysis, the samples were degassed at 150 °C for 10 hours under vacuum. The specific surface area of the samples was calculated by the BET method based on the N_2 adsorption isotherm data. The pore volume was calculated from the amount of N_2 adsorbed at a relative pressure of 0.95. The pore radius distribution was estimated by

applying the Dollimore–Heal method to the measured desorption isotherm.

UV/visible diffuse reflectance spectra were measured on pellets of catalyst pressed onto 13 mm diameter KBr supports in a Perkin Elmer Lamda 750S spectrometer incorporating a 60 mm integrating sphere. High resolution X-ray photoemission spectra (XPS) were recorded in a Scienta ESCA 300 spectrometer located at Daresbury Laboratory, UK, which incorporated a rotating anode Al Kα (hυ =1486.6 eV) X-ray source. The X-ray source was run with 200 mA emission current and 14 kV anode bias, while the analyzer operated at 150 eV pass energy with 0.8 mm slits. Gaussian convolution of the analyzer resolution with a linewidth of 260 meV for the monochromated x-ray source gives an effective instrument resolution of 400 meV. Electron paramagnetic resonance (EPR) spectra were collected at 298 K using a Bruker X-band CW spectrometer operating at 9.44 GHz. A modulation frequency of 100.0 KHz and an external frequency counter were employed. A crystal of 2,2-diphenyl-1-picrylhydrazyl (DPPH) was used to calibrate the spectrometer, assuming a g value of 2.0036.

4.2.3 Catalytic activity

The photocatalytic activity was evaluated by monitoring the photo decomposition of an aqueous solution of methylene blue with a concentration of 10 ppm. This simple method of assessing photocatalytic activity was first employed by Asahi et al.[1] and has remained a popular method for screening catalysts[22,24,27,33] despite the possibility of direct photolytic degradation of the dye. To take account of this possibility the activity of the N doped catalysts was always compared with that of the undoped TiO_2 sample U. A 150 W Xe lamp was used as the radiation source. The short wavelength components

of the lamp output were removed using optical filters with cutoffs at $\lambda < 395$ nm ($h\nu > 3.14$ eV), $\lambda < 400$ nm ($h\nu > 3.10$ eV) and $\lambda < 420$ nm ($h\nu > 2.95$ eV). In a typical photocatalytic experiment, a total of 40 mg of catalyst powder was added to 40 cm^3 of the methylene blue solution in a borosilicate tube. Prior to irradiation, the suspensions were magnetically stirred in the dark for 60 minutes to ensure the establishment of equilibrium coverage of the catalyst powder by the dye. At measured time intervals, aliquots of around 3 cm^3 were extracted and filtered through a 0.20 μm membrane filter to remove the catalyst particles. The filtrates were analyzed by recording variations in the absorbance at 665 nm (the peak maximum in the absorption spectra) in a Libra S6 Visible Spectrophotometer relative to the initial reading. The percentage of methylene blue degradation was plotted against the time of irradiation to provide a quantitative indication of the activity of the catalyst.

4.3 Results and discussion.

4.3.1 Crystallinity, particle size and surface area

As prepared catalyst powders appeared to be amorphous in X-ray diffraction and exhibited minimal enhanced catalytic activity as compared to undoped samples. Annealing at temperatures above 350 °C was necessary to induce formation of crystalline photoactive catalysts. Figure 4.1a shows diffraction patterns of a precursor sample calcined at a range of different temperatures, mostly for 1 hour. It can be seen that there is no evidence for emergence of crystalline phases after annealing at 350 °C and that the diffraction peaks associated with the anatase phase remain weak after annealing at 360 °C and 370 °C for 1 hour. Annealing at 380 °C leads to improved crystallinity. Although material with a similar x-ray signature could be prepared by

annealing at 370 °C for 3 hours, but this longer time of calcination brings about an increase in the particle size, which reduces the surface area of the solid. Calcination at higher temperatures up to 450°C does not produce any major change in the XRD patterns but does lead to a progressive decrease in surface area (see table 4.1) and a reduction in catalytic activity. Figure 4.1b shows x-ray diffraction patterns of the N-doped samples studied in the present work, all of which were sintered at 380 °C for 1 hour. Diffraction peaks can all be assigned to the anatase phase of TiO_2. There is no significant change in peak position compared with the undoped material.

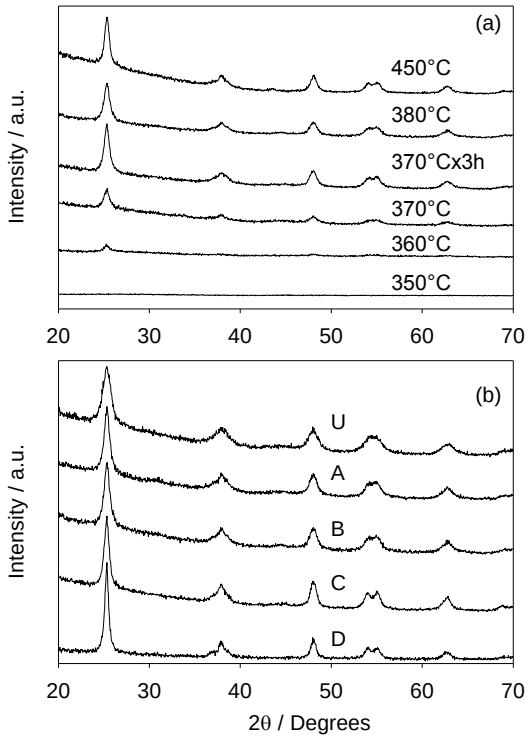


Figure 4.1 (a) X-ray powder diffraction patterns for an anatase precursor powder sintered at the range of temperatures indicated. Unless specified otherwise the sintering time was 1 hour in each case. (b) X-ray powder diffraction patterns for the four N-doped catalyst powders studied in the present work along with the powder pattern for the undoped reference sample U.

Table 4.1 BET surface areas as function of calcination temperature for samples prepared by synthetic route A

Calcination temperature (°C)	BET surface area (m^2 / g)
350	206
370	189
380	164
400	127
450	115

From the measured width of the anatase (1 0 1) peak crystallite sizes were estimated by means of the Scherrer equation (eq 1) .

$$D = \frac{k\lambda}{\beta \cos\theta} \quad \text{(eq. 1)}$$

Here D is the average crystallite size in Ångstroms; *k* is a constant which is taken as 0.89; λ is the wavelength of the X-ray radiation (CuKα, λ = 1.5406 Å); θ is the Bragg angle of the diffraction peak; and β is the corrected broadening, obtained after quadratic subtraction of instrument broadening, using the (110) peak of a well-sintered sample of rutile TiO_2 (particle size > 2 μm) as the standard. The results of this analysis are shown in table 2, which also gives BET surface areas and pore volumes estimated from nitrogen adsorption at $P/P_0 = 0.95$.

It can be seen that the crystallite sizes of the samples are in a range between 100 Å to 200 Å. The crystallite size is bigger for all the N-doped samples than for the undoped anatase reference sample U and is highest for the sample D, where ammonia was introduced by bubbling gas through the solution of titanium isopropoxide. In general there is a good inverse correlation between the crystallite size from XRD line broadening and the BET surface area for the N doped samples. The lowest surface area

was found for sample D, which also exhibited the smallest pore volume.

Table 4.2 Some morphological properties of the prepared solids.

Catalyst	Crystallite size[a] (Å)	S_{BET}[b] (m^2/g)	Pore volume[c] (cm^3/g)
U	95	167	0.18
A	128	164	0.24
B	131	167	0.20
C	166	142	0.22
D	191	130	0.12

[a] Calculated by applying the Scherrer formula for line broadening to the anatase (101) diffraction peak.
[b] BET surface area calculated from the linear part of the BET plot (P/P_0 = 0.1–0.3).
[c] Total pore volume, taken from the volume of N_2 adsorbed at P/P_0 = 0.95.

4.3.2 Bulk and surface N doping levels.

The bulk N doping levels determined by the inert gas fusion method are given in table 4.3. In all cases the doping levels are around 10^{22} N atoms/mol, corresponding to a N/Ti ratio of about 0.015 i.e. the N doping level is about 1.5 %. The doping level defined in this way was highest for sample C where the value is 2.5% and lowest for sample B where the value is 0.8 %. In order to assess the reproducibility of the bulk analytical technique, a series of four nominally identical samples from a large batch synthesis giving the lowest N doping level were analysed. The standard deviation was found to be 4% of the mean.

Table 4.3 Comparison of bulk N concentrations from inert gas fusion analysis, surface N concentration from XPS and paramagnetic N concentration from EPR in N-doped TiO_2 catalysts.

Catalyst	Bulk N concentration[a] (10^{22} atoms mol^{-1})	Total surface N concentration[b] (10^{22} atoms mol^{-1})	Bulk paramagnetic N-concentration[c] (10^{18} spin mol^{-1})
A	1.3 ± 0.1	1.3 ± 0.1	3.2 ± 0.6
B	0.50 ± 0.05	1.1 ± 0.1	2.5 ± 0.5
C	1.5 ± 0.1	1.4 ± 0.1	1.2 ± 0.4
D	1.3 ± 0.1	0.75 ± 0.1	2.5 ± 0.5

[a] determined by inert gas fusion analysis
[b] determined by XPS
[c] estimated from EPR using freshly prepared DPPH solutions in toluene as a standard

The surface N concentrations as determined by XPS are also given in table 3. These values were derived by correcting the measured Ti 2p and N 1s total peak areas by the relevant atomic sensitivity factors[30]. The uncertainty in XPS quantification is around ±10%. The surface doping levels were found to be very close to the bulk doping levels for both samples A and C. Somewhat surprisingly the surface doping level was found to be lower than the bulk doping level for sample D and higher than the bulk doping level for sample B. Nonetheless the difference between bulk and surface doping levels is at most a factor of around 2. It is therefore clear that the sol gel method of sample preparation leads to significant incorporation of N throughout the bulk of the samples. Detailed discussion of the N 1s core lineshape and the N 1s chemical shift is given below.

4.3.3 The influence of N doping on electronic structure and the mode of N incorporation.

The N-doped samples calcined at 380 °C for 1 hour all exhibited a pale yellow colouration indicative of visible region absorption by the solids. The influence of doping on the electronic spectrum was studied by diffuse reflectance spectroscopy. The

Kubelka-Munk function F(R) derived from the diffuse reflectivity is taken to represent the absorption coefficient α of the sample. The spectra presented as plots F(R) against energy are shown in figure 4.2 for undoped TiO_2 (sample U) and two N-doped TiO_2 samples (A and C). The other doped samples all gave very similar spectra. For undoped TiO_2 absorption extends down to about 3.0 eV. The absorption onset is well below the 0 K bandgap of 3.42 eV[41] due to pronounced phonon assisted Urbach tailing in the room temperature spectrum. The absorption onset for the doped sample is at around 2.4 eV, corresponding to a downward shift in the absorption onset of 0.6 eV. This is consistent with the calculations of Pacchioni and co-workers which show that both substitutional and interstitial nitrogen doping introduces new occupied states in the bandgap above the top of the valence band of undoped anatase TiO2.[14,24,31]

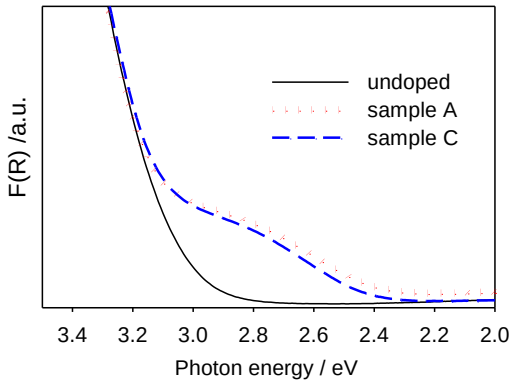


Figure 4.2 Absorption spectra (represented by the Kubelka-Monk function, F(R)) of an undoped anatase powder sample and N-doped samples A and C as obtained from diffuse reflectance spectroscopy.

Figure 4.3 shows the geometry of the two models they used for their calculations.[20] In the substitutional model (figure 4.3a), the nitrogen atom is bound to three Ti atoms and replaces a lattice oxygen in TiO_2. In the interstitial model, a N atom bound to one lattice oxygen to form a NO species (Figure 4.3b). Within various starting configurations considered, with the N atom coordinated to one or up to three lattice oxygen atoms,

they found this to present the lowest energy minimum. Although interstitial NO species trapped in the lattice and bound to a lattice oxygen atom (forming NO_2^{2-}) has been proposed on the basis of EPR measurements,[18] it was found to be unstable because of the repulsive interactions of the trapped NO with the surrounding cavity.[20]

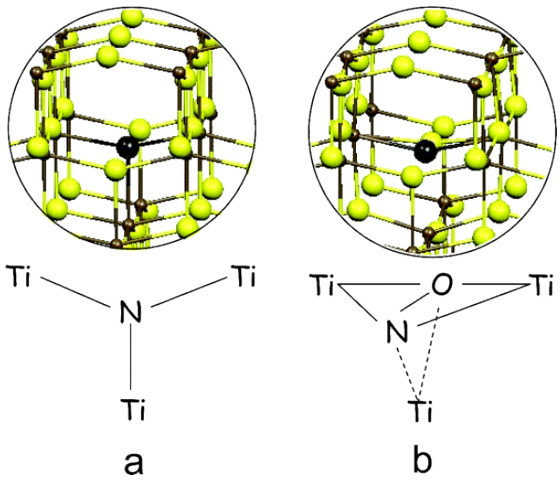


Figure 4.3. Partial geometry and schematic sketch of the model for (a) substitutional and (b) interstitial N-doping in an anatase matrix. The N atom is represented by a black sphere, O atoms are represented by yellow spheres, and Ti atoms are represented by small brown spheres.[20]

The gap states are found[14] 0.14 eV and 0.73 eV above the top of the valence band for the paramagnetic species N^{2-} and NO^{2-} respectively. The states move to higher energies within the bandgap in the corresponding diamagnetic species N^{3-} and NO^{3-} due to increased coulombic repulsion, with calculated energies of 0.59 eV and 0.75 eV respectively relative to the valence band maximum. The large shift between substitutional N^{2-} and N^{3-} is a consequence of the fact that the orbital where the extra electron is accommodated is localised on one atom[24]. By contrast the gap states for NO^{2-} and NO^{3-} are associated with an antibonding π^* orbital within the NO unit, which is triply occupied for NO^{2-} and quadruply occupied for NO^{3-}. Thus the extra electron is more delocalised than for substitutional doping. In addition the increased occupation of an antibonding orbital leads to lengthening of the NO bond which will tend to move the

π* level to lower energy. It appears that the coulombic and bondlength effects almost cancel each other so that the shift between NO^{2-} and NO^{3-} is very small. The shift in the optical onset by about 0.6 eV is consistent with incorporation of diamagnetic nitrogen in either substitutional or interstitial sites.

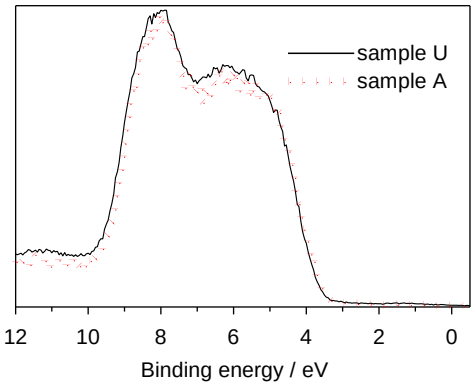


Figure 4.4 Comparison of valence band XPS for an undoped anatase sample (dotted curve) and an N-doped sample prepared by route A (solid line).

Valence band X-ray photoemission was intended to directly measure the N-induced states in the bandgap. As shown in figure 4.4 the valence band onset for undoped samples is found around 3.2 eV. Given the value of the bulk bandgap this demonstrates that the Fermi level is pinned close to the bottom of the conduction band. There is no obvious change in the position of the valence band edge for N doped samples or the appearance of new structure within the bandgap. This contrasts with a earlier work by my group on TiO_2 single crystals doped with N by treatment with NH_3 at elevated temperatures,[8] where new structure above the valence band edge is clearly observed in photoemission, extending into the bottom half of the bulk bandgap. However, the N doping level in this earlier work was around a factor of 10 higher than in the present work and the dominant mode of nitrogen incorporation was as substitutional nitrogen rather than interstitial nitrogen as found here (see below). It is important to note that the

fact that the main O 2p valence band edge in N doped samples was basically unshifted from its position for undoped samples provides compelling evidence that the Fermi level in N-doped samples remains pinned close to the bottom of the conduction band.

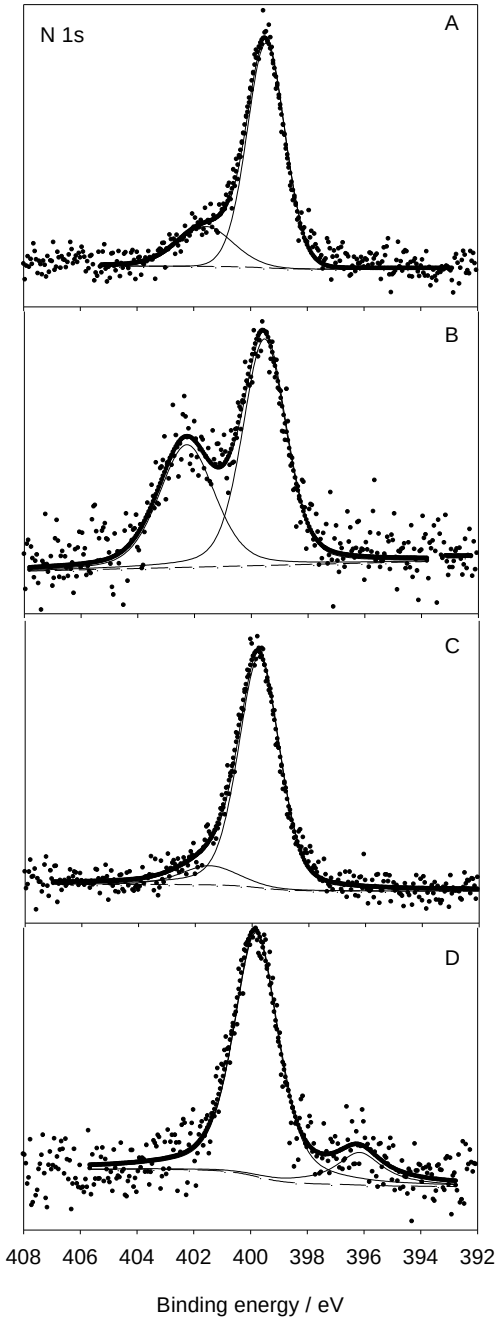


Figure 4.5 N 1s core level structure in XPS for the N-doped samples A-D studied in the present work.

In order to investigate the chemical states of the species present on the N-doped TiO_2 catalyst surfaces and their concentrations, high-resolution X-ray photoelectron spectra

of the N 1s and Ti 2p core levels were measured. Figure 4.5 shows the XPS spectra in the N 1s region of N-doped, along with curve fits to the spectra. It can be seen that for all samples there is a broad N 1s peak with a binding energy of around 399.5 eV. This is referred to as peak II in table 3. A further and much weaker peak at a higher binding energy of 401.5 eV is observed for samples A, B and C and is labelled as I. This peak is absent or very weak indeed for sample D which reveals instead a further weak peak at the lower binding energy of 396.2 eV, labelled III in the table.

Table 4.4 Surface N/Ti ratios in XPS.

Catalyst	Surface N/Ti ratio[a]			
	N Peak I 401.5 eV	N Peak II 399. 5 eV	N Peak III 396.2 eV	Total N (I+II+III)
A	0.005	0.016	-	0.022
B	0.007	0.011	-	0.018
C	0.002	0.022	-	0.024
D	-	0.011	0.002	0.013

[a]from XPS core line intensities using sensitivity factor of 1.2 for Ti $2p_{3/2}$ and 0.42 for N 1s.

As discussed above, the two main modes of nitrogen incorporation considered in the literature involve substitution of N on O sites and occupation of interstitial sites. The binding energies reported for the N 1s peak of TiN range between 396.7 eV and 397.1 eV[42,43] and it seems reasonable to assume that peak III is associated with substitutional nitrogen. If N^{2-} simply replaces O^{2-} to give paramagnetic $N_O^{\times}$ in Kroger-Vink notation, the 2p shell of the N^{2-} anion would contain a single hole and a shift in the N 1s peak to higher binding energy would be expected. However N substitution on 2*x* sites can be

compensated by the electrons from x doubly ionised oxygen vacancies $V_O^{\bullet\bullet}$ to give substitutional diamagnetic N^{3-} (i.e. N_O') and a material with overall stochiometry $TiO_{2-3x}N_{2x}$. Turning now to interstitial doping, extensive computational work has shown that N_i is stabilised by binding to a lattice O^{2-} ion to give NO^{2-}.[14,20,24] This defect complex could alternatively be described as $(NO)_O^\times$ in Kröger-Vink notation and like $N_i^\times$ itself this is a paramagnetic species: the molecular valence shell configuration is $\sigma^2\pi^4\pi^3$. Again this paramagnetic acceptor species can be rendered diamagnetic by compensation with electrons derived from oxygen vacancies to give NO^{3-} with a configuration $\sigma^2\pi^4\pi^4$: in Kröger-Vink notation this is $(NO)_O'$. The formal oxidation state of nitrogen in $(NO)_O'$ is –I and therefore a assignment of the peak at 399.5 eV to this species is reasonable. The chemical shift in N 1s binding energies between $N_O^\times$ and $(NO)_O^\times$ is calculated to be +1.6 eV.[14] This is somewhat less than the shift observed between peaks II and peak III. However the computational study did not deal with the N 1s chemical shift between diamagnetic N_O' and $(NO)_O'$ and as discussed in the context of the shift of N 2p levels in the bandgap, the shift to low energy is expected to be bigger for N_O' than for $(NO)_O'$ due to the greater electron delocalisation in the latter. Thus a chemical shift of 2.5 eV between N_O' and $(NO)_O'$ is not undreasonable. The peak observed at 401.5 eV for samples A, B and C is probably associated with NH_4^+ salt contaminant left on the sample surface: a binding energy of 401.5 eV has been reported for NH_4^+ species[44]. There is no indication of surface NO_3 species where then N 1s binding energy is expected to be around 407 eV[45].

Ti 2p core level spectra of the samples U and A-D are shown in figure 4.6. The spectra are essentially unchanged as a result of N doping aside from a barely significant shift to low binding energy, which is at most 0.2 eV (for sample C). A similar but bigger shift

has been noted by Wang *et al.* and attributed to empty states associated with Ti ions adjacent to doubly ionised oxygen vacancies.[11]

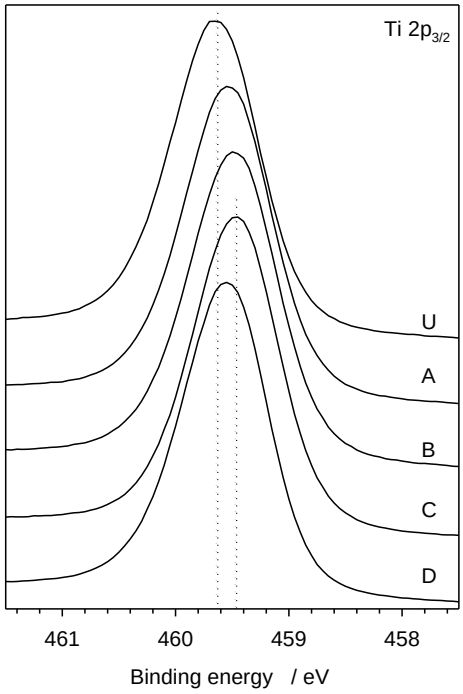


Figure 4.6 Ti 2p core level structure for the undoped anatase sample and N-doped samples prepared by routes A-D.

These observations again indicate that the position of the Fermi level in the near surface region in all samples change very little upon N doping. In previous work on rutile TiO_2(110) single crystals doped with N by treatment with NH_3 at 600 °C done by my group, broad structure on the low binding energy side of the main Ti $2p_{3/2}$ peak was observed,[8] similar to those observed by Batzill *et al.*[2] and Chambers *et al.*[4]. Chemically shifted structure of this sort is often taken to be indicative of reduction of Ti^{4+} to Ti^{3+}. However valence band photoemission showed that no reduced Ti(III) was present[8]. Also in that work the N 1s core binding energy indicated that the N was present mainly as N_O'. It has been argued that due to the lower electronegativity of N as compared with O, N^{3-} substitution on O^{2-} sites gives rise to the new Ti 2p structure centred at around

0.9 eV to low binding energy of the Ti 2p peak of TiO_2 itself[2,4,5,8]. The large width of this structure observed in experiments on rutile TiO_2(110) treated with NH_3 at 600 °C was attributed to the fact that this treatment produces a relatively high doping level and there are a range of possible coordination environments $TiO_{6-n}N_n$ with $1 \leq n \leq 6$.[8] The absence of low binding energy structure of this sort in the present work provides further evidence that that most of the N in doped samples is present as NO^{3-} and not as N^{3-} directly bound to Ti.

4.3.4 Electron paramagnetic resonance (EPR) spectra

X-band EPR spectra of the catalyst samples are shown in figure 4.7.a. These spectra are better resolved than in most previous work[18,24,26,31,33-38] although they are very similar to some of the spectra reported by Di Valentin and Livraghi and co-workers[14,20]. The spectra are characteristic of an orthorhombic system with hyperfine coupling to ^{14}N. However, the spectra cannot be simulated using a single set of orthorhombic parameters. In particular, the splitting of the feature at around 3300 gauss into two components, whose relative intensities vary somewhat between the different samples, points to the presence of two distinct paramagnetic species. Therefore spectra were simulated as a superposition of signals due to two components identified as species i and species ii. The results of these simulations are shown in the lower panels to figure 4.7.b whilst the parameters used to generate the simulated spectra are given in table 4.5. where it is seen that the g values for species i and species ii differ by about 0.0005. There are also small differences in the ^{14}N hyperfine coupling constants. The EPR signal for samples B and C are dominated by species i, whilst D is dominated by ii and A is a near equal mix of i and ii. The two component structure has been noted before[14,20] but the distinct values for the EPR parameters needed to simulate the spectra

have not been reported before.

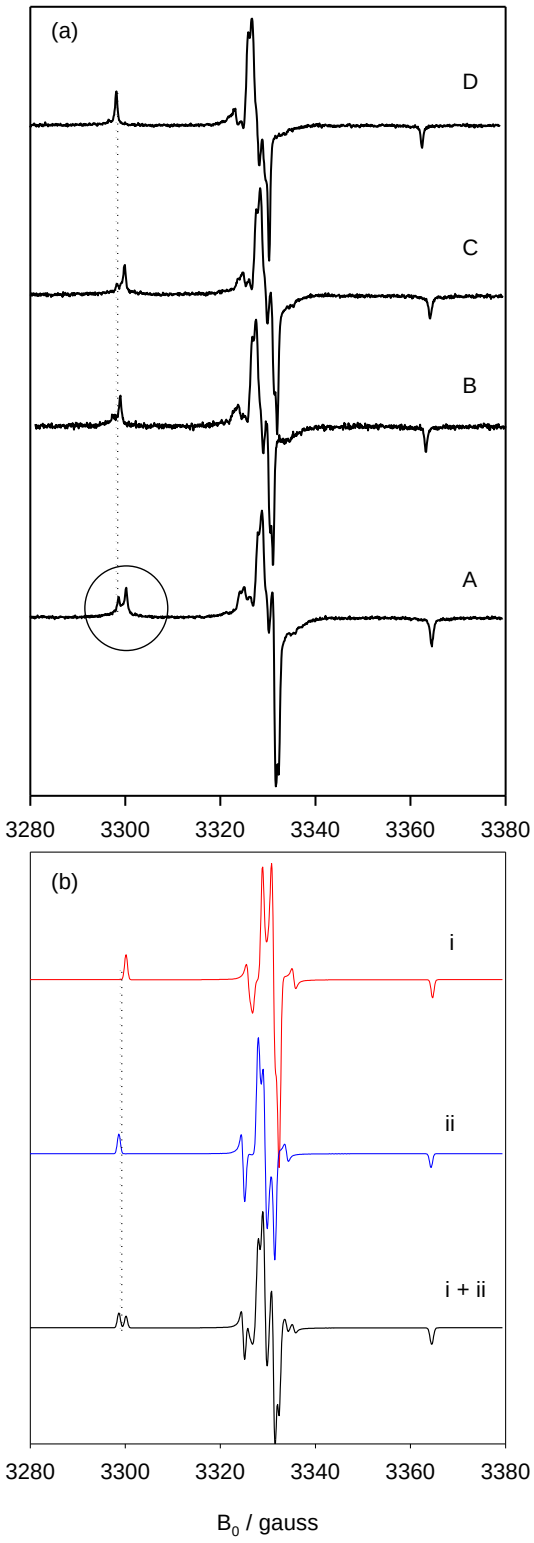


Figure 4.7 X-band EPR spectra of the four N doped samples studied in the present work. (b) Simulated EPR spectra using the two different sets of parameters listed in table 5 together with the sum of the two simulated spectra.

Table 4.5 Parameters from simulations of EPR spectra.

	g_1	g_2	g_3	A_1 (MHz)	A_2(MHz)	A_3 (MHz)
Species i	2.0058	2.0044	2.0037	8.12	12.04	90.44
Species ii	2.0063	2.0048	2.0041	7.56	12.60	92.12

The EPR spectra similar to those found in the present work have previously been associated with a species labelled as N_b where the subscript b indicates a bulk species. As discussed above N_b can be described as an interstitial N atom bound to a lattice O^{2-} species to give the paramagnetic NO^{2-} species or $(NO)_O^{\times}$ in Krőger-Vink notation. This species will have 3 electrons in the π^* level of the NO unit to give a $^2\Pi_{3/2}$ electronic state. EPR parameters calculated for this species are in better agreement with those observed experimentally than for simple substitution of N^{2-} on O^{2-} sites to give $N_O^{\times}$ [14,20,31]. Within the Ti coordination sphere of the anatase structure it is possible to identify two distinct Ti-O distances: 4 O atoms are found with a Ti-O bondlength of 1.934 Å and 2 O atoms are found with a Ti-O bondlength of 1.980 Å[46,47]. It can be argued that the two different sets of EPR parameters are associated with the fact that interstitial N could in principle bind to either of the two distinct oxygen atoms. The theoretical work alluded to above did not consider the potential importance of the two distinct Ti-O bondlengths in anatase.

The concentrations of the paramagnetic centres in the four catalyst samples were determined by double integration of the EPR signal and comparison with a freshly prepared dilute solution of DPPH in toluene. The uncertainty in this spin counting quantification is typically around ± 20%. As shown in table 3, the spin concentrations of samples A, B and D are all 2.5×10^{18} mol^{-1} or higher (in the case of A). The spin concentration in sample C is however slightly lower with a value of 1.2×10^{18} mol^{-1}.

Provided the Fermi level of all doped samples lies at the bottom of the conduction band, the question on how the formation of any paramagnetic species at all is possible has to be addressed. The quadruply occupied π* level of the $(NO)'_O$ complex lies at an energy ΔE = 2.4 eV below the bottom of the conduction band, an energy defined experimentally by the onset of optical absorption in doped samples. Given that kT at room temperature is about 0.025 eV, the value of the Fermi-Dirac distribution function $F(E,T) = 1/(e^{\Delta E/kt} + 1)$ when ΔE = 2.4 eV is around 2 × 10^{-42}. Thus the probability of thermal ionisation of π* electrons is negligible. However it has been shown in previous EPR studies that the intensity of the paramagnetic signal increases dramatically under visible light irradiation[14,24,36,38] due to an excitation process:

$$(NO)'_O + h\nu \longrightarrow (NO)^{x}_O + e'$$

It is therefore possible that the EPR signals observed for all doped samples arises at least in part from photoexcited sites resulting from ambient illumination. Figure 4.8 shows that the nitrogen EPR signal of an N-doped sample measured under ordinary conditions of illumination in the laboratory decreases on protecting it from ambient light during the measurement. As seen Figure 4.8.a., the EPR signal assigned to the paramagnetic species $(NO)^{x}_O$ shows a pronounced decrease after one hour in darkness and further diminishes after four hours. However, soon after normal illumination is restored in the room, the original signal is almost 100% recovered, see figure 4.8.b. Similar observations have been reported in previous EPR measurements of N-doped TiO_2 under controlled irradiation.[24,48] It is interesting to note that the decreases of the EPR signal occurs slowly, while the increase to the original value occurs almost immediately. In a study done by Elio Giamello et.al,[24] the nitrogen EPR signal intensity

of samples measured in vacuum quickly increased when the samples was irradiated with blue light (λ = 437nm), and returned to its original value as soon as the light was turned off. However, when the same experiment was performed under an oxygen pressure of 5 KPa, the increased EPR signal remains at values higher than the original before irradiation, and an additional signal assigned to surface superoxide $O_2^{\cdot-}$ radical species was observed. This led the authors to conclude that the electrons in the conduction band (excited from nitrogen states) reduce adsorbed oxygen to form superoxide radicals. The rate of reduction of paramagnetic species $(NO)_O^{\times}$ to diamagnetic $(NO)_O'$ involves the re-oxidation of reduced species adsorbed on the surface (e.g. superoxide $O_2^{\cdot-}$ radical), and will therefore be inversely proportional to their stabilities.

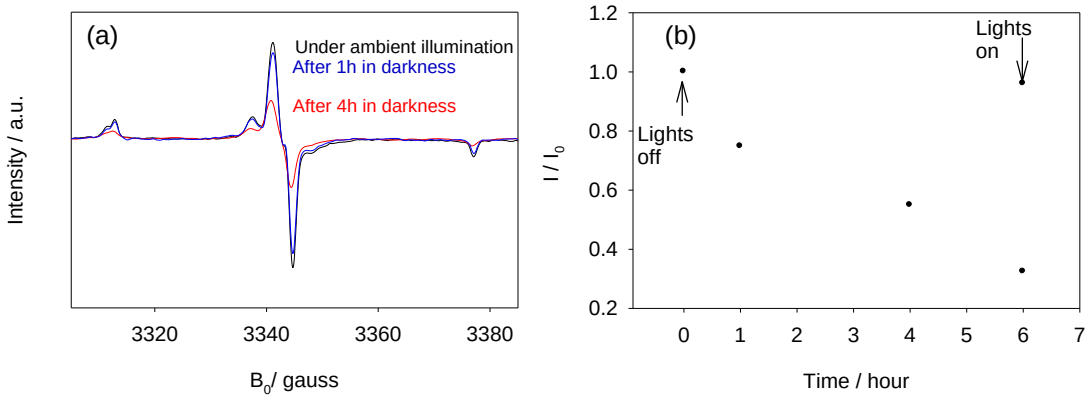


Figure 4.8 (a) Effects of laboratory illumination on the EPR spectrum of sample A. (b) EPR intensity at different times in darkness.

4.3.5 Catalytic activity.

The results of methylene blue degradation experiments are shown in figure 4.9. Results for all five samples studied using the 395 nm cutoff filter are given in figure 4.9.a. The undoped anatase sample U shows slight photocatalyic activity, probably due to the Urbach tail of absorption which extends down to about 3.0 eV. All samples that have

been doped with N show enhanced photocatalytic activity as compared with the reference. Samples A and B exhibit the highest activity and these samples have the highest surface area and smallest crystallite size. Samples C and D have lower activities than A and B and also have lower surface areas. However there is not a direct correlation between activity and surface area because D is more active than C even though it has a lower surface area. The influence of using 400 nm and 420 nm cutoff filters are shown in figure 4.9b for the undoped sample and for the most active N doped sample i.e. sample A. This figure also includes a repeat of measurements using the 395 nm filter: comparison between 4.8a and 4.8b serves to confirm the reproducibility of the catalytic measurements. It can be seen that undoped anatase shows no catalytic activity at all when using the 400 nm and 420 nm filters. By contrast sample A remains active, albeit with a reduced rate of degradation of methylene blue.

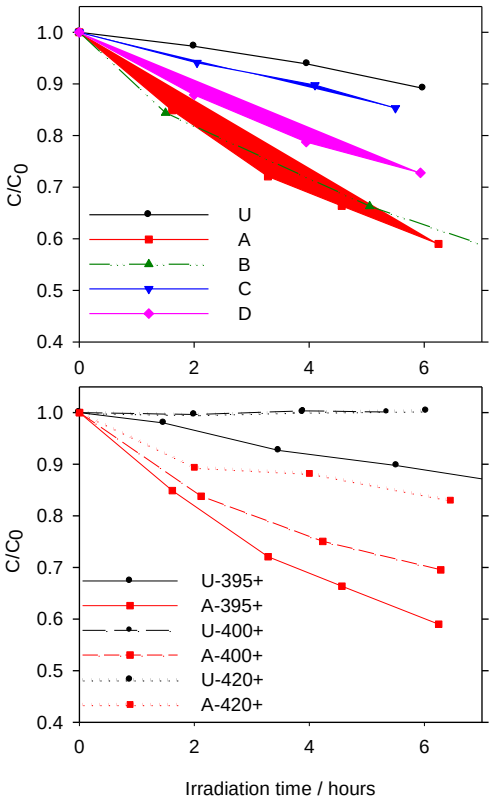


Figure 4.9 Plots showing variation in absorbance of methylene blue solutions after irradiation with filtered light from a Xe lamp in the presence of N-doped anatase photocatalysts (a) results for samples U and A-D using 395 nm filter (b) results for samples A and U using 395 nm, 400 nm and 420 nm filters.

Despite the very low concentration of paramagnetic centres, it is however striking that there appears to be a direct correlation between the concentration of paramagnetic centres and the photocatalytic activity. Thus the order of catalytic activities A>B>C shown in figure 4.9 mirrors the order of concentrations of paramagnetic centres given in table 4.3. The lower activity of sample D as compared with sample B, even though they have the same paramagnetic concentrations, is partly attributable to the lower surface area of D. This correlation between the concentration of paramagnetic centres and photocatalytic activity can be linked to the reason why the formation of any paramagnetic species at all is possible. As above explained, it is possible that the EPR signals observed for all doped samples arises at least in part from photoexcited sites resulting from ambient illumination. The steady state concentration of electrons and the $(NO)_O^x$ holes seen in EPR will be inversely related to the electron-hole recombination rate. The photocatalytic activity also depends on the concentration of electrons and holes, thus providing a link between the intensity of the EPR signal and the catalytic performance.

4.4 Conclusions.

All the N doped samples prepared in the present work display significant enhancement in visible region photocatalytic activity as compared to undoped anatase. Bulk and surface doping levels as determined by an inert gas fusion method and XPS respectively differ at most by a factor of two. XPS indicates that N close to the surface is mostly in a form with a characteristic binding energy close to 400 eV: this is ascribed to interstitial nitrogen bound to lattice oxygen to give an NO-like species. The present results do not establish definitively that this is the dominant mode of incorporation of N in the bulk of the samples, although this is not an unreasonable assumption. The

concentration of paramagnetic centres associated with N doping is around three orders of magnitude lower than the total concentration of N: in other words only around 0.1% of the $(NO)_O'$ centres are ionised to give paramagnetic $(NO)_O^\times$. These paramagnetic centres are therefore minority bulk species and are unlikely to provide the dominant contribution to the visible region optical absorption. Their concentration is also well below the limit of detectability in XPS. It is also clear that the empty hole states associated with the paramagnetic centres do not define the position of the the Fermi level. This this would lead to shifts to low binding energy in excess of 2eV for the valence band and Ti 2p structure and this is not observed. As mentioned previously the formation of diamagnetic $(NO)_O'$ requires the compensation of the $(NO)_O^\times$ acceptor states by electrons associated with doubly ionised oxygen vacancy sites. First principles density functional calculations have demonstrated that the energy required to create oxygen vacancies is reduced from a value of around 4.2 eV for undoped anatase to around 0.6 eV for N-doped anatase, provided that all the electrons associated with ionisation of the vacancies are trapped at an N dopant site[14,20]. Thus incorporation of N promotes the formation of oxygen vacancies and allows near-complete compensation of $(NO)_O^\times$ acceptor states.

Finally, considering the chemistry that is necessary to produce interstitial nitrogen doping in TiO_2 using NH_3 derived precursors, it must be recognized that N incorporation into the anatase lattice involves a net oxidation from the –III state found in NH_3 or NH_4^+ to –I as found in $(NO)_O'$. Given that the preparative procedure is carried out in air, ambient oxygen could act as the oxidising agent in the following reactions:

$$2NH_4^+ + O_2\,(g) + 3O_O^\times \rightarrow 2(NO)_O' + V_O^{\bullet\bullet} + 2H^+ + 3H_2O$$

Alternatively nitrate could act as the oxidising agent:

$$3NH_4^+ + NO_3^- + 6O_O^\times \rightarrow 4(NO)_O' + 2V_O^{\bullet\bullet} + 5H_2O + 2H^+$$

4.5 References

(1) Asahi, R.; Morikawa, T.; Ohwaki, T.; Aoki, K.; Taga, Y. *Science* **2001**, *293*, 269.

(2) Batzill, M.; Morales, E. H.; Diebold, U. *Chemical Physics* **2007**, *339*, 36.

(3) Batzill, M.; Morales, E. H.; Diebold, U. *Physical Review Letters* **2006**, *96*.

(4) Chambers, S. A.; Cheung, S. H.; Shutthanandan, V.; Thevuthasan, S.; Bowman, M. K.; Joly, A. G. *Chemical Physics* **2007**, *339*, 27.

(5) Cheung, S. H.; Nachimuthu, P.; Joly, A. G.; Engelhard, M. H.; Bowman, M. K.; Chambers, S. A. *Surface Science* **2007**, *601*, 1754.

(6) Romero-Gomez, P.; Rico, V.; Borras, A.; Barranco, A.; Espinos, J. P.; Cotrino, J.; Gonzalez-Elipe, A. R. *Journal of Physical Chemistry C* **2009**, *113*, 13341.

(7) Yu, Y. P.; Xing, X. J.; Xu, L. M.; Wu, S. X.; Li, S. W. *Journal of Applied Physics* **2009**, *105*.

(8) Takahashi, I.; Payne, D. J.; Palgrave, R. G.; Egdell, R. G. *Chem. Phys. Lett.* **2008**, *454*, 314.

(9) Diwald, O.; Thompson, T. L.; Zubkov, T.; Goralski, E. G.; Walck, S. D.; Yates, J. T. *Journal of Physical Chemistry B* **2004**, *108*, 6004.

(10) Yu, A. M.; Wu, G. J.; Zhang, F. X.; Yang, Y. L.; Guan, N. J. *Catalysis Letters* **2009**, *129*, 507.

(11) Wang, J.; Tafen, D. N.; Lewis, J. P.; Hong, Z. L.; Manivannan, A.; Zhi, M. J.; Li, M.; Wu, N. Q. *Journal of the American Chemical Society* **2009**, *131*, 12290.

(12) Chen, X. F.; Wang, X. C.; Hou, Y. D.; Huang, J. H.; Wu, L.; Fu, X. Z. *Journal of Catalysis* **2008**, *255*, 59.

(13) Peng, F.; Cai, L. F.; Yu, H.; Wang, H. J.; Yang, J. *Journal of Solid State Chemistry* **2008**, *181*, 130.

(14) Di Valentin, C.; Finazzi, E.; Pacchioni, G.; Selloni, A.; Livraghi, S.; Paganini, M. C.; Giamello, E. *Chemical Physics* **2007**, *339*, 44.

(15) Qiu, X. F.; Burda, C. *Chemical Physics* **2007**, *339*, 1.

(16) Burda, C.; Lou, Y. B.; Chen, X. B.; Samia, A. C. S.; Stout, J.; Gole, J. L. *Nano Letters* **2003**, *3*, 1049.

(17) Chen, X. B.; Burda, C. *Journal of Physical Chemistry B* **2004**, *108*, 15446.

(18) Livraghi, S.; Votta, A.; Paganini, M. C.; Giamello, E. *Chemical Communications* **2005**, 498.

(19) Nosaka, Y.; Matsushita, M.; Nishino, J.; Nosaka, A. Y. *Science and Technology*

of Advanced Materials **2005**, *6*, 143.

(20) Di Valentin, C.; Pacchioni, G.; Selloni, A.; Livraghi, S.; Giamello, E. *Journal of Physical Chemistry B* **2005**, *109*, 11414.

(21) Chen, X. B.; Lou, Y. B.; Samia, A. C. S.; Burda, C.; Gole, J. L. *Advanced Functional Materials* **2005**, *15*, 41.

(22) Sathish, M.; Viswanathan, B.; Viswanath, R. P.; Gopinath, C. S. *Chemistry of Materials* **2005**, *17*, 6349.

(23) Li, H. X.; Li, J. X.; Huo, Y. I. *Journal of Physical Chemistry B* **2006**, *110*, 1559.

(24) Livraghi, S.; Paganini, M. C.; Giamello, E.; Selloni, A.; Di Valentin, C.; Pacchioni, G. *Journal of the American Chemical Society* **2006**, *128*, 15666.

(25) Cong, Y.; Zhang, J. L.; Chen, F.; Anpo, M. *Journal of Physical Chemistry C* **2007**, *111*, 6976.

(26) Reyes-Garcia, E. A.; Sun, Y. P.; Reyes-Gil, K.; Raftery, D. *Journal of Physical Chemistry C* **2007**, *111*, 2738.

(27) Yang, W. D.; Lin, W. C.; Yang, C. H.; Chung, Z. J.; Huang, I. L. *Journal of Materials Research* **2009**, *24*, 2574.

(28) Xing, M. Y.; Zhang, J. L.; Chen, F. *Applied Catalysis B-Environmental* **2009**, *89*, 563.

(29) Nadtochenko, V.; Denisov, N.; Gorenberg, A.; Kozlov, Y.; Chubukov, P.; Rengifo, J. A.; Pulgarin, C.; Kiwi, J. *Applied Catalysis B-Environmental* **2009**, *91*, 460.

(30) *Practical Surface Analsysis*; Briggs, D.; Seah, M. P., Eds.; John Wiley: Chichester, 1994.

(31) Napoli, F.; Chiesa, M.; Livraghi, S.; Giamello, E.; Agnoli, S.; Granozzi, G.; Pacchioni, G.; Di Valentin, C. *Chemical Physics Letters* **2009**, *477*, 135.

(32) Souto, S.; Alvarez, F. *Applied Physics Letters* **1997**, *70*, 1539.

(33) Livraghi, S.; Chierotti, M. R.; Giamello, E.; Magnacca, G.; Paganini, M. C.; Cappelletti, G.; Bianchi, C. L. *Journal of Physical Chemistry C* **2008**, *112*, 17244.

(34) Livraghi, S.; Czoska, A. M.; Paganini, M. C.; Giamello, E. *Journal of Solid State Chemistry* **2009**, *182*, 160.

(35) Livraghi, S.; Elghniji, K.; Czoska, A. M.; Paganini, M. C.; Giamello, E.; Ksibi, M. *Journal of Photochemistry and Photobiology a-Chemistry* **2009**, *205*, 93.

(36) Li, D.; Ohashi, N.; Hishita, S.; Kolodiazhnyi, T.; Haneda, H. *Journal of Solid*

State Chemistry **2005**, *178*, 3293.

(37) Joung, S. K.; Amemiya, T.; Murabayashi, M.; Itoh, K. *Applied Catalysis a-General* **2006**, *312*, 20.

(38) Yamamoto, Y.; Moribe, S.; Ikoma, T.; Akiyama, K.; Zhang, Q.; Saito, F.; Tero-Kubota, S. *Molecular Physics* **2005**, *104*, 1733.

(39) Wang, Y. Q.; Yu, X. J.; Sun, D. Z. *Journal of Hazardous Materials* **2007**, *144*, 328.

(40) Xie, Y.; Zhao, Q. N.; Zhao, X. J.; Li, Y. Z. *Catalysis Letters* **2007**, *118*, 231.

(41) Tang, H.; Levy, F.; Berger, H.; Schmid, P. E. *Physical Review B* **1995**, *52*, 7771.

(42) Delfino, M.; Fair, J. A.; Hodul, D. *Journal of Applied Physics* **1992**, *71*, 6079.

(43) Prieto, P.; Kirby, R. E. *Journal of Vacuum Science & Technology a-Vacuum Surfaces and Films* **1995**, *13*, 2819-2826.

(44) Swartz, W. E.; Alfonso, R. A. *Journal of Electron Spectroscopy and Related Phenomena* **1974**, *4*, 351.

(45) Rodriguez, J. A.; Jirsak, T.; Liu, G.; Hrbek, J.; Dvorak, J.; Maiti, A. *Journal of the American Chemical Society* **2001**, *123*, 9597.

(46) Horn, M.; Schwerdt.Cf; Meagher, E. P. *Zeitschrift Fur Kristallographie* **1972**, *136*, 273.

(47) Labouriau, A.; Earl, W. L. *Chemical Physics Letters* **1997**, *270*, 278.

(48) Konstantinova, E. A.; Kokorin, A. I.; Lips, K.; Sakthivel, S.; Kisch, H. *Applied Magnetic Resonance* **2009**, *35*, 421.

Chapter 5: Control of valence states in Rh-doped TiO_2 by Sb co-doping: a study by high resolution X-ray photoemission spectroscopy.

5.1 Introduction

Historically, cation doping was used as an approach to increase visible light absorption by TiO_2 before anion doping was considered.[1,2] Studies of over 20 different metal dopants in TiO_2 have led to a well-established understanding of the effects of the cation doping on the UV-visible absorption of TiO_2.[2] It is known that doping with transition metal ions leads to new states within the bandgap of TiO_2.[3] Although these may be associated with optical absorption in the visible region, paramagnetic centres may also act as electron/hole trapping sites or as recombination centres.[2] The Ti site in both polymorphs of TiO_2 has approximately octahedral site symmetry. For this reason dopant cations with a d^6 electron configuration and which are likely to favour a low spin state are of particular interest because the closed t_{2g}^6 shell will lead to diamagnetic dopant centres. Trivalent Co(III), Rh(III) and Ir(III) are all nd^6 ions, but of course they are not isovalent with Ti(IV). Thus doping these transition elements into TiO_2 will lead to oxidation to the M(IV) state which has an open shell t_{2g}^5 configuration unless additional compensating dopants or defects are present. Kudo and coworkers[4] studied co-doping of Rh-doped TiO_2 with Sb(V). On the basis of x-ray absorption spectroscopy and electron paramagnetic resonance spectroscopy it was argued that Sb co-doping did indeed suppress formation of t_{2g}^5 Rh(IV). Moreover the Sb co-doping led to markedly improved photocatalystic performance. In fact the same strategy of co-doping with higher valent ions such as Nb(V), Ta(V) or Sb(V) has also been shown to lead to improved photocatalytic activity even when doping with non-isovalent open shell

cations such as Cr(III)[5,6] and Ni(II)[7] in TiO_2 and $SrTiO_3$.

This chapter presents a study of high resolution X-ray photoemission valence band spectra of both Rh-doped and Rh/Sb codoped TiO_2. This enables us to locate the position of the Rh 4d states within the bandgap of TiO_2 and also to explore shifts in the position of the Fermi level induced by Sb co-doping. At the same time the changes in XPS may be used to explain very pronounced changes in diffuse reflectance spectra induced by co-doping with Sb.

5.2 Experimental section

5.2.1 Preparation of solids

Ceramic samples of $Rh_{0.01}Ti_{0.99}O_2$ and $Rh_{0.01}Sb_{0.01}Ti_{0.98}O_2$ were prepared by solid state reaction between rutile TiO_2 (Aldrich, 99.9%) and Rh_2O_3, with addition of Sb_2O_5 for the co-doped sample. Stoichiometric quantities of the oxide powders were ground together in an agate mortar and pestle and pelletised between tungsten carbide dies. Following the synthetic conditions used by Kudo and coworkers[4] to prepared Rh-doped and Rh/Sb-codoped samples, the pellets were placed in recrystallised alumina boats and fired for 10 hours at 1150°C to give robust ceramic discs. Heating ramp used to reach this firing temperature was 200ºC/min.

5.2.2 Characterization

Powder X-ray Diffraction (XRD), carried out on a Panalytical X'Pert Pro instrument using monochromated Cu $K\alpha_1$ radiation, was used to assess phase purity. X-ray photoemission spectra were measured in a Scienta ESCA 300 spectrometer located at the National Centre for Electron Spectroscopy and Surface Analysis at Daresbury

Laboratory, UK. This incorporates a rotating anode Al Kα ($h\nu$ = 1486.6 eV) X-ray source, a seven crystal monochromator and a 300 mm mean radius spherical sector analyser with parallel electron detection system. The effective instrument resolution was 0.40 eV. For most samples it was necessary to use an electron flood gun to stabilise the surface charge. Use of a flood gun shifts all spectral features to high kinetic energy. Photoelectron spectra were therefore charge calibrated using the weak C 1s contaminant peak which was assigned a binding energy of 285.0 eV. It was confirmed that this calibration procedure places the Fermi level of metallic thin film samples on highly insulating substrates (e.g. degenerately Sn-doped In_2O_3 on zirconia substrates) at zero binding energy, which ensure that the binding energies in all spectra are relative to the Fermi level of the sample. Diffuse reflectance (DR) spectra were measured in the visible and near ultraviolet (UV) region using a Perkin Elmer Lambda 750S instrument incorporating a 60 cm integrating sphere.

5.3 Results and discussion

5.3.1 X-Ray Diffraction

Figure 5.1 shows powder X-ray diffraction patterns of pure and doped samples. All patterns contain strong peaks characteristic of the rutile phase with no peaks associated with impurity phases. Detail of the rutile 110 peak shows that there is a small shifts in the positions of the diffraction peaks to low angle were observed in the doped samples, consistent with the fact that the ionic radii of Rh^{3+} (r = 66.5 pm), Rh^{4+} (r = 61.5 pm) and Sb^{5+} (r = 61 pm) in 6-coordinate environments are all slightly greater than the tabulated value for Ti^{4+} (r = 60.5 pm).[8]

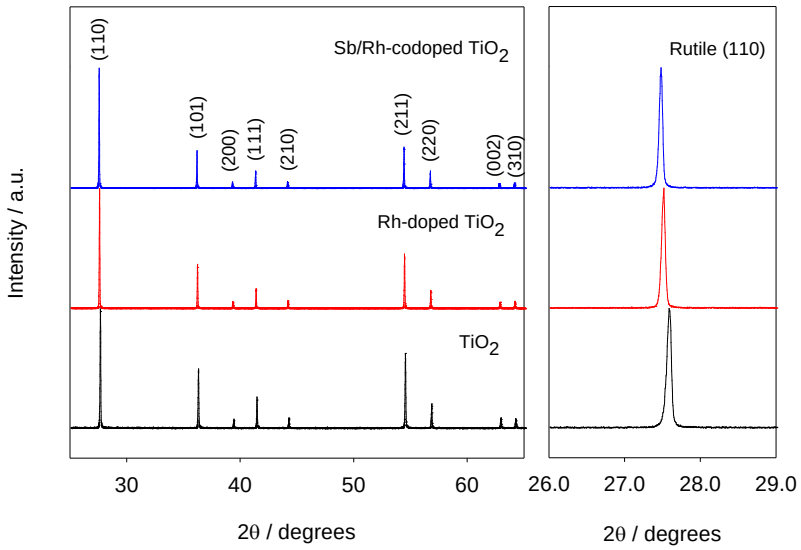


Figure 5.1. X-ray diffraction patterns of pure TiO_2, Rh-doped TiO_2 and Sb/Rh-codoped TiO_2 produced by high temperature solid state reaction. A single set of rutile peaks is observed in each case.

5.3.2 X-ray photoelectron spectroscopy

Valence band and shallow core level photoemission spectra of undoped TiO_2, Rh-doped TiO_2 and Rh/Sb-codoped TiO_2 are shown in panels a and b of figure 5.2. Intensities have been normalized relative to the O 2*s* peak which appears at about 22 eV binding energy. Expanded scans of the valence band region itself are shown in panels c and d. Rh doping introduces a fairly strong and well-defined peak above the top of the main O 2*p* valence band. This is associated with Rh 4*d* states. The high intensity even at a doping level of 1% may be attributed to the fact that the one electron cross section for ionisation of Rh 4*d* states has a value of 1.5 kB that is very much bigger than the cross section of 0.06 kB for ionisation of O 2*p* states at a photon energy of 1486.6 eV. At the same time Rh doping alone leads to a shift to low binding energy of around 0.5 eV for the main O 2*p* valence band. This shift is mirrored by shifts to lower binding energy for the Ti 2*p* and O 1*s* core level peaks (figure 5.3) and suggests that Rh doping pins the Fermi level below the position found for nominally undoped TiO_2. Here the Fermi level

lies just below the conduction band minimum and is defined by Ti 3d states associated with oxygen vacancies. Thus in nominally undoped rutile TiO_2 the valence band onset is found at around 3 eV, corresponding to the bulk bandgap of TiO_2.

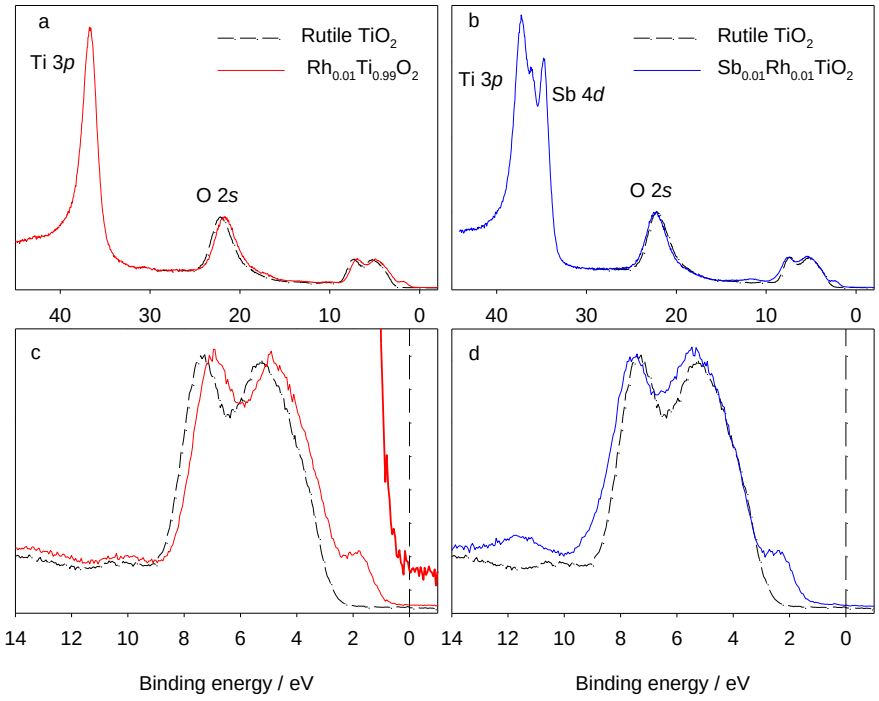


Figure 5.2. Valence band photoelectron and shallow core levels spectra of samples studied in this work. Spectral intensities are normalized relative to the O 2s core line at 22 eV. (a) Valence band photoelectron spectra of TiO2 and 1% Rh-doped TiO2 ($Rh_{0.01}Ti_{0.99}O_2$) encompassing O 2*p* bands, the O 2*s*. (b) Valence band photoelectron spectra of TiO_2 and 1% Rh / 1% Sb-codoped TiO_2 ($Sb_{0.01}Rh_{0.01}Ti_{0.98}O_2$) encompassing O 2*p* bands, the O 2s band and shallow core Sb 4*d* and Ti 3*p* levels. (c) Detail of the O 2*p* valence bands of TiO_2 and 1% Rh-doped TiO_2. (b) Detail of the O 2*p* valence bands of TiO_2 and 1%Rh/1% Sb-codoped TiO_2.

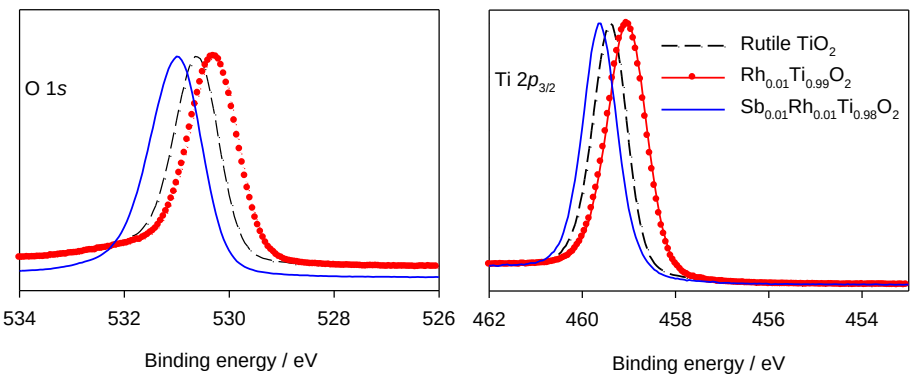


Figure 5.3. O 1s and Ti 2p3/2 core level spectra for TiO_2, $Rh_{0.01}Ti_{0.99}O_2$ and $Sb_{0.01}Rh_{0.01}Ti_{0.98}O_2$.

As seen in figure 5.2, Sb co-doping leads to several changes in the valence band and shallow core region. Firstly, the valence band shifts to higher binding energy so that the main valence band edge is found at roughly the same position as for undoped TiO_2. The core levels (figure 5.3) show a similar shift to high binding energy and in fact O 1*s* and Ti 2*p* core binding energies in Rh/Sb co-doped TiO_2 are slightly higher than in undoped TiO_2. In addition the Rh 4*d* structure shows a small shift toward the O 2*p* bandedge so that it appears as a shoulder rather than peak. Secondly Sb co-doping leads to appearance of a new peak at 34.4 eV binding energy along with a second peak which overlaps the Ti 3*p* peak at around 37.0 eV.[9] Curve fitting the composite spectral profile allows us to assign this structure to the Sb $4d_{5/2}$ peak, which is separated from the Sb $4d_{3/2}$ component with a spin-orbit splitting of 1.2 eV.[10-12] Note that Kudo and co-workers[4] failed to recognise that the Ti 3p peak appears in this region and interpreted changes in spectra with change of Sb doping level purely in terms of changes in valence state rom Sb^{5+} to Sb^{3+}. From the measured intensity of the Sb 4*d* peaks and the Sb $3d_{3/2}$ core level peak the effective Sb/Ti ratio within the sampling depth of XPS was estimated to be around 0.08. This is clearly bigger than the bulk Sb doping level of 0.01 and indicates pronounced surface segregation of Sb. As discussed in detail elsewhere, the driving force for segregation is that reduced "lone pair" Sb(III) cations are easily accommodated in surface sites where the lack of inversion symmetry facilitates 5*s*-5*p* mixing.[13,14] Finally Sb doping leads to the appearance of a new peak below the bottom of the valence band at around 12.5 eV binding energy, as well as enhanced intensity and broadening in the lower half of the valence band. The new peak is attributed to O 2*p* states strongly hybridised with Sb 5*s* states: structure at around the same binding energy has recently been reported in XPS of In_5SnSbO_{12}[15]. Similarly the changes in the main

valence band are attributed to hybridisation of O 2*p* states with Sb 5*p* states, similar to the Sn 5*p*-O 2*p* hybridisation found in SnO_2[16-18] and $In_4Sn_3O_{12}$.[19] There is relatively little change at the top of the valence band as these states are of almost pure O 2p character.[20]

The shift in the position of the Fermi level as a consequence of Rh doping and the movement back to the original position with Sb codoping is attributed to a change in the Rh valence state from Rh(IV) in $Rh_{0.01}Ti_{0.99}O_2$ to Rh(III) in $Rh_{0.01}Sb_{0.01}Ti_{0.98}O_2$. As mentioned above the position of the Fermi level in nominally undoped TiO_2 is pinned by Ti(III) $3d^1$ states associated with the inevitable oxygen deficiency that is found in this n-type oxide. Introduction of t_{2g}^5 Rh(IV) onto Ti(IV) sites creates deep acceptor states that will compensate the Ti(III) states and pin the Fermi level at a lower energy defined by the *adiabatic* ionisation energy of the 4*d* states. Note that this energy lies above the *vertical* ionisation energy for Rh(IV) 4*d* states which determines the position of the peak maximum in photoemission: the energy difference between vertical and adiabatic energies is determined by the difference in energy between situations where there is screening of the photohole by electronic polarisation, which can take place on the timescale of the photoemission process, and one where there is further screening by relaxation of ionic positions in response to the generation of the photohole.[21] This vibrational relaxation is a slow process. Sb(V) co-doping adds extra electrons into the system and with equal concentrations of Rh and Sb there should be a complete filling of the t_{2g} states to give t_{2g}^6 Rh(III). This interpretation of the valence band XPS data is in accord with EPR experiments which reveal that there is almost complete quenching of the signal associated with open shell Rh(III) upon co-doping with Sb.[4] It is superficially surprising to find that that Sb co-doping leads to a shift of the Rh 3d peaks to 0.5 eV higher binding energy as seen in figure 5.4, given that it is being proposed a

decrease in oxidation state from (IV) to (III). It should however be remembered that as with the other core levels, the Rh binding energy is influenced by the upward shift in the position of the Fermi level consequent upon Sb co-doping. In addition one must recognise that the partial filling of acceptor states by donor electrons associated with oxygen vacancies will lead to co-existence of Rh(III) and Rh(IV) before co-doping with Sb. It is striking that the Rh $3d_{5/2}$ core line for the Sb/Rh co-doped sample is much narrower (FWHM = 0.73 eV) than the corresponding core line for the sample doped only with Rh (FWHM = 1.03 eV) The extra broadening is consistent with the coexistence of two different oxidation states in XPS of $Rh_{0.01}Ti_{0.99}O_{2-x}$ as well as with spin and orbital angular momentum coupling between the open shell t_{2g}^5 configuration and the Rh 3*d* photohole.[22]

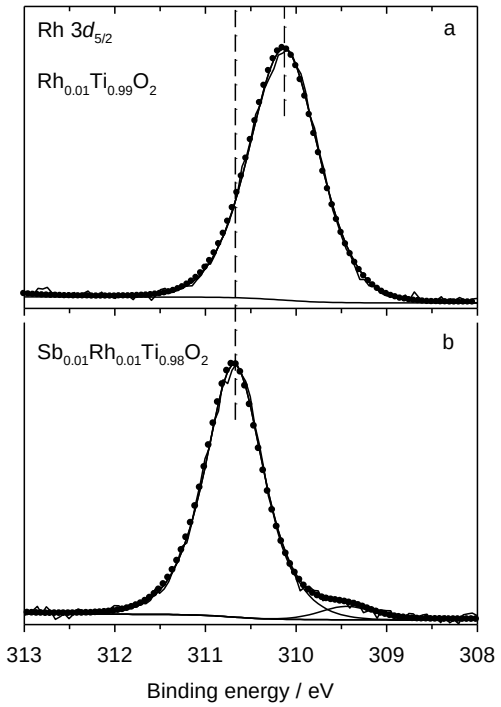


Figure 5.4. Rh $4d_{5/2}$ core level spectra for $Rh_{0.01}Ti_{0.99}O_2$ and $Sb_{0.01}Rh_{0.01}Ti_{0.98}O_2$.

5.3.3 UV/visible spectroscopy

The changes observed in photoemission may be used as a basis for rationalising the appearance of the optical spectra. For undoped TiO_2 the band-edge is observed at about 3.0 eV as expected from the value for the bulk bandgap. With Rh and Sb codoping an extra feature is observed as a strong shoulder to the main bandedge. This structure has maximum intensity in difference spectra at around 2.8 eV and extends down to about 2 eV. It therefore straddles most of the visible region and is responsible for the yellow-orange colouration of the co-doped sample. The ligand field splitting in $Rh(H_2O)_6^{3+}$ is estimated to be about 27,000 cm^{-1} i.e. 3.34 eV[23] and the empty e_g levels are therefore expected to lie above the conduction band minimum. Thus the extra structure in the optical spectrum of the co-doped sample is attributed to transitions from the filled Rh t_{2g}^6 levels into the empty Ti 3*d* conduction band. The energy of the feature observed in diffuse reflectance is in accord with the position of the Rh *4d* structure just above the O 2*p* band edge found in X-ray photoemission and the high intensity is compatible with assignment to an intersite metal to metal charge transfer transition rather than a dipole forbidden $4d \rightarrow 4d$ transition. For the sample doped with Rh alone a more complex spectrum is observed. The structure within the visible region shifts to somewhat lower energy and a second shoulder giving significant absorption intensity down to about 1.6 eV (800 nm) appears in the spectrum. This new structure is assigned to ligand to metal charge transfer transitions from states in the O 2*p* valence band into empty Rh 4*d* t_{2g}^5 states.

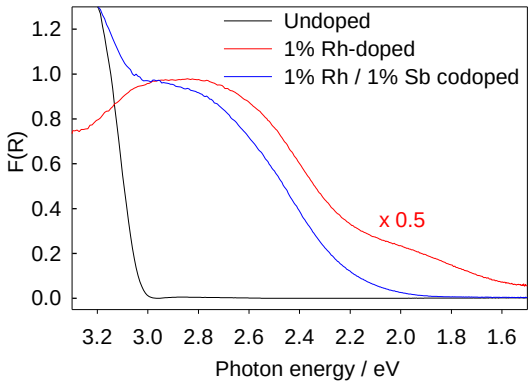


Figure 5.5. Diffuse reflectance spectra of undoped rutile TiO_2, $Rh_{0.01}Ti_{0.99}O_2$ and $Sb_{0.01}Rh_{0.01}Ti_{0.98}O_2$ presented in terms of the Kubelka-Munk function F(R) versus photon energy.

5.4 Conclusions

The main conclusions of this study are summarised in the schematic energy level diagrams based on the discussion given above shown in figure 5.6. In agreement with Kudo and co-workers, these results suggest that co-doping Sb into Rh-doped TiO_2 suppresses formation of Rh(IV) by a charge compensation mechanism. The Rh dopant is therefore present as Rh(III) with filled t_{2g}^6 levels and the Fermi level is defined by Ti(III) $3d^1$ states associated with oxygen deficiency. By contrast without Sb codoping there Rh is present as Rh(IV) with a t_{2g}^5 configurations. The holes in the t_{2g} levels can trap Ti 3*d* charge carriers associated with oxygen vacancies and the Fermi level is pinned below the value found in the co-doped material and in nominally undoped TiO_2.

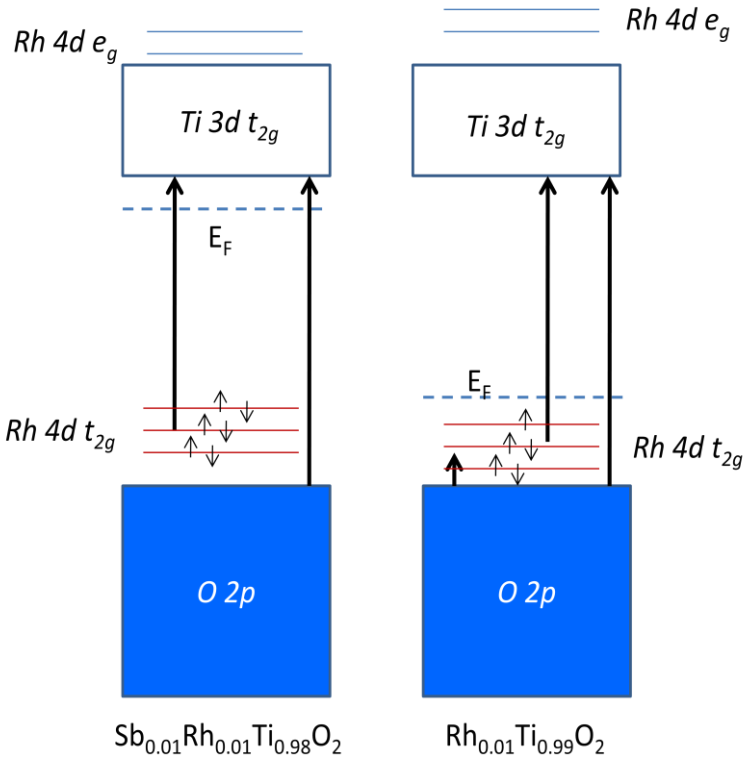


Figure 5.6. Schematic energy level diagrams for $Sb_{0.01}Rh_{0.01}Ti_{0.98}O_2$ and $Rh_{0.01}Ti_{0.99}O_2$

5.5 References

(1) Linsebigler, A. L.; Lu, G. Q.; Yates, J. T. *Chemical Reviews* **1995**, *95*, 735.

(2) Ni, M.; Leung, M. K. H.; Leung, D. Y. C.; Sumathy, K. *Renewable & Sustainable Energy Reviews* **2007**, *11*, 401.

(3) Mizushima, K.; Tanaka, M.; Asai, A.; Iida, S.; Goodenough, J. B. *Journal of Physics and Chemistry of Solids* **1979**, *40*, 1129.

(4) Niishiro, R.; Konta, R.; Kato, H.; Chun, W. J.; Asakura, K.; Kudo, A. *Journal of Physical Chemistry C* **2007**, *111*, 17420.

(5) Kato, H.; Kudo, A. *Journal of Physical Chemistry B* **2002**, *106*, 5029.

(6) Ishii, T.; Kato, H.; Kudo, A. *Journal of Photochemistry and Photobiology a-Chemistry* **2004**, *163*, 181.

(7) Niishiro, R.; Kato, H.; Kudo, A. *Physical Chemistry Chemical Physics* **2005**, *7*, 2241.

(8) Shannon, R. D.; Prewitt, C. T. *Acta Crystallographica Section B-Structural Crystallography and Crystal Chemistry* **1969**, *B 25*, 925.

(9) Oku, M.; Wagatsuma, K.; Kohiki, S. *Physical Chemistry Chemical Physics* **1999**, *1*, 5327.

(10) Kang, J. S.; Park, J. G.; Olson, C. G.; Youn, S. J.; Min, B. I. *Journal of Physics-Condensed Matter* **1995**, *7*, 3789.

(11) Cox, P. A.; Egdell, R. G.; Harding, C.; Patterson, W. R.; Tavener, P. J. *Surf. Sci.* **1982**, *123*, 179.

(12) Egdell, R. G.; Flavell, W. R.; Tavener, P. *J. Solid State Chem.* **1984**, *51*, 345.

(13) Gulino, A.; Taverner, A. E.; Warren, S.; Harris, P.; Egdell, R. G. *Surface Science* **1994**, *315*, 351.

(14) Gulino, A.; Condorelli, G. G.; Fragala, I.; Egdell, R. G. *Applied Surface Science* **1995**, *90*, 289.

(15) O'Neil, D. H.; Egdell, R. G.; Edwards, P. P. *Journal of Applied Physics* **2010**, *107*.

(16) Themlin, J. M.; Sporken, R.; Darville, J.; Caudano, R.; Gilles, J. M.; Johnson, R. L. *Physical Review B* **1990**, *42*, 11914.

(17) Egdell, R. G.; Walker, T. J.; Beamson, G. *Journal of Electron Spectroscopy and Related Phenomena* **2003**, *128*, 59.

(18) Egdell, R. G.; Rebane, J.; Walker, T. J.; Law, D. S. L. *Phys. Rev. B* **1999**, *59*,

1792.

(19) O'Neil, D. H.; Walsh, A.; Jacobs, R. M. J.; Kuznetsov, V. L.; Egdell, R. G.; Edwards, P. P. *Physical Review B* **2010**, *81*, 085110.

(20) Mo, S. D.; Ching, W. Y. *Physical Review B* **1995**, *51*, 13023.

(21) Taverner, A. E.; Rayden, C.; Warren, S.; Gulino, A.; Cox, P. A.; Egdell, R. G. *Physical Review B* **1995**, *51*, 6833.

(22) Hüfner, S. *Photoelectron Spectroscopy: principles and aplications*; Third edition ed.; Springer: Beling, 2003.

(23) Figgis, B. N.; Hitchman, M. A. *Ligand Field Theory and its Applications*; Wiley VCH: New York, 2000.

Chapter 6 Electronic and structural properties of $Sn_xTi_{1-x}O_2$ ($0.0 \leq x \leq 0.1$) solid solutions.

6.1 Introduction

Mixed oxides of TiO_2 and SnO_2 are of interest in the field of gas sensing, where they give enhanced response to H_2 and CO compared to the pure binary oxides,[1-5] and in the field of photocatalysis, where improved activity under UV light[6-13] and visible light[14,15] have been reported. In both gas sensing and photocatalysis it has been found that small additions of SnO_2 to TiO_2 give the most beneficial results[2,9]. In both cases the electronic structure of the material is critical for to the functional behaviour. TiO_2 and SnO_2 both adopt the tetragonal rutile structure, although the lattice parameters for SnO_2 (a = 4.737 Å, c = 3.360 Å) are somewhat bigger than those for TiO_2 (a = 4.594 Å, c = 2.959 Å). Substitutional solid solutions $Sn_xTi_{1-x}O_2$ which retain the rutile structure of the end members are obtained by reaction between SnO_2 and TiO_2 at elevated temperatures.[2,16,17] Above 1450°C solid solutions across the complete composition range $0.0 < x < 1.0$ are thermodynamically stable.[18] Below 1450°C there is a roughly symmetrical miscibility gap, within which solid solution undergo spinodal decomposition into Sn and Ti rich phases.[19-21] However, such decomposition is slow at room temperature, and rapid quenching of compositions close to the end members ($x < 0.2$, $x > 0.8$) gives single phase samples which are stable for long periods;[17,22,23] alternatively, metastable compositions can be made close to room temperature under kinetic control.[24]

While the individual electronic structures of TiO_2 and SnO_2 have been well studied over many years,[25-30] the electronic structures of $Sn_xTi_{1-x}O_2$ solid solutions have been investigated only recently, and chiefly by theoretical means.[31-33] Rutile TiO_2 and SnO_2 both have direct bandgaps of magnitude 3.062 eV and 3.596 eV respectively.[34-36] In SnO_2 the valence and conduction bands are both offset to lower energies in comparison with TiO_2. Thus when TiO_2 and SnO_2 are bought together in a heterojunction, photoexcited electrons from TiO_2 are transferred across the interface to the SnO_2 phase with no applied voltage,[13,37,38]. This suggests that the SnO_2 conduction band minimum is lower in energy than TiO_2, a conjecture corroborated by theoretical calculations.[39]

Sensato *et al.* performed periodic density functional theory (DFT) calculations on rutile $Sn_xTi_{1-x}O_2$ and predicted a monotonic increase of the direct band gap with increasing Sn content, but also the presence of a lower energy (2.9 eV) indirect band gap present at low Sn concentrations.[31] Taft *et al.* performed DFT calculations on Sn doped TiO_2 (110) surfaces, and found the nature and magnitude of the band gap to be highly dependent on the location of the substitutional Sn^{4+} defect.[32] For most substitutional sites, the direct bandgap of TiO_2 was found to increase with the addition of Sn, but it was also found that the fundamental inter-band transition may become smaller and indirect. Long *et al.*, also using DFT, found a decrease in the band gap of rutile TiO_2 upon Sn doping caused by the lowering of the conduction band energy.[33] Higher levels of Sn doping were however found to cause an increase in the band gap. While these theoretical studies are interesting, there has been little detailed experimental work of the electronic structure of $Sn_xTi_{1-x}O_2$.

This chapter presents a detailed experimental study of the structural and electronic properties of $Sn_xTi_{1-x}O_2$ solid solutions in the composition range $0.0 \leq x \leq 0.10$. Structural changes were investigated using X-ray diffraction and Raman spectroscopy. The magnitude of the optical bandgap was determined through diffuse reflectance (DR) spectroscopy and changes in the valence band were measured using high resolution X-ray photoelectron spectroscopy (XPS). Results from both techniques showed narrowing of the bandgap at low Sn doping levels, which is of prime importance for potential visible light photocatalytic applications.

6.2 Experimental Section

6.2.1 Preparation of the solids

Rutile TiO_2 (Aldrich, 99.9%) and SnO_2 (Alrich, 99.9%) powders were weighed in the desired ratio and ground together in an agate mortar. The resulting mixture was placed in recrystallised alumina boats and heated to 1200°C in air for 3 to 6 days. To avoid the spinodal decomposition that can occur during slow cooling, the samples were quenched by removal from the furnace at 1200°C into air, followed by cooling on the bench top. Samples were put in and out the furnace at 600ºC and taken to the desired temperature without any specific heating rate.

6.2.2 Characterization

Powder X-ray Diffraction (XRD), carried out on a Panalytical X'Pert Pro instrument using monochromated Cu $K\alpha_1$ radiation, was used to assess phase purity. Samples found to be multi-phase were reground and refired at 1200 °C until a single phase was obtained. High resolution X-ray photoemission spectra (XPS) were recorded on a

Scienta ESCA 300 spectrometer located at Daresbury Laboratory, UK, which incorporated a rotating anode Al K_α ($h\nu$ =1486.6 eV) X-ray source. The X-ray source was run with 200 mA emission current and 14 kV anode bias, while the analyzer operated at 150 eV pass energy with 0.8 mm slits. Gaussian convolution of the analyzer resolution with a linewidth of 260 meV for the monochromated X-ray source gives an effective instrument resolution of 400 meV. The spectrometer was calibrated regularly to set the Fermi edge of a silver reference sample at zero binding energy. Powder samples of Sn-doped TiO_2 were prepared for XPS analysis by pressing into indium foil. Extra care was taken to ensure that the coverage of the indium foil was complete, and that no In peaks appeared in the photoelectron spectra. A weak C 1s peak was evident in most spectra with a C 1s to O 1s intensity ratio typically around 0.03. After correction for atomic sensitivity factors this corresponds to a surface C/O ratio of about 0.08. Given that around 10% of the signal in Al Kα XPS derives from the topmost atomic layer this corresponds to just under 1 monolayer of surface hydrocarbon contamination. Fortunately the ionisation cross sections at $h\nu$ = 1486.6 eV for C 2p (5 barns) and H 1s (0.2 barns) states are very much lower than those for O 2p (60 Barns) or Ti 3d (85 Barns) states, so that the contamination layer will contribute around only 1% of the intensity in valence band photoemission spectra. For most samples it was necessary to use an electron flood gun to stabilise the surface charge. Use of a flood gun shifts all spectral features to high kinetic energy. Photoelectron spectra were therefore charge calibrated using the weak C 1s contaminant peak which was assigned a binding energy of 285.0 eV. Diffuse reflectance (DR) spectra were measured in the visible and near ultraviolet (UV) region using a Perkin Elmer Lambda 750S instrument incorporating a 60 cm integrating sphere. Raman spectra were recorded at room

temperature using a Perkin Elmer RamanStation 400F spectrometer with excitation by a He/Ne laser.

6.3 Results and discussion

6.3.1 X-Ray Diffraction

Figure 6.1 shows X-ray diffraction patterns of the $Sn_xTi_{1-x}O_2$ solid solution over the range of concentrations studied. A single set of diffraction peaks characteristic of a single rutile phase was observed for all samples. A shift of the diffraction peaks toward lower 2θ angles with increasing Sn content was observed, which is a consequence of the expansion of the TiO_2 unit cell due to substitutional incorporation of Sn onto Ti sites.[9,22,40]

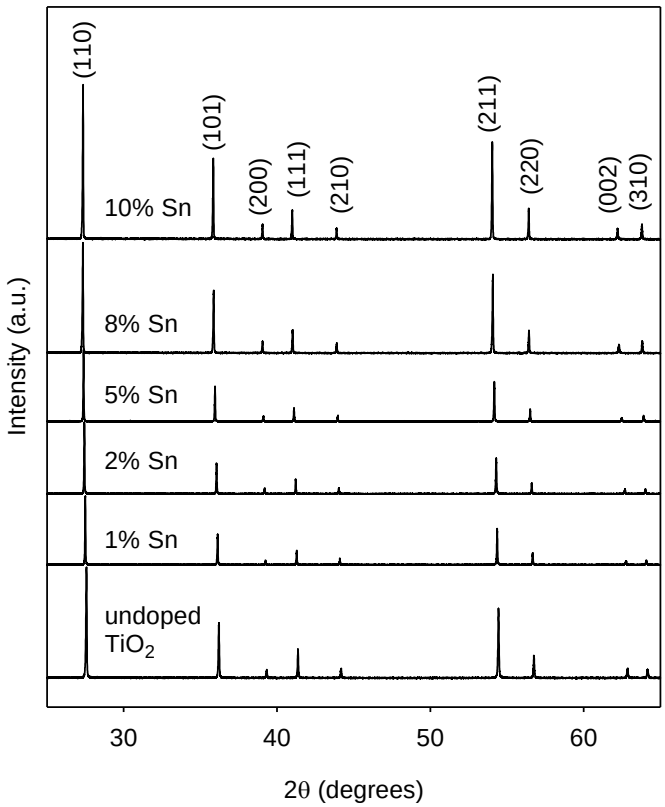


Figure 6.1 X-ray diffraction patterns (Cu $K\alpha_1$) for $Sn_xTi_{1-x}O_2$ solid solutions of the compositions indicated produced by high temperature solid state reaction. A single set of rutile peaks is observed in each case.

From the position of the diffraction peaks, the tetragonal lattice parameters *a* and *c* were calculated. In figure 6.2, the values of *a* and *c* are plotted as a function of x for $Sn_xTi_{1-x}O_2$. The unit cell volume $V = a^2c$ is also presented. It can be clearly seen that both lattice parameters and unit cell volume of the solid solutions increase with x, indicating the lattice expansion. However, the increase of the *a* and *c* values is not linear with Sn concentration, *i.e.* there is a positive deviation from Vegard's law in both *a* and *c*. Such a deviation from Vegard's law has been reported for this system before.[22,31,41] Although deviation from Vegard's law is frequently accompanied by phase separation caused by spinodal decomposition,[31] the phase purity of the samples found by XRD analysis suggests this decomposition not to be the cause of the deviation. In their theoretical work, Sensato *et al.* found marked deviations from the Vegard's law for phase pure $Sn_xTi_{1-x}O_2$ solid solutions,[31] which indicated that deviation may have an origin other than spinodal decomposition, as experimentally shown in this work. As shown in figure 2 the deviation found for the *a* lattice parameter was greater than that found for the *c* parameter. This result can be related to the anisotropy in compressibility (κ) for the rutile TiO_2, being $\kappa_a = 1.93\times10^{-4}$ $kbar^{-1}$ along the *a* axis and $\kappa_c = 0.87\times10^{-4}$ $kbar^{-1}$ along the *c* axis.[42] These values indicate that in TiO_2 the displacement of ions in the [100] direction is larger than the displacement in the [001] direction when external forces are applied on a crystal. Therefore, a larger deviation of the *a* parameter may be a result of a more effective relaxation in the [100] direction of the stress brought about by incorporation of the larger Sn^{4+} cation. This analysis, which makes use of the compressibility values for undoped rutile TiO_2, may be valid for the low Sn concentrations studied here. However, in SnO_2, the anisotropy of the compressibilities is reversed in comparison to TiO_2, *i.e.* in SnO_2 $\kappa_c > \kappa_a$,[42] and in studies

of the whole range of composition for $Sn_xTi_{1-x}O_2$ solid solutions, different behaviour of the *a* and *c* lattice parameters are found in each region of composition.[22,31]

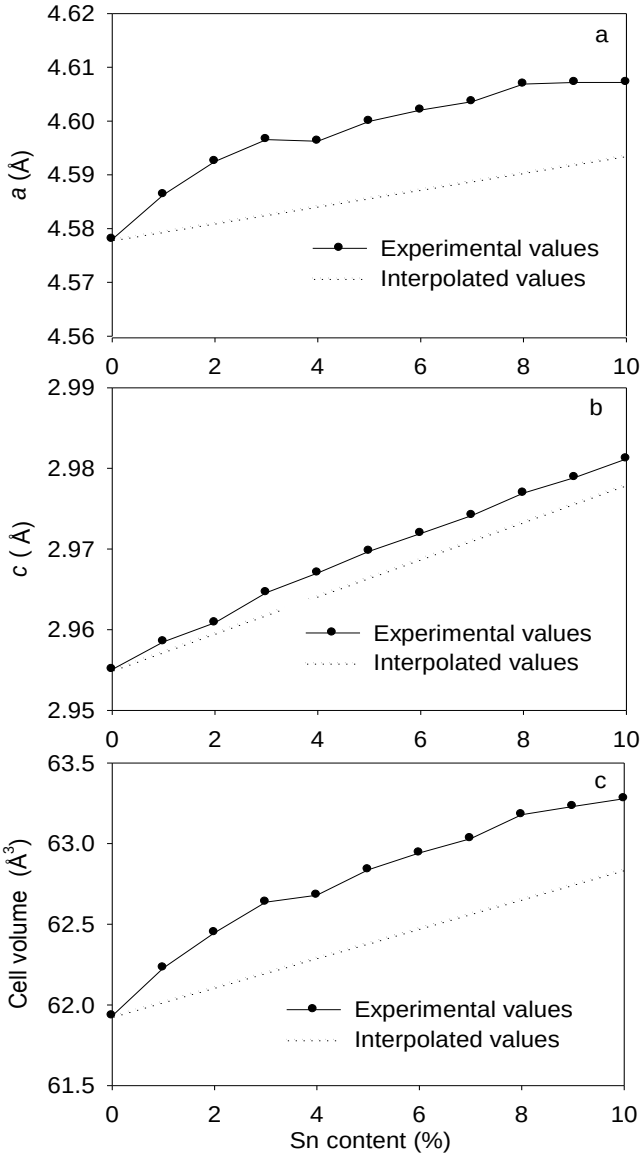


Figure 6.2 Experimentally determined lattice parameters and cell volume of $Sn_xTi_{1-x}O_2$ solid solutions with 0 – 10 % Sn content. Dotted lines show linearly interpolated values linking the TiO_2 and SnO_2 end members (Vegard's Law)

6.3.2 Raman Spectroscopy

Rutile TiO_2 and SnO_2 belong to the space group D_{4h} ($P4_2/mnm$) and display four Raman active fundamental vibrational modes, $A_{1g} + B_{1g} + B_{2g} + E_g$.[43] Raman spectra

taken on the undoped TiO_2 sample showed peaks at 143 cm^{-1}, 447 cm^{-1} and 610 cm^{-1} which are assigned in accordance with the literature to the B_{1g}, E_g and A_{1g} vibrations respectively, as shown in figure 6.3.

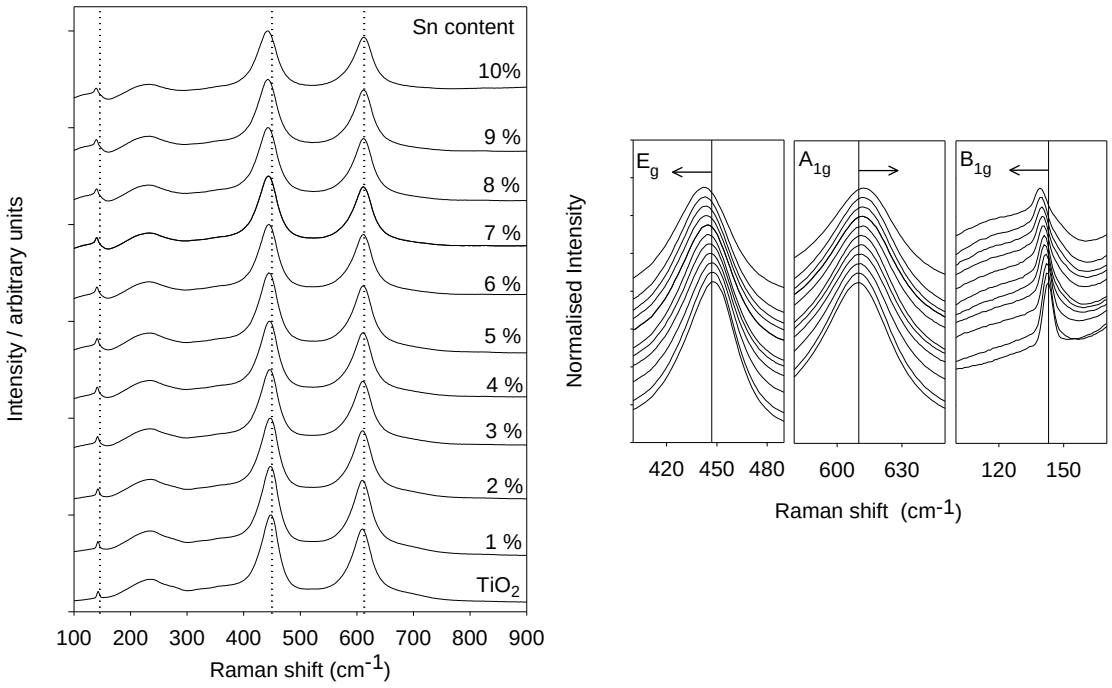


Figure 6.3 Left, Raman spectra of $Sn_xTi_{1-x}O_2$ solid solutions with 0-10 % Sn content. Dotted vertical lines show the positions of TiO_2 Raman peaks. Right, expanded views of the E_g, A_{1g} and B_{1g} Raman peaks. The solid vertical line shows the TiO_2 peak position and the arrow indicates the change caused by increasing Sn doping.

The broad feature around 235 cm^{-1} is a combination band,[43,44] and the B_{2g} vibration, expected at 826 cm^{-1} is not observed due to its weak intensity.[22] Sn doping did not cause the appearance of any additional bands, but increasing Sn doping has differing effects on the frequencies of the fundamental vibrations. The B_{1g} and the E_g vibrations show a general shift to lower frequencies with increasing Sn doping, while the opposite trend is seen in the A_{1g} vibration, *i.e.* there is a shift to *higher* frequencies. In each case, the change in frequency is close to linear with Sn concentration (Figure 6.4). The frequency of vibrational modes can be affected by particle size for nano-scale crystals.

However, since there is no significant variation in crystallite size in these samples as determined from the full width at half maximum height (FWHM) of the diffraction peaks, this effect cannot explain the variations in Raman shifts seen here. In SnO_2 (TiO_2), the B_{1g}, E_g and A_{1g} vibrations appear at 123 (143) cm^{-1}, 475 (447) cm^{-1} and 634 (610) cm^{-1} respectively. Thus, while dilute doping of TiO_2 with Sn causes the A_{1g} and B_{1g} to vibrations shift *towards* their SnO_2 values, the E_g vibration shifts *away* from its value in SnO_2 value. Hirata *et al.* studied the Raman spectra of $Sn_xTi_{1-x}O_2$ solid solutions across the whole composition range and also found the frequency of the E_g fundamental vibrational mode to be non-linear with *x*.[22]

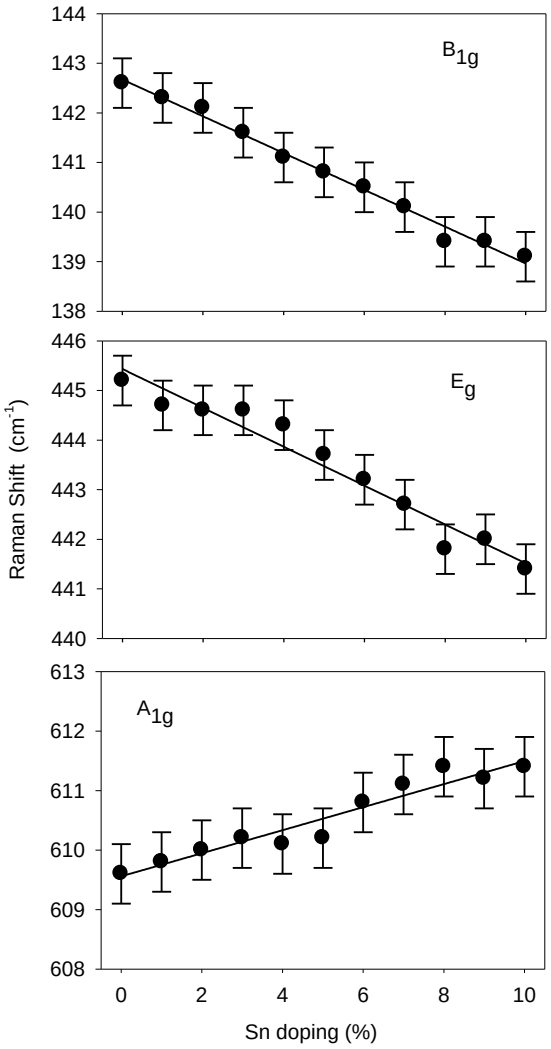


Figure 6.4. Peak positions of the B_{1g}, E_g and A_{1g} bands in Raman spectra of $Sn_xTi_{1-x}O_2$ solid solutions with changing Sn content.

6.3.3 Optical Band Gap

From the UV-visible diffuse reflectance data, the absorption spectra of the samples were calculated by means of the Kubelka-Munk remission function (as described in chapter 2). Figure 6.5a shows the absorption of samples in the range of concentration studied. The spectra of all samples show the characteristic broad absorption band that TiO_2 presents due to its fundamental band gap transition. A close examination of the band absorption in the spectra of the samples shows that the spectral edges of the doped samples are shifted toward higher wavelength compared with the undoped TiO_2.

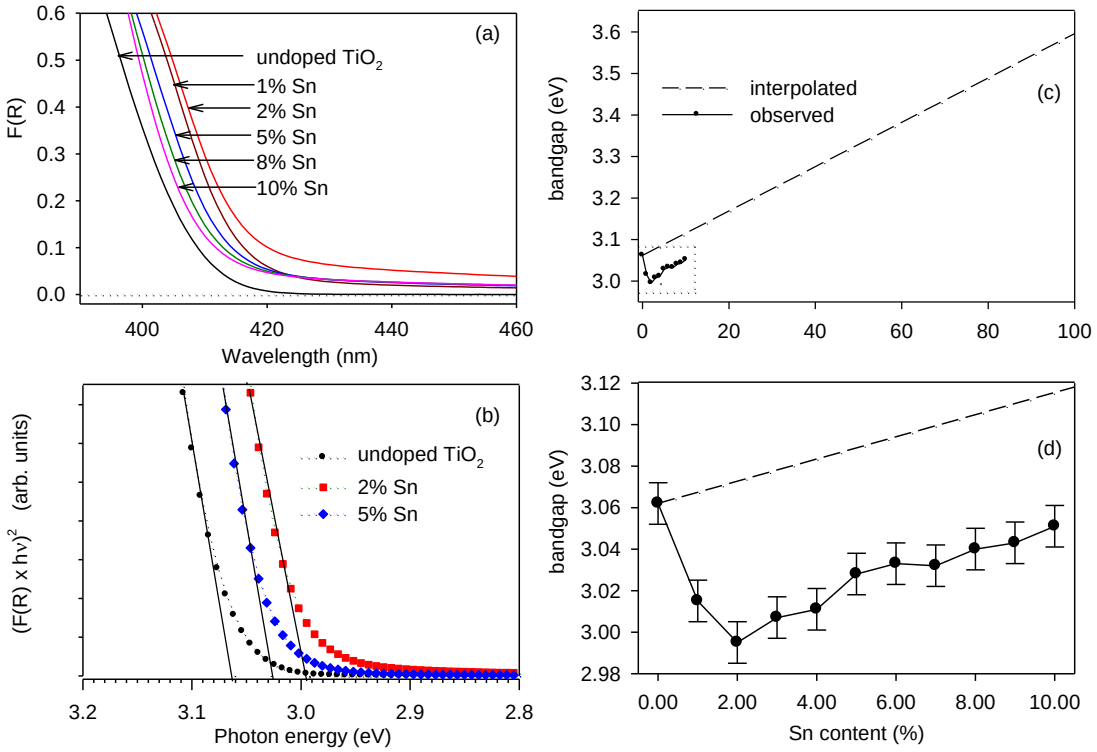


Figure 6.5 (a) Kubelka-Munk remission function F(R) derived from diffuse reflectance spectra, for several representative samples of $Sn_xTi_{1-x}O_2$ of the compositions indicated close to the band edge. The shift in band edge with doping is apparent. (b) Band gap plots of $(F(R)h\nu)^2$ for several representative samples, showing extrapolation of the straight line portion to determine the direct band gap. (c) and (d) Variation in optical band gap of $Sn_xTi_{1-x}O_2$ with varying Sn concentration. Dashed line is a linear interpolation between the band gap values for TiO_2 (3.062 eV) and SnO_2 (3.596 eV). Negative band bowing is apparent.

Typically, in a plot absorption coefficient (α) versus photon energy ($h\nu$), the absorption edge can be fitted to a power law relationship:

$$\alpha(\nu) = \frac{B(h\nu - E_g)^n}{h\nu}$$

where B is a constant, E_g is the band-gap energy, and n is an integral or half-integral value that depends on the model used for the electronic transition. Values of $n = ½$ and $n = 2$ result in a linear fit for direct and indirect transitions respectively.[45] This model has been extensively used in the study of optical properties of many type of samples, *e.g.* TiO_2 thin films[46] and powder, CdS thin films[47], and SnO_2 thin films and nanopowder.[48] As F(*R*) is proportional to α, it can be seen that the linear portion of a plot $[F(R)\ h\nu]^{1/n}$ versus $h\nu$ intercepts the abscissa at $h\nu = E_g$, and this type of plot is commonly used in the estimation of the band gap energy of semiconductors.[46,48,49] Using n = ½, the model for direct band gap transitions, good linear fits were obtained as shown in figure 6.5(b). Figure 6.5(c) and 6.5(d) show values of band gap of all samples estimated by using this method, as a function of Sn-concentration. It can be seen that the band-gap decreases with increasing Sn doping at low doping levels and reaches a minimum for 2% Sn doped TiO_2. At higher Sn doping levels the band gap increases monotonically with increasing Sn doping, although it does not converge onto the value obtained by linear interpolation between the limits for TiO_2 and SnO_2 within the range of compositions investigated. Thus it appears that negative band bowing occurs in the $Sn_xTi_{1-x}O_2$ system at low doping levels. It should be noted that some experimental and theoretical studies have found a monotonic increase of the band gap as the Sn concentration increases. [31,50] However these earlier investigations involved the complete composition range with broad steps of x = 0.1 between different samples. Thus the behaviour at very low doping levels was not identified. In more recent theoretical work, Long *et. al.*[33] found a band gap reduction of 0.12 eV when one Sn is

substituted for Ti in a rutile 2 × 2 × 2 supercell (i.e. 1 Ti in every 16) to give a material with 6.25 % Sn doping. The band gap increases by 0.06 eV from the reduced value when the doping level is increased to 12.5 % corresponding to one Sn atom in a 2 × 2 × 1 supercell, although there still an overall reduction of 0.06 eV at this doping level. Qualitatively at least these theoretical results mirror the experimental findings of this study.

It is important to note that as well as leading to a shift in the band edge, Sn doping leads to a very broad but quite weak tail of absorption that extends across much of the visible region down to around 700 nm (corresponding to an energy of 1.7 eV), as shown in figure 6.6. As discussed below this extra structure is tentatively assigned to reduced Sn^{2+} cations occupying sites at surfaces or grain boundary interfaces.

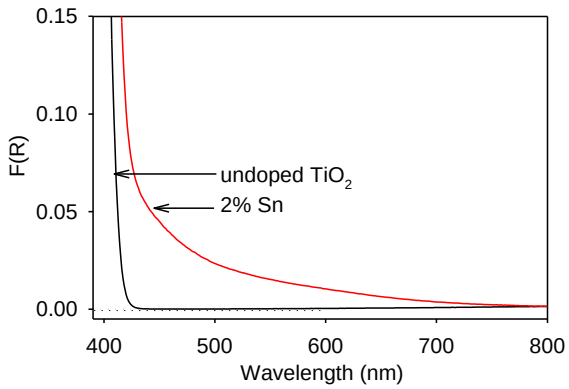


Figure 6.6. Comparison of F(R) for undoped and 2% Sn doped TiO_2 over the visible region, showing a pronounced tail into the visible region in the doped sample.

6.3.4 X-ray photoelectron spectroscopy

The reduction of the band gap of $Sn_xTi_{1-x}O_2$ at low Sn concentrations observed by optical spectroscopy can be caused either by an increase in energy of the valence band

maximum (VBM) or a decrease in energy of the conduction band minimum (CBM), or both effects simultaneously. XPS is able to test the first of these possibilities through measurement of the filled valence band states, and it may be determined whether filled states exist in doped samples above the VBM of undoped TiO_2. The second possibility might be tested through measurement of the shift in spectral lines that would be caused by a lowering of the CBM. In n-type semiconductors, the Fermi level is pinned near to the CBM by donor states. Thus a reduction in energy of the CBM will lead to a reduction in energy of the Fermi level, and a consequent shift in the observed photoelectron spectrum. In practice there are caveats to this use of XPS to investigate valence band structure and Fermi level position. The short mean free path of electrons within a solid means that Al Kα XPS necessarily measures surface rather than bulk electronic structure. At the surface, the valence band and conduction band are likely to be offset (bent) away from their bulk positions by surface electronic states, and correspondingly the Fermi level at the surface may be different to that in the bulk. Secondly, filled surface states within the band gap may be present in photoemission spectra which do not reflect the bulk electronic structure. Finally binding energies in XPS are affected by both initial and final state effects.

Valence band and shallow core level photoelectron spectra of TiO_2 and several Sn doped TiO_2 samples are shown in Figure 6.7. For comparison, the intensity in each spectrum in Figure 6.7 has been normalised to the O 2*s* peak which appears at a binding energy of 22.2 eV, and varies less than 0.1 eV in energy between samples. The most readily identified change in the spectra on addition of Sn is the emergence of a doublet with principle component at a binding energy of 25.7 eV and splitting of 0.7 eV. This

peak increases in intensity with increasing Sn content and is assigned as the Sn 4*d* core line.[51]

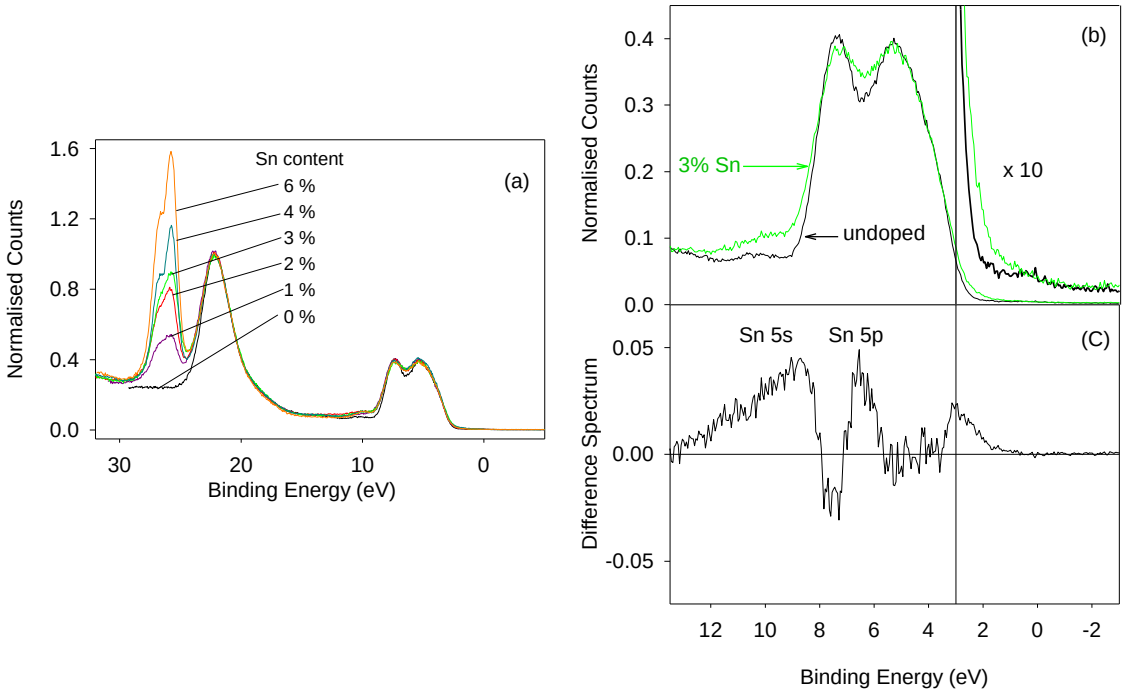


Figure 6.7. (a) Valence band photoelectron spectra of TiO_2 and $Sn_xTi_{1-x}O_2$ solid solutions (Sn concentrations 1%, 2%, 3%, 4%, 6%) encompassing O 2p bands, the O 2s band and shallow core Sn 4d levels. Spectral intensities are normalised relative to the O 2s core line at 22.2 eV. (b) Detail of the O 2p valence bands of TiO_2 and 3% $Sn_xTi_{1-x}O_2$. The vertical line at 3.06 eV denotes the bandgap of undoped rutile TiO_2. (c) Difference spectrum (3% Sn doped – undoped) showing changes due to Sn doping. Labels refer to contributions of metal orbitals to the total density of states.

The valence band itself straddles binding energies between 3.0 - 12.0 eV and is shown in detail for undoped TiO_2 and 3% Sn doped TiO_2 in Figure 6.7. Experimental spectra are referenced to the Fermi level, which is pinned to the bottom of the conduction band in n-type semiconductors such as TiO_2 and SnO_2.[52] Sn derived states in the valence band of $Sn_xTi_{1-x}O_2$ with small values of *x* will appear at lower binding energies relative to the Fermi level than they do in SnO_2, since SnO_2 has a significantly larger band gap (3.60 eV) than TiO_2 (3.06 eV). Therefore in order to compare Sn-induced features in the current spectra with valence band spectra of SnO_2 it is necessary to take account of

a shift to low binding energy of about 0.5 eV. Despite significant covalency in both TiO_2 and SnO_2, bandstructure calculations show that the top of the valence bands in both TiO_2 and SnO_2 are composed primarily of O 2*p* states with only small contributions from the metal cations.[35,53] As a consequence, the upper part of the valence band shows only small changes upon substituting Sn onto Ti sites within the doping range investigated in this study, and these changes are best illustrated in the difference spectra shown in Figure 6.7. Each Sn doped sample showed very similar changes in this region, and so for clarity, in Figure 6.7 only spectra from undoped TiO_2 and 3% Sn doped TiO_2 are shown. Upon Sn doping, there is an increase in spectral weight between binding energies of 8.0 eV - 11.5 eV, with the greatest increase at a binding energy of 8.5 eV. There is also a separate sharp increase in spectral weight centred at a binding energy of 6.5 eV. After inclusion of the 0.5 eV correction, these two energies correspond to the regions of the valence band of SnO_2 where there is pronounced hybridisation of Sn 5*s* and Sn 5*p* states respectively with O 2*p* states.[53] The broad feature with maximum at 8.5 eV is therefore assigned to hybridised Sn 5*s* – O 2*p* states, while the sharper feature at 6.5 eV is assigned to hybridised Sn 5*p* – O 2*p* states. Both Long *et al.* and Sensato *et al.* in their respective DFT studies of bulk $Sn_xTi_{1-x}O_2$ predicted contributions from Sn to the valence band states at energies close to those found in the present work.[31,33] It is also observed a decrease in spectral weight upon Sn doping at a binding energy of 7.5 eV. This binding energy corresponds very well to that of the Ti 3*d* contribution to the valence band of TiO_2.[35] Therefore the changes in the valence band can be linked with the introduction of Sn derived states and the removal of Ti derived states that would occur upon substitutional doping of Sn for Ti. As expected from the calculations the top of the valence band spectra from 5.5 eV to 4.0 eV shows almost no change upon Sn doping, as this region is composed

almost entirely of O 2*p* derived states and has close to zero contribution from the metal cations. However, there is another significant change in the valence band spectra: an increase in spectral weight above the VBM of TiO_2 upon Sn doping, which can clearly be seen in the difference spectrum in Figure 6.7. Each Sn doped sample showed an increase in this region, and the difference spectra for several samples between binding energies of 3.0 – 0 eV are shown in Figure 6.8a. It can be seen that the integrated area above the VBM increases from 0% to 4% Sn doping and then falls from 4% to 6% Sn doping. The increase is dominated not by the small shift in the position of the valence band edge but by the tail of states extending into the bandgap. Note also that the maximum in the intensity of structure structure above 3 eV is found for 4% Sn doping whereas the maximum shift in the optical onset deduced from diffuse reflectance spectra is found at 2% Sn doping. A similar tailing of filled states above the VBM has been observed in SnO_2, and such states have been assigned to hybridised 5*s*-5*p* "lone pair" states associated with Sn(II) occupying surface sites. The reduction from Sn(IV) in the bulk to Sn(II) at the surface arises from oxygen deficiency at the surface.[28,51,52,54] If the cause of the states observed above the VBM is oxygen deficiency, it is interesting to note that the characteristic band gap feature of oxygen deficient TiO_2 surfaces, the Ti^{3+} 3*d* peak with binding energy 0.7 eV,[52] was not observed in any of the samples. In accordance with the idea that there is a significant concentration of Sn(II) occupying surface sites it was found that the intensity of the Sn 3*d* core level peaks relative to that of Ti 2*p* was always higher than expected from the bulk doping level as is evident from data presented in table 6.1. As has been discussed in detail elsewhere "lone pair" cations such as Sn(II) are more easily accommodated in surface sites than in bulk sites, thus providing a driving force for surface segregation.[54]

Table 6.1 Comparison of bulk and surface x values defined by formula $Sn_xTi_{1-x}O_2$

Bulk value of x[a]	Surface value of x[b]
0.01	0.020
0.02	0.049
0.03	0.048
0.04	0.060
0.06	0.091

[a] defined by stoichiometry of starting mixture.
[b] from XPS measurements on Sn 3*d* and Ti 2*p* core lines after correction with atomic sensitivity factors.

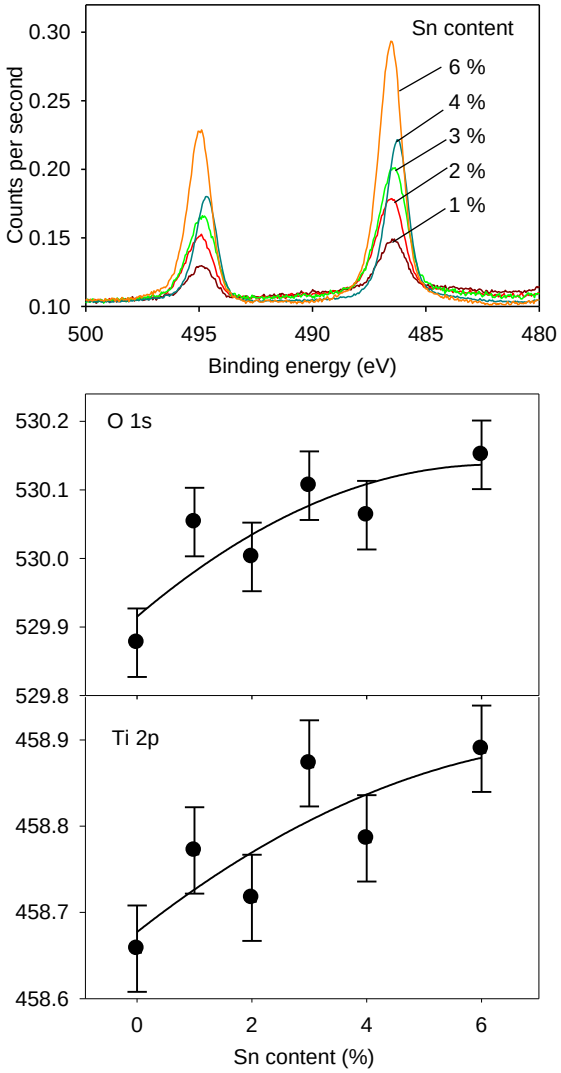


Figure 6.8 (a) Sn 3d core line photoelectron spectra of $Sn_xTi_{1-x}O_2$ solid solutions with the Sn contents indicted. (b) Variation in O 1s and Ti 2p core level binding energies in $Sn_xTi_{1-x}O_2$ solid solutions with increasing Sn content.

As it can be seen in figure 6.9, the Ti 2*p* and O 1*s* core lines show a shift to higher binding energy upon increasing Sn doping, while the Sn 3d core line shows no systematic variation in binding energy. If the CBM, and consequently the Fermi level, had decreased in energy, then a decrease in binding energy would be expected for the whole spectrum. However, the small change in CBM energy, estimated to be around 0.12 eV by Long *et.al.* might be masked by a larger core line chemical shift arising from final state effects. The averaged high frequency dielectric constant of SnO_2 ($\varepsilon_{av}(\infty) = 3.91$) is much smaller than that of TiO_2 ($\varepsilon_{av}(\infty) = 7.37$)[55] so that final state screening will be less pronounced in the former material as it is less polarizable. This will lead to a contribution to the chemical shift toward higher binding energy.

6.4 Conclusions

Phase pure $Sn_xTi_{1-x}O_2$ solid solutions have been prepared and characterised. Diffuse reflectance spectroscopy has clearly shown that Sn doping leads to narrowing of the band gap of TiO_2 in the concentration range investigated, with a minimum band gap of 2.995 eV at 2% Sn doping. In addition Sn doping leads to a broad tail of absorption that extends down to around 1.77 eV. XPS showed changes in the valence band density of states consistent with the substitution of Sn(IV) onto Ti(IV) sites, and additionally the presence new states above valence band maximum of undoped TiO_2 associated with segregated Sn(II) cations occupying surface sites. A small shift of the main valence band edge to low binding energy was also observed. The shift of the band edge is correlated with the shift in the main optical absorption onset whereas the surface gap states produce a tail of weak absorption extending across the visible range. Band bowing of the sort found here has been very extensively studied in III-V

semiconductors.[56] However there has been less work on oxide systems and the extent of band bowing in oxide "alloys" such as $A_xZn_{1-x}O$ (A = Ca, Cd, Mg)[57] and $Si_xM_{1-x}O_2$ (M = Zr or Hf)[58] is expected to be rather small. Moreover no distinct minimum in the band gap is predicted by first principles calculations when the "wide gap" cation is substituted onto the host site. It has been argued that pronounced band bowing is only expected when the host and substituent ions have very different electronegativities.[59] The present finding of a distinct minimum in the band gap when Sn substitutes for Ti is somewhat surprising given that that the difference in electronegativity (on the Allred-Rochow scale) between Sn (1.72) and Ti (1.32) is less than between say Si (1.74) and Hf (1.23) or Zr (1.32). Although further theoretical work may be needed to explain the apparently anomalous behaviour in $Sn_xTi_{1-x}O_2$ solid solutions, this band gap narrowing as well as other characteristic like the absorption across the visible region and surface tin segregation observed in $Sn_xTi_{1-x}O_2$ solid solutions, have very important practical implications as will be discussed in the next two chapters.

6.4 References

(1) Zakrzewska, K. *Thin Solid Films* **2001**, *391*, 229.

(2) Radecka, M.; Zakrzewska, K.; Rekas, M. *Sensors and Actuators B-Chemical* **1998**, *47*, 194.

(3) Carney, C. M.; Yoo, S.; Akbar, S. A. 10th International Meeting on Chemical Sensors, Tsukuba, JAPAN, 2004; p 29-33.

(4) Tai, W. P.; Oh, J. H. *Sensors and Actuators B-Chemical* **2002**, *85*, 154.

(5) Carotta, M. C.; Gherardi, S.; Guidi, V.; Malagu, C.; Martinelli, G.; Vendemiati, B.; Sacerdoti, M.; Ghiotti, G.; Morandi, S.; Bismuto, A.; Maddalena, P.; Setaro, A. *Sensors and Actuators B-Chemical* **2008**, *130*, 38.

(6) Cai, Z. Q.; Shen, Q. H.; Gao, J. W.; Yang, H. *Journal of Inorganic Materials* **2007**, *22*, 733.

(7) Fresno, F.; Guillard, C.; Coronado, J. M.; Chovelon, J. M.; Tudela, D.; Soria, J.; Herrmann, J. M. *Journal of Photochemistry and Photobiology a-Chemistry* **2005**, *173*, 13.

(8) Fresno, F.; Coronado, J. A.; Tudela, D.; Soria, J. *Applied Catalysis B-Environmental* **2005**, *55*, 159.

(9) Lin, J.; Yu, J. C.; Lo, D.; Lam, S. K. *Journal of Catalysis* **1999**, *183*, 368.

(10) Jing, L. Q.; Fu, H. G.; Wang, D. J.; Wei, X.; Sun, J. Z. *Acta Physico-Chimica Sinica* **2005**, *21*, 378.

(11) Cao, Y. A.; Yang, W. S.; Zhang, W. F.; Liu, G. Z.; Yue, P. L. *New Journal of Chemistry* **2004**, *28*, 218.

(12) Lin, C. F.; Wu, C. H.; Onn, Z. N. *Journal of Hazardous Materials* **2008**, *154*, 1033.

(13) Tada, H.; Hattori, A.; Tokihisa, Y.; Imai, K.; Tohge, N.; Ito, S. *Journal of Physical Chemistry B* **2000**, *104*, 4585.

(14) Sayilkan, F.; Asiltuerk, M.; Tatar, P.; Kiraz, N.; Sener, S.; Arpac, E.; Sayilkan, H. *Materials Research Bulletin* **2008**, *43*, 127.

(15) Kutty, T. R. N.; Avudaithai, M. *Chemical Physics Letters* **1989**, *163*, 93.

(16) Sinclair, W. R.; Loomis, T. C. *Angewandte Chemie-International Edition* **1958**, *70*, 603.

(17) Drobeck, D. L.; Virkar, A. V.; Cohen, R. M. *Journal of Physics and Chemistry of Solids* **1990**, *51*, 977.

(18) Naidu, H. P.; Virkar, A. V. *Journal of the American Ceramic Society* **1998**, *81*, 2176.

(19) Nambu, S.; Oiji, M. *Journal of the American Ceramic Society* **1991**, *74*, 1910.

(20) Cohen, R. M.; Drobeck, D.; Virkar, A. V. *Journal of the American Ceramic Society* **1988**, *71*, C401.

(21) Kong, L. B.; Ma, J.; Huang, H. *Journal of Alloys and Compounds* **2002**, *336*, 315.

(22) Hirata, T.; Ishioka, K.; Kitajima, M.; Doi, H. *Physical Review B* **1996**, *53*, 8442.

(23) Kulshreshtha, S. K.; Sasikala, R.; Sudarsan, V. *Journal of Materials Chemistry* **2001**, *11*, 930.

(24) Uchiyama, H.; Imai, H. *Chemical Communications* **2005**, 6014.

(25) Robertson, J. *Physical Review B* **1984**, *30*, 3520.

(26) Mazzone, A. M. *Philosophical Magazine Letters* **2004**, *84*, 275.

(27) Freeman, C. M.; Catlow, C. R. A. *Journal of Solid State Chemistry* **1990**, *85*, 65.

(28) Cox, D. F.; Fryberger, T. B.; Semancik, S. *Physical Review B* **1988**, *38*, 2072.

(29) Batzill, M.; Diebold, U. *Progress in Surface Science* **2005**, *79*, 47.

(30) Glassford, K. M.; Chelikowsky, J. R. *Physical Review B* **1992**, *46*, 1284.

(31) Sensato, F. R.; Custodio, R.; Longo, E.; Beltran, A.; Andres, J. *Catalysis Today* **2003**, *85*, 145.

(32) Sambrano, J. R.; Nobrega, G. F.; Taft, C. A.; Andres, J.; Beltran, A. *Surface Science* **2005**, *580*, 71-79.

(33) Long, R.; Dai, Y.; Huang, B. *Journal of Physical Chemistry C* **2009**, *113*, 650.

(34) Robertson, J. *Journal of Physics C-Solid State Physics* **1979**, *12*, 4767.

(35) Mo, S. D.; Ching, W. Y. *Physical Review B* **1995**, *51*, 13023.

(36) Maki-Jaskari, M. A.; Rantala, T. T. *Physical Review B* **2001**, *64*, 075407.

(37) Vinodgopal, K.; Kamat, P. V. *Environmental Science & Technology* **1995**, *29*, 841.

(38) Zhou, M. H.; Yu, J. G.; Liu, S. W.; Zhai, P. C.; Jiang, L. *Journal of Hazardous Materials* **2008**, *154*, 1141.

(39) Beltran, A.; Andres, J.; Sambrano, J. R.; Longo, E. *Journal of Physical Chemistry A* **2008**, *112*, 8943.

(40) Uchiyama, H.; Imai, H. *Chemical Communication* **2005**, 6014.

(41) Park, M.; Mitchell, T. E.; Heuer, A. H. *Journal of the American Ceramic Society* **1975**, *58*, 43.

(42) Peercy, P. S.; Morosin, B. *Physical Review B* **1973**, *7*, 2779.

(43) Porto, S. P. S.; Fleury, P. A.; Damen, T. C. *Physical Review* **1967**, *154*, 522.

(44) Ma, H. L.; Yang, J. Y.; Dai, Y.; Zhang, Y. B.; Lu, B.; Ma, G. H. *Applied Surface Science* **2007**, *253*, 7497.

(45) Smith, R. A. *Semiconductors*; Second ed.; Cambridge University Press: Cambridge, 1978.

(46) Mahanty, S.; Roy, S.; Sen, S. *Journal of Crystal Growth* **2004**, *261*, 77.

(47) Biswas, S.; Hossain, M. F.; Takahashi, T.; Kubota, Y.; Fujishima, A. *Thin Solid Films* **2008**, *516*, 7313.

(48) Deng, H. M.; Hossenlopp, J. M. *Journal of Physical Chemistry B* **2005**, *109*, 66.

(49) Pang, G. S.; Chen, S. G.; Koltypin, Y.; Zaban, A.; Feng, S. H.; Gedanken, A. *Nano Letters* **2001**, *1*, 723.

(50) Zakrzewska, K.; Radecka, M.; Rekas, M. *Thin Solid Films* **1997**, *310*, 161.

(51) Themlin, J. M.; Chtaib, M.; Henrard, L.; Lambin, P.; Darville, J.; Gilles, J. M. *Physical Review B* **1992**, *46*, 2460.

(52) Egdell, R. G.; Eriksen, S.; Flavell, W. R. *Solid State Communications* **1986**, *60*, 835.

(53) Themlin, J. M.; Sporken, R.; Darville, J.; Caudano, R.; Gilles, J. M.; Johnson, R. L. *Physical Review B* **1990**, *42*, 11914.

(54) Cox, P. A.; Egdell, R. G.; Harding, C.; Patterson, W. R.; Tavener, P. J. *Surface Science* **1982**, *123*, 179.

(55) Taverner, A. E.; Rayden, C.; Warren, S.; Gulino, A.; Cox, P. A.; Egdell, R. G. *Physical Review B* **1995**, *51*, 6833.

(56) Vurgaftman, I.; Meyer, J. R.; Ram-Mohan, L. R. *Journal of Applied Physics* **2001**, *89*, 5815.

(57) Fan, X. F.; Sun, H. D.; Shen, Z. X.; Kuo, J. L.; Lu, Y. M. *Journal of Physics-Condensed Matter* **2008**, *20*, 235221.

(58) Nakhmedov, E. P.; Nadimi, E.; Bouhassoune, M.; Radehaus, C.; Wieczorek, K. *Physical Review B* **2007**, *75*, *115204*.

(59) Tit, N.; Obaidat, I. M.; Alawadhi, H. *Journal of Computational and Theoretical Nanoscience* **2009**, *6*, 1646.

Chapter 7 Electronic properties of high area Sn-doped rutile TiO_2 photocatalysts

7.1 Introduction

In current research on photocatalysis, cation doping in TiO_2 is a well-established approach to increase visible light absorption for potential use of TiO_2-based materials as visible light photocatalysts.[1] Transition metal dopants including the group 5 elements V [2], Nb [3] and Ta[3] as well as first row elements such as Cr [4], Fe [4] and Ni [3] have all been shown to promote intense visible light absorption, which is originated from new states within the bandgap of TiO_2.[5] However, paramagnetic species may decrease the photocatalytic activity since they act as electron/hole trapping sites or as recombination centres.[1] Theoretical work[6,7] as well as the experimental study reported in chapter 6 indicates that doping of an isovalent post-transition metal such as Sn into TiO_2 can also increase its visible light absortion, which suggests Sn-doped TiO_2 to be a potential visible region photocatalyst. A further advantage of post-transition metal doping is that, unlike transition metals, post-transition metals do not have a propensity to form less paramagnetic species.

Chapter 6 reported an experimental study of the electronic properties of $Sn_xTi_{1-x}O_2$ solid solutions. Samples were prepared by conventional high temperature solid state synthetic procedure for x values in the range $0 < x < 0.10$. In qualitative agreement with Long et al.[7] it was found a small decrease in the bandgap at very low doping levels, followed by an increase toward the value obtained by interpolation between the limits for TiO_2 and SnO_2 when $x > 0.02$. Additionally, for all samples a weak but extended

visible light absorption up to photon energy of 2eV was observed and associated to the presence of Sn^{2+}. These observations suggest Sn-doping in TiO_2 to be a potential means of bringing about photocatalysis in visible region. Samples studied in chapter 6 were however of little value as photocatalysts owing to their low surface area.

In the present chapter the properties of high surface area $Sn_xTi_{1-x}O_2$ prepared by a sol-gel route are investigated. It is found that even small levels of Sn doping promotes the anatase to rutile phase transition at much lower temperature than is found for undoped material. At the same time Sn doping inhibits sintering of the rutile phase, allowing for the preparation of Sn-doped rutile TiO_2 photocatalysts whose activity compares favourably with that of the more widely studies N-doped anatase TiO_2 studied in chapter 4. A further advantage may be that cation doped systems such as $Sn_xTi_{1-x}O_2$ are likely to prove more durable than anion doped systems with respect to loss of dopant during extended exposure to aqueous solutions in sunlight.

7.2 Experimental Section

7.2.1 Samples preparation

A range of sol-gel synthetic conditions have been proposed for the preparation of $Sn_xTi_{1-x}O_2$ solid solutions.[8-10] The basic strategy is the co-precipitation of Sn(VI) and Ti(IV) hydroxide from by hydrolysis of Sn and Ti compounds easily hydrolysable such as alcohoxide or chlorides followed by a thermal annealing process for crystallization of the material. For the study presented in this Sn-doped TiO_2 was prepared by a sol gel route using alkoxide precursors. Titanium (IV) isopropoxide (Aldrich, 97%) and an appropriate volume of tin (IV) tert-butoxide (Aldrich, 99.99%) were dissolved in isopropanol (Funka, analytical grade) to give 30 cm^3 of a solution with 0.5 M Ti

concentration. The resulting solution was acidified using HNO_3 (HNO_3/Ti molar ratio 0.15) and then hydrolysed with 10 cm^3 of distilled water. The resulting powder suspension was digested for 20 h and then dried at 70 °C. The amorphous material obtained in this way was calcined in air at temperatures ranging from 400°C to 700°C.

7.2.2 Characterization

Powder X-ray diffraction (XRD) patterns were measured on a Panalytical X'Pert Pro instrument using monochromated Cu $K\alpha_1$ radiation. High resolution X-ray photoemission spectra (XPS) were recorded on a Scienta ESCA 300 spectrometer located at Daresbury Laboratory, UK. This incorporated a rotating anode Al K_α ($h\nu$ =1486.6 eV) X-ray source, a seven crystal X-ray monochromator, a 300 mm mean radius spherical sector electron energy analyser and a parallel electron detection system. The X-ray source was run with 200 mA emission current and 14 kV anode bias, while the analyzer operated at 150 eV pass energy with 0.8 mm slits. Gaussian convolution of the analyzer resolution with a linewidth of 260 meV for the monochromated X-ray source gives an effective instrument resolution of 400 meV. Powder samples were prepared for XPS analysis by pressing into carbon tape. Photoelectron spectra were charge calibrated relative to the weak C 1s contaminant peak which was assigned a binding energy of 284.6 eV. Diffuse reflectance (DR) spectra were measured in the visible and near ultraviolet (UV) region using a Perkin Elmer Lambda 750S instrument incorporating a 6 cm integrating sphere.

7.2.3 Photocatalytic tests

The photocatalytic activity was evaluated by monitoring the photo-mineralisation of an aerated aqueous solution of methylene blue[11] with a concentration of 10 ppm. This

simple method of assessing photoactivity has proved a very popular and convenient method for screening catalysts[12-16]. A 150 W Xe lamp was used as the radiation source. The short wavelength components of the lamp output were removed using optical filters with cutoffs at $\lambda < 395$ nm ($h\nu > 3.14$ eV), $\lambda < 400$ nm ($h\nu > 3.10$ eV) and $\lambda < 420$nm ($h\nu > 2.95$ eV). In a typical photocatalytic experiment, a total of 40 mg of catalyst powder was added to 40 cm^3 of the methylene blue solution in a borosilicate tube. Prior to irradiation, the suspensions were magnetically stirred in the dark for 60 minutes to ensure the establishment of equilibrium coverage of the catalyst powder by the dye. At measured time intervals, aliquots of around 3 cm^3 were extracted and filtered through a 0.20 μm membrane filter to remove the catalyst particles. The filtrates were analyzed by recording variations in the absorbance at 665 nm (the peak maximum in the absorption spectra) in a Libra S6 Visible Spectrophotometer relative to the initial reading. The percentage of methylene blue degradation was plotted against the time of irradiation to provide a quantitative indication of the activity of the catalyst. Dye degradation tests were also carried out using a similar procedure but with a 10 ppm solution of methyl orange[17,18]. The concentration of this dye was monitored using the absorption peak at 480 nm. This dye underwent photodecomposition at a lower rate than methylene blue and experiments were conducted using the output of a 300 W solar simulator lamp with a 400 nm cutoff filter.

7.3 Results and discussion

7.3.1 Influence of tin on the rutile to anatase phase transition and powder particle size

Figure 7.1 shows X-ray diffraction (XRD) patterns of $Sn_xTi_{1-x}O_2$ solid solutions over the range of concentrations studied calcined at temperatures of 400 °C, 600 °C and 700

°C for 1 hour. After calcination at 400 °C most of the broad diffraction peaks observed in XRD could be indexed as belonging to the anatase phase. Peaks with 2θ values of 27.4° and 36.0° in the powder patterns of Sn-doped samples shown in figure 7.1a could however be assigned respectively to the (110) and (101) reflections of rutile. For all samples calcined at 400 °C, an additional weak XRD peak appears with a 2θ value of about 30.5°. This is associated with the brookite phase of TiO_2. The appearance of brookite TiO_2 has been reported in other preparation methods for $Sn_xTi_{1-x}O_2$ solid solutions[19] and W-Ti mixed oxides.[20] However, there is no sign of brookite for samples calcined at higher temperatures. As seen in figure 7.1b, upon increasing the calcination temperature to 600 °C all of doped samples undergo "rutilization" to give rutile TiO_2 as the predominant polymorph, but for the undoped sample the extent of conversion to the rutile phase remains quite small. Finally figure 7.1c shows XRD patterns for samples calcined at 700°C. It can be seen that the undoped sample is now converted into rutile as the majority phase whilst for 5% and 10% Sn doped samples conversion to rutile is complete. The promotion of the anatase to rutile phase conversion at lower temperatures than is found for undoped samples has been noted before and attributed to Sn incorporation into the TiO_2 lattice.[8,21,22] As discussed previously in chapter 6, SnO_2 adopts the same structure as the rutile polymorph of the TiO_2, but does not form an anatase phase. Thus it seems reasonable that Sn doping promotes the anatase-to-rutile conversion at lower temperatures in $Sn_xTi_{1-x}O_2$ solid solutions than in pure TiO_2 itself.

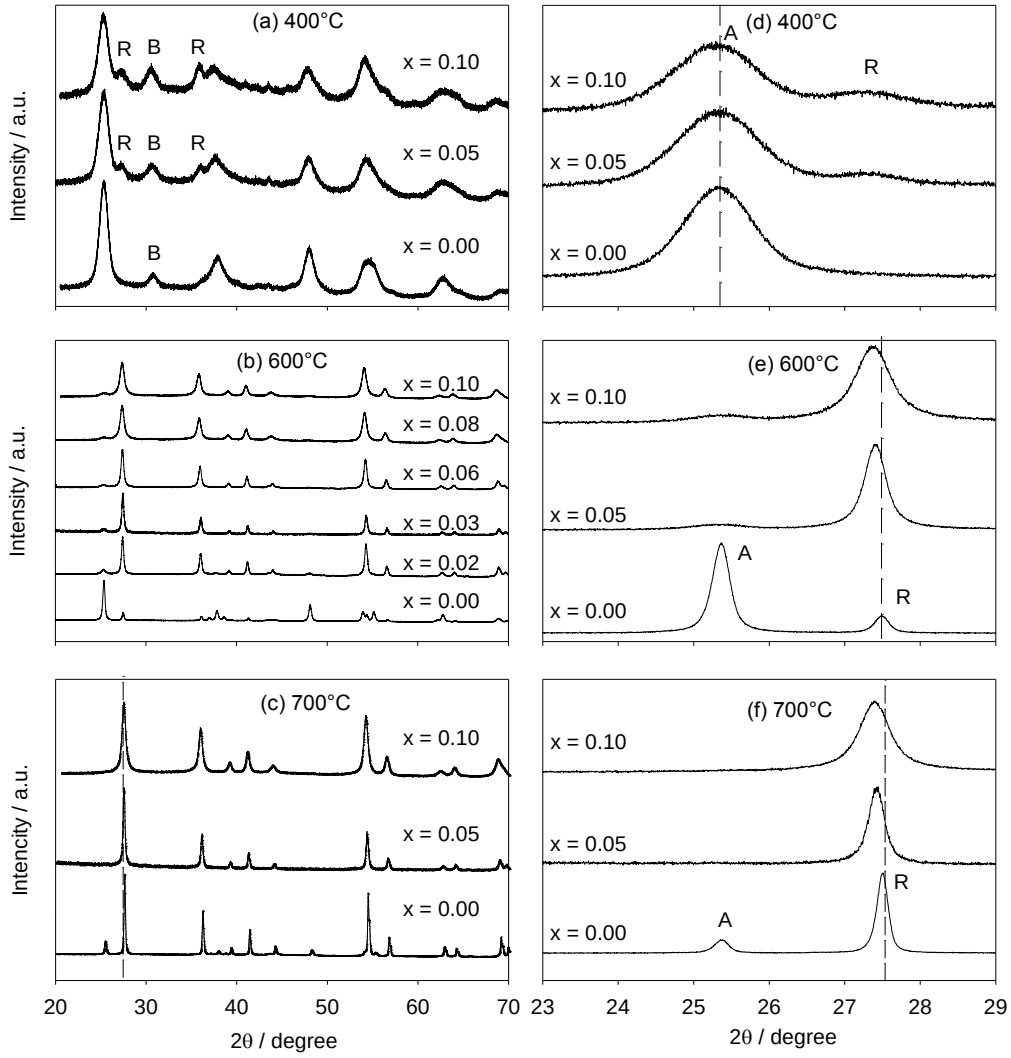


Figure 7.1 XRD patterns for Sn-doped TiO_2 samples prepared by a sol gel route sintered for 1 hour. Panels (a), (b) and (c) show wide scan patterns for samples annealed at 400°C, 600°C and 700°C respectively. R, A and B label peaks associated with rutile, anatase and brookite polymorphs. Panels (d), (e) and (f) show expansions which include the rutile (110) and anatase (101) reflections.

A shift of the diffraction peaks of the rutile phase toward lower 2θ angles was observed in the XRD pattern of doped samples that increased with Sn concentration. This arises from the fact that the lattice parameters of rutile-SnO_2 are bigger than those of rutile-TiO_2. Thus Sn incorporation onto Ti sites leads to an expansion of the TiO_2 unit cell.[23-25] As shown in figure 7.2 the *a* and *c* lattice parameters of the rutile phase increase monotonically as the Sn doping level increases, with a small positive deviation from a

simple Vegard interpolation as it was also found for samples made by solid state means studied in chapter 6. It is of interest to note that no such shift was seen for the anatase (101) XRD peaks (see figure 7.1). This suggests that there is very limited Sn incorporation into the anatase phase.

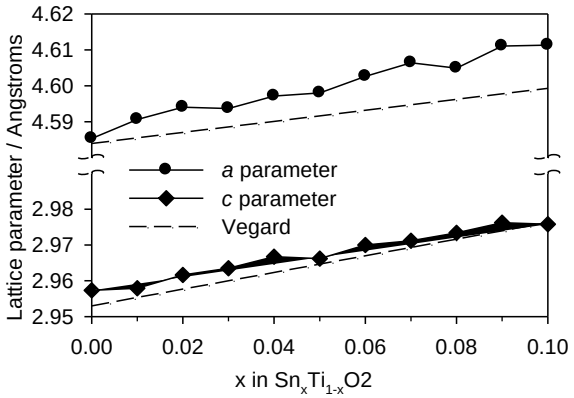


Figure 7.2 Lattice parameters for the rutile phase in $Sn_xTi_{1-x}O_2$ sintered at 600°C as function of Sn doping level x. The dashed lines show interpolations based on a Vegard relationship.

In figure 7.1 it can also be seen that for samples calcined at 600 °C at 700 °C the diffraction peaks of doped samples are broader than those seen in the undoped sample. This indicates that the doped samples have smaller crystallite size. From the measured width of the rutile (110) peak crystallite sizes were estimated by means of the Scherrer equation.

$$D = \frac{k\lambda}{\beta cos\theta}$$

Here D is the average crystallite size in Angstroms; k is a constant which is taken as 0.89; λ is the wavelength of the X-ray radiation ($CuK\alpha_1$, λ = 1.5406 Å); θ is the Bragg angle of the diffraction peak; and β is the corrected broadening, obtained after quadratic subtraction of instrument broadening, using the (110) peak of a well-sintered

sample of rutile TiO_2 with a particle size greater than 2 µm as the standard. The results of this analysis are shown in figure 7.3. As expected the higher the calcination temperature the smaller the particle size. There is also a good inverse correlation between the crystallite size and the Sn content for all samples at both the higher calcination temperatures. These observations suggest that the Sn incorporation reduces the sintering of the rutile crystallites in the $Sn_xTi_{1-x}O_2$ solid solutions.

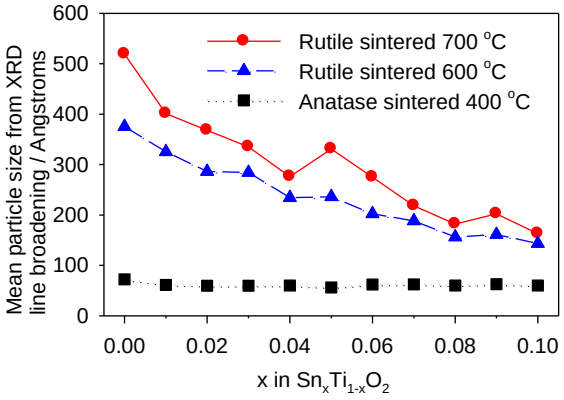


Figure 7.3 Mean particle size based on XRD line broadening for $Sn_xTi_{1-x}O_2$ samples as a function of Sn doping level x.

The specific surface area (SSA) of some selected solid solution samples as determined by BET analysis are shown in table 7.1. It can be seen that there is a pronounced increase in the SSA upon Sn doping which correlates with the decrease in the particle size inferred from XRD line broadening. Moreover, the reduction in SSA brought about by a higher calcination temperature is smaller for the solid solutions with higher Sn concentration. Taken together these results demonstrate that Sn doping inhibits the sintering of $Sn_xTi_{1-x}O_2$ solid solutions as compared with undoped TiO_2.

Table 1. Crystallite size and BET surface area for Sn-doped TiO_2 catalysts as a function of x in $Sn_xTi_{1-x}O_2$ and calcination temperature for selected samples.

Nominal value of x	Crystallite size[a] (Å)			Surface area[b] (m^2/g)	
	400°C	600°C	700°C	600°C	700°C
0.00	72	369	519	2.01	1.47
0.05	60	237	329	45.83	18.96
0.10	60	143	164	47.06	32.00

[a]Calculated by applying the Scherrer formula for line broadening to the rutile (110) diffraction peak.
[b] BET surface area calculated from the linear part of the BET plot (P/P_0=0.1–0.3).

7.3.2 Sn concentrations on $Sn_xTi_{1-x}O_2$ surfaces

Figure 7.4 shows an X-ray photoemission spectrum of a typical powder sample in the region of the Ti 2p and Sn 3d core levels. The Sn 3d core lines appear quite strong relative to the Ti 2p core peaks even in a sample with 6% Sn doping owing to the relatively high value for the cross section for ionisation of Sn 3d electrons as compared with the Ti 2p cross section. From spectra of this sort the apparent surface Sn 3d concentration as probed by XPS was determined by correction of core line intensities by atomic sensitivity factors[26]. In all cases the apparent Sn surface concentration was bigger than the nominal bulk value. Figure 7.5 shows the surface enrichment factor (defined as the apparent value of x in $Sn_xTi_{1-x}O_2$ determined by XPS divided by the bulk value of x) as a function of bulk doping level. The enrichment is highest at low bulk doping levels and falls off in a manner suggestive of saturation of surface sites with segregated dopant at higher doping levels.

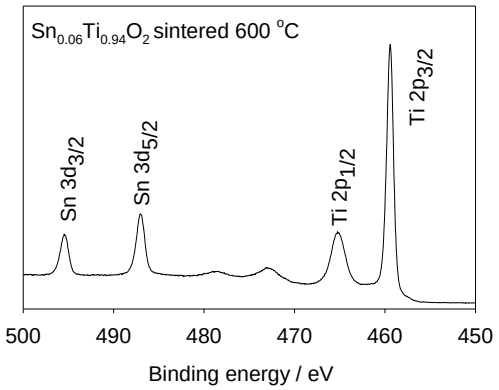


Figure 7.4 XPS data for 6% Sn-doped TiO_2 sintered at 600°C in region of Ti 2p and Sn 3d core lines.

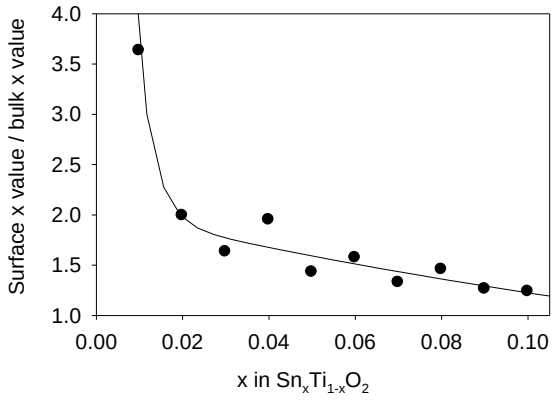


Figure 7.5 Surface enrichment ratio for Sn-doped TiO_2 samples sintered at 600°C defined as the apparent surface value of x in $Sn_xTi_{1-x}O_2$ determined by XPS divided by the corresponding bulk value. The solid line provides a guide to the trend observed.

Dopant surface segregation has been seen in other systems where a post transition metal ion dopant is introduced into an oxide host lattice. Systems studied include Sb-doped SnO_2,[27-29] Sb-doped TiO_2,[30] Sn-doped In_2O_3 ceramics[31] and thin films[32,33] as well as $Sn_xTi_{1-x}O_2$ solid solutions reported in chapter 6 in this thesis. Segregation in these systems has been attributed to the preference of post transition metal ions in the *N*-2 oxidation state to occupy surface sites, where *N* refers to the group oxidation state. Free ions in the *N*-2 oxidation state such as Sn^{2+} and Sb^{3+} have a configuration $5s^25p^0$. In solid state oxides, the 5s electrons hybridise strongly with O 2*p* states to give

antibonding states of mixed metal 5*s*-O 2*p* character at the top of the valence band. These states can further interact with nominally empty metal 5*p* states to give a directional electron lone pair provided that the cation occupies a site which lacks inversion symmetry. [34-36]. Bulk sites within the rutile structure are centrosymmetric but the lowered coordination at surface sites removes the inversion symmetry, thereby allowing 5*s*-5*p* hybridisation and a lowering of the internal electronic energy of the dopant ion. Thus segregation and reduction of bulk ions in the *N* oxidation state to give surface ions in the *N*-2 oxidation state lowers the surface energy and provides a thermodynamic driving force for segregation. At the same time, the lowering of the surface energy inhibits sintering of the Sn-doped TiO_2: obviously sintering will reduce the number of surface sites available for occupation by Sn(II).

7.3.3 The influence of Sn doping on electronic structure

(a) Valence band XPS

Valence band and shallow core level photoemission spectra of undoped rutile TiO_2 and of a series of Sn-doped samples sintered at 600 °C are shown in figure 7.6a. Similar to spectra of solid state samples in chapter 6, the intensity of the shallow core Sn 4*d* level increases monotonically with Sn doping level, mimicking the increase in intensity of the deeper Sn 3*d* core level. A second weaker peak at the bottom of the valence band (binding energy 10.5 eV relative to the Fermi energy) also grows in intensity with Sn doping, as seen in figure 7.6b. By reference to photoemission spectra of SnO_2 itself this peak is identified as being associated with states with pronounced Sn 5*s* character, hybridised with O 2*p* states.[27,37,38] Although in the ionic limit Sn^{4+} has an electron configuration $5s^0 5p^0$, SnO_2 is highly covalent with strong mixing between occupied O 2*p* states and nominally empty Sn 5*s* states, introducing Sn 5*s* character toward the

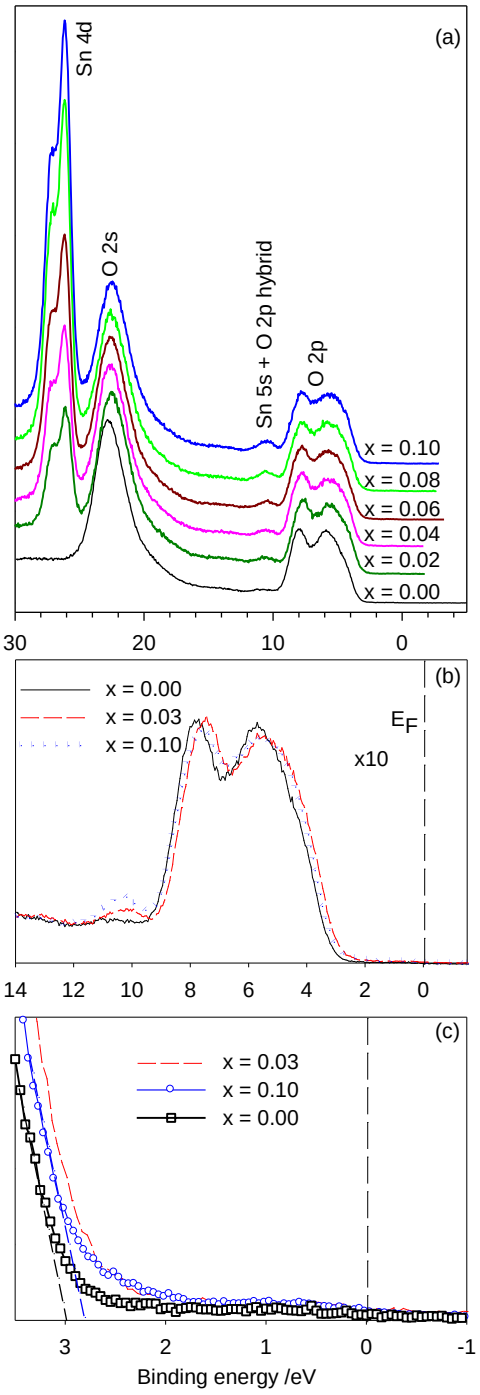


Figure 7.6 (a) Valence band and shallow core x-ray photoemission spectra of rutile TiO_2 and and Sn doped samples of $Sn_xTi_{1-x}O_2$ (where x = 0.02,0.04,0.06, 0.080 and 0.10) sintered at 600°C. (b) Expanded view of valence band region for undoped TiO_2, $Sn_{0.03}Ti_{0.97}O_2$ and $Sn_{0.10}Ti_{0.90}O_2$. (c) Further expanded view of valence band edge and bandgap regions for undoped TiO_2, $Sn_{0.03}Ti_{0.97}O_2$ and $Sn_{0.10}Ti_{0.90}O_2$.

bottom of the valence band. Similar states in Sn-doped In_2O_3 have been shown recently to have pronounced Sn 5*s* character on the basis of enhanced intensity in hard x-ray photoemission spectra[39].

More subtle changes are evident at the top of the valence band: these are most obvious when making a comparison between undoped TiO_2, $Sn_{0.03}Ti_{0.97}O_2$ and $Sn_{0.10}Tio_{0.90}O_2$ as in figure 7.6c. Firstly there is a small shift in the main valence band edge toward the Fermi energy. In agreement with the study on doped ceramic samples shown in chapter 6, this band edge shift reaches a maximum for doping levels around x = 0.02-0.03 and for higher doping levels the edge moves back toward the position found for undoped TiO_2. Secondly there is a small but noticeable increase in intensity above the top of the valence band, tailing into the lower part of the bandgap to about 2 eV binding energy. The tailing is more pronounced the higher the doping level and the higher the surface Sn concentration seen in XPS. This tail of states in the bandgap is attributed to surface states arising from Sn^{2+} ions in surface and grain boundary interface sites and the associated lone-pair like O 2*p* + Sn 5*s* + Sn 5*p* hybrid state discussed above.

(b) Diffuse reflectance spectra

Diffuse reflectance spectra of undoped TiO_2, $Sn_{0.03}Ti_{0.97}O_2$ and $Sn_{0.10}Ti_{0.90}O_2$ all sintered at 600 ºC are shown in figure 7.7(a) as plots of the Kubelka-Monk function F(R) versus photon energy hν. Expanded plots of $(F(R)h\nu)^2$ versus photon energy are shown in figure 7.7b. The absorption edge for undoped TiO_2 is found close to 3eV, as expected for the quoted value for the bulk bandgap. For the undoped sample, there is some indication of gradual rise in F(R) across the photon energy range between 2.6 eV and 1.6 eV. This is attributed to a low concentration of Ti^{3+} defect sites arising from oxygen deficiency. This absorption maximises in the near infrared at around 1 eV and

with higher levels of oxygen deficiency results in a characteristic blue colouration. The reflectance spectra of the Sn doped samples reveal a small shift in the main absorption edge to lower photon energy. The edge shift is bigger for the sample with x = 0.03 than for the more highly doped sample with x = 0.10. This is consistent with the valence band XPS data discussed above and the study of electronic properties of Sn-doped TiO_2 ceramics reported in chapter 6, as well as the density functional theory calculations of Long et al.[7]

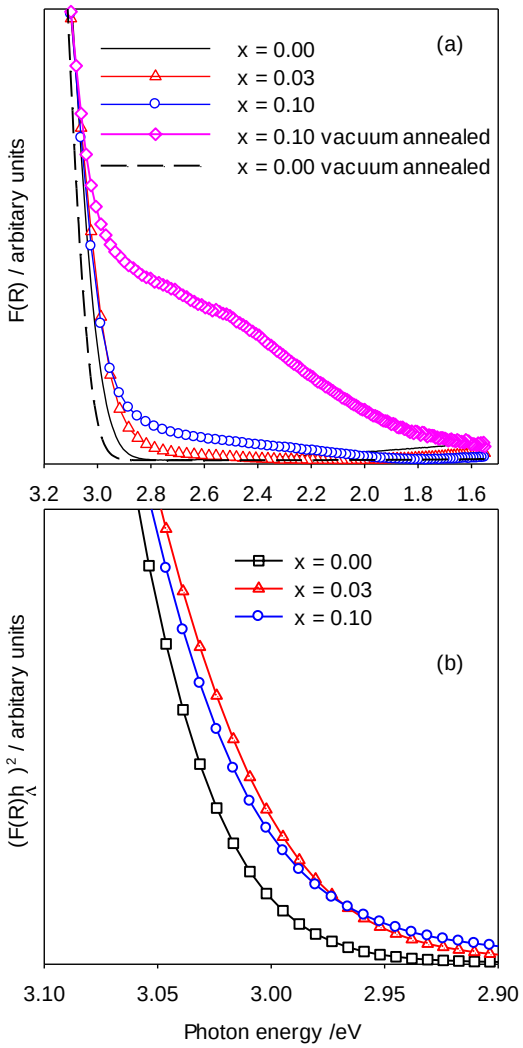


Figure 7.7 (a) Diffuse reflectance spectra of undoped rutile TiO_2, $Sn_{0.03}Ti_{0.97}O_2$ and $Sn_{0.10}Ti_{0.90}O_2$ sintered at 600 °C presented in terms of the Kubelka –Monk function F(R) versus photon energy. Data for rutile TiO_2 $Sn_{0.10}Ti_{0.90}O_2$ further annealed at 200 °C in vacuo are also shown. (b) Detail of optical absorption onsets for undoped rutile TiO_2, $Sn_{0.03}Ti_{0.97}O_2$ and $Sn_{0.10}Ti_{0.90}O_2$ presented in terms of plots of $(h\nu F(R))^2$ versus photon energy hν.

In addition the spectra reveal a weak tail of absorption extending across the visible region down to about 2 eV. This tail is most pronounced for $Sn_{0.10}Ti_{0.90}O_{2.}$ It is also notable that for this sample, the rise in F(R) toward the infrared end of the spectrum found for undoped TiO_2 is suppressed. The intensity of the absorption tail is strongly enhanced after annealing samples in vacuum at 200 °C whereas such annealing does not affect the undoped TiO_2 absorption, as shown for data relating to $Sn_{0.10}Ti_{0.90}O_2$ and undoped rutile included in figure 7.7a. In summary then, both valence band XPS measurements and diffuse reflectance spectra are consistent with a small narrowing of the bulk bandgap at low doping levels. The long weak absorption tail also accords with earlier chapter. This tail is associated with filled electronic states in the bottom half of the bulk bandgap observed in photoemission spectra of both SnO_2 and Sn-doped TiO_2 ceramic samples. These states arise from hybridised lone pairs arising from Sn^{2+} in bulk or grain boundary interface sites. These states lie deeper in the bulk band gap than states associated with electron self-trapped on Ti^{3+} sites. Thus Sn doping eliminates any possible paramagnetic $3d^1$ sites arising from a small level of oxygen deficiency. The concentration of reduced Sn^{2+} species increases on annealing in vacuum, which enhances the intensity of the absorption tail.

7.3.4 Photocatalytic activity of $Sn_xTi_{1-x}O_2$ solid solutions

Absorption spectra of methylene blue and methyl orange as used in dye degradation experiments are shown in figure 7.8, along with the data derived from a diffuse reflectance spectrum for a typical catalyst sample (3% Sn doped TiO_2 sintered at 600 °C). This figure also identifies the positions of the filters used to explore the spectral dependence of dye degradation. It should be noted that methylene blue has almost no

absorption around the position of the TiO_2 band edges, but methyl orange absorbs strongly in this region.

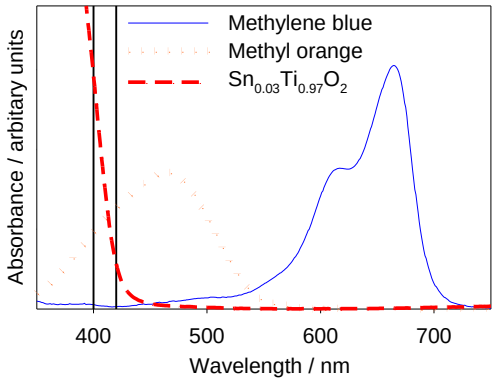


Figure 7.8 Optical absorption spectra of 10 ppm solutions of methylene blue and methyl orange along with band edge absorption for $Sn_{0.03}Ti_{0.98}O_2$ presented in terms of the Kubelka-Monk function. The positions of cutoff filters used in the present work are also indicated.

None of the samples sintered at 400 °C showed photocatalytic activity as gauged by degradation of methylene blue dye using 400 nm and 420 nm cutoff filters, although doped samples were active under irradiation with the unfiltered output of the Xe lamp or with a 395 nm filter. By contrast Sn-doped samples annealed at 600 °C were active in degradation of methylene blue dye even using the 420 nm filter, although undoped samples sintered at 600 °C and 700 °C were inactive under these conditions. The bandgap cutoff for undoped rutile is at 3.06 eV (405 nm) so these observations establish that photon absorption by the catalyst is critical to dye degradation. Some typical results from methylene blue degradation experiments are shown in figure 7.9a for samples of $Sn_{0.02}Ti_{0.98}O_2$ annealed at 400 °C and 600 °C. The samples sintered at 600 °C were more active than samples sintered at 700 °C, presumably owing their higher surface area.

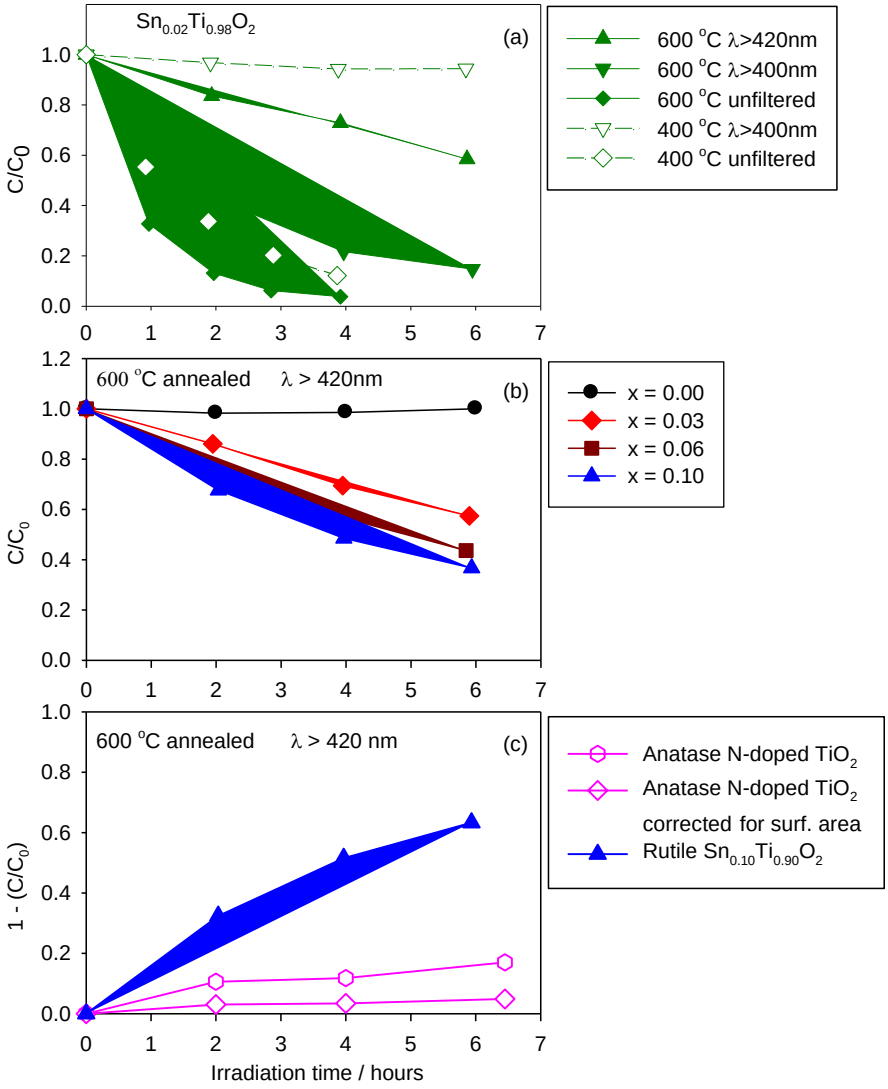


Figure 7.9 (a) Concentration C of methylene blue dye under irradiation with output of 150 W Xe lamp in presence of $Sn_{0.02}Ti_{0.98}O_2$ photocatalysts as compared with initial concentration of dye C_0 using filters with cutoffs at 400 nm and 420 nm as well as the unfiltered output of the lamp. The catalyst samples were all sintered at 400 °C and 600 °C for 1 hour.

(b) Concentration C of methylene blue dye under irradiation with filtered output (λ > 420 nm) of 150 W Xe lamp in presence of $Sn_xTi_{1-x}O_2$ photocatalysts as compared with initial concentration of dye C_0 for x=0.00, 0.03, 0.06 and 0.10. The catalyst samples were all sintered at 600 °C for 1 hour.

(c) Comparison of degree of degradation of methylene blue dye ($1-C/C_0$) under irradiation as above in presence of optimal N-doped anatase TiO_2 photocatalyst (from chapter 4) and 10% Sn doped catalyst (x = 0.10) sintered at 600 °C. A plot is also shown where the data for the anatase catalyst have been corrected to allow for the greater surface area.

Further results from methylene blue degradation experiments with a 420 nm filter using catalyst samples annealed at 600 °C for a series of different Sn doping levels are shown

in figure 7.9b. It was found that the catalytic activity increased with Sn doping level so that the sample with bulk composition $Sn_{0.10}Ti_{0.90}O_2$ was the most active. The activity of this sample was much greater than optimal nitrogen doped TiO_2 anatase samples studied in chapter 4, even though these samples are annealed at a much lower temperature of 380 °C and therefore have surface areas that are typically around a factor of three larger than the Sn-doped samples sintered at 600 °C. As shown in figure 7.9c, the superior performance of the Sn-doped catalyst is particularly striking when the data for the N-doped catalysts are corrected to allow for their greater surface area.

The pronounced dependence of the activity in dye degradation tests upon both the insertion of 400 nm and 420 nm cut off filters and the level of Sn doping argues strongly in favour of a mechanism for methylene blue dye degradation that involves photon generation of electron-hole pairs within the catalyst, with subsequent oxidation of the dye by holes. Clearly there are very strong variations in catalyst absorption around 400 nm that are influenced by Sn doping, whereas methylene blue does not absorb in this region. Thus the possible reaction of photoexcited methylene blue with the catalyst surface would not be changed by the insertion of 400 nm and 420 nm filters. This allows us to rule out a dominant "photosensitisation" mechanism for dye degradation involving photoexcitation in the dye followed by charge injection from the excited dye into the conduction band of the semiconductor catalyst[40,41].

As discussed above photo-degradation of methyl orange was generally slower than that of methylene blue and experiments using this dye were restricted to the most active catalysts. Some typical results are shown in figure 7.10 where the activity of $Sn_{0.10}Ti_{0.90}O_2$ sintered in air at 600 °C is compared with that of the same material after

sintering in vacuo at 200 °C. The vacuum treatment is seen to lead to enhanced photocatalytic activity.

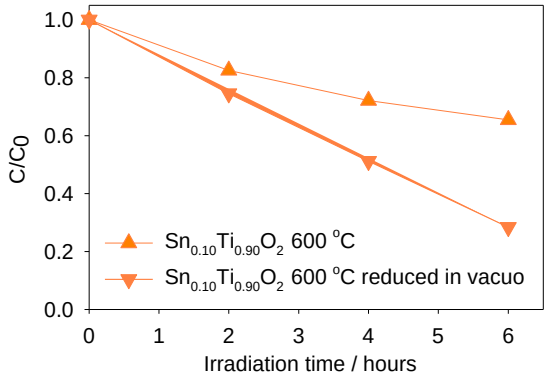


Figure 7.10 Concentration ratio C/C_0 of methyl orange dye under irradiation with filtered output (λ > 400 nm) of 300 W solar simulator lamp in presence of $Sn_{0.10}Ti_{0.90}O_2$ photocatalyst sintered at 600 °C for 1 hour in air compared with results for same catalyst after further annealing in vacuo at 200 °C.

7. 4 Conclusions.

The study carried out in this chapter establishes that Sn doping in TiO_2 not only promotes the transformation of high area anatase powders (prepared by a sol-gel route) into the rutile polymorph as previously reported, but also inhibits particle sintering. This allows preparation of high area powders of doped material with the rutile structure. Sn doping leads to a small shift in the position of the valence band edge and a small narrowing of the bulk bandgap, as gauged by valence band X-ray photoemission and diffuse reflectance spectroscopy. The band gap narrowing is most pronounced for doping levels around x-=0.02-0.03. In addition segregated Sn^{2+} ions residing at surface and grain boundary interfaces give rise to surface states above the top of the main valence band, leading to a tail of absorption seen in diffuse reflectance spectra extending down to about 2 eV. The intensity of this absorption increases with Sn doping level and is very strongly enhanced by annealing catalyst samples in vacuo.

Photoatalytic activity as gauged by the mineralisation of methylene blue or methyl orange dyes increases with Sn doping level and correlates with the intensity of visible region absorption associated with the Sn^{2+} surface states discussed above. Optimal Sn-doped rutile TiO_2 powders exhibit photocatalytic activity superior to that of N-doped TiO_2 with the anatase phase, even though the latter samples have a much larger surface area. It can be speculated that the enhanced photocatalytic activity in Sn doped material arises from efficient trapping of photogenerated holes on surface segregated Sn ions. This both inhibits electron hole pair recombination and localises holes in surface sites where they can participate in heterogeneous redox reactions. Thus Sn-doped TiO_2 shows considerable promise as a practical visible region photocatalyst.

7.5 References

(1) Ni, M.; Leung, M. K. H.; Leung, D. Y. C.; Sumathy, K. *Renewable & Sustainable Energy Reviews* **2007**, *11*, 401.

(2) Klosek, S.; Raftery, D. *Journal of Physical Chemistry B* **2001**, *105*, 2815.

(3) Niishiro, R.; Kato, H.; Kudo, A. *Physical Chemistry Chemical Physics* **2005**, *7*, 2241.

(4) Dholam, R.; Patel, N.; Adami, M.; Miotello, A. *International Journal of Hydrogen Energy* **2009**, *34*, 5337.

(5) Mizushima, K.; Tanaka, M.; Asai, A.; Iida, S.; Goodenough, J. B. *Journal of Physics and Chemistry of Solids* **1979**, *40*, 1129.

(6) Yu, X. H.; Li, C. S.; Tang, H.; Ling, Y.; Tang, T. A.; Wu, Q. O.; Kong, J. J. *Computational Materials Science* **2010**, *49*, 430.

(7) Long, R.; Dai, Y.; Huang, B. *Journal of Physical Chemistry C* **2009**, *113*, 650.

(8) Cao, Y. Q.; He, T.; Zhao, L. S.; Wang, E. J.; Yang, W. S.; Cao, Y. A. *Journal of Physical Chemistry C* **2009**, *113*, 18121.

(9) Jing, L. Q.; Fu, H. G.; Wang, B. Q.; Xin, B. F.; Li, S. D.; Sun, J. Z. *Applied Catalysis B-Environmental* **2006**, *62*, 282.

(10) Sui, R. H.; Young, J. L.; Berlinguette, C. P. *Journal of Materials Chemistry* **2010**, *20*, 498.

(11) Mills, A.; Wang, J. S. *Journal of Photochemistry and Photobiology a-Chemistry* **1999**, *127*, 123.

(12) Asahi, R.; Morikawa, T.; Ohwaki, T.; Aoki, K.; Taga, Y. *Science* **2001**, *293*, 269.

(13) Sathish, M.; Viswanathan, B.; Viswanath, R. P.; Gopinath, C. S. *Chemistry of Materials* **2005**, *17*, 6349.

(14) Livraghi, S.; Paganini, M. C.; Giamello, E.; Selloni, A.; Di Valentin, C.; Pacchioni, G. *Journal of the American Chemical Society* **2006**, *128*, 15666.

(15) Yang, W. D.; Lin, W. C.; Yang, C. H.; Chung, Z. J.; Huang, I. L. *Journal of Materials Research* **2009**, *24*, 2574.

(16) Livraghi, S.; Chierotti, M. R.; Giamello, E.; Magnacca, G.; Paganini, M. C.; Cappelletti, G.; Bianchi, C. L. *Journal of Physical Chemistry C* **2008**, *112*, 17244.

(17) Brown, G. T.; Darwent, J. R. *Journal of Physical Chemistry* **1984**, *88*, 4955.

(18) Song, X. M.; Wu, J. M.; Yan, M. *Thin Solid Films* **2009**, *517*, 4341.

(19) Fresno, F.; Tudela, D.; Coronado, J. M.; Soria, J. *Catalysis Today* **2009**, *143*, 230.

(20) Fernandez-Garcia, M.; Martinez-Arias, A.; Fuerte, A.; Conesa, J. C. *The Journal of Physical Chemistry B* **2005**, *109*, 6075.

(21) Fresno, F.; Coronado, J. A.; Tudela, D.; Soria, J. *Applied Catalysis B-Environmental* **2005**, *55*, 159.

(22) Fresno, F.; Tudela, D.; Coronado, J. M.; Fernandez-Garcia, M.; Hungria, A. B.; Soria, J. *Physical Chemistry Chemical Physics* **2006**, *8*, 2421.

(23) Hirata, T.; Ishioka, K.; Kitajima, M.; Doi, H. *Physical Review B* **1996**, *53*, 8442.

(24) Lin, J.; Yu, J. C.; Lo, D.; Lam, S. K. *Journal of Catalysis* **1999**, *183*, 368.

(25) Uchiyama, H.; Imai, H. *Chemical Communication* **2005**, 6014.

(26) *Practical Surface Analsysis*; Briggs, D.; Seah, M. P., Eds.; John Wiley: Chichester, 1994.

(27) Cox, P. A.; Egdell, R. G.; Harding, C.; Patterson, W. R.; Tavener, P. J. *Surface Science* **1982**, *123*, 179.

(28) Egdell, R. G.; Flavell, W. R.; Tavener, P. *J. Solid State Chem.* **1984**, *51*, 345.

(29) Cox, P. A.; Egdell, R. G.; Harding, C.; Orchard, A. F.; Patterson, W. R.; Tavener, P. J. *Solid State Communications* **1982**, *44*, 837.

(30) Gulino, A.; Condorelli, G. G.; Fragala, I.; Egdell, R. G. *Applied Surface Science* **1995**, *90*, 289.

(31) Cox, P. A.; Flavell, W. R.; Egdell, R. G. *J. Solid State Chem.* **1987**, *68*, 340.

(32) Bourlange, A.; Payne, D. J.; Palgrave, R. G.; Zhang, H.; Foord, J. S.; Egdell, R. G.; Jacobs, R. M. J.; Veal, T. D.; King, P. D. C.; McConville, C. F. *Journal of Applied Physics* **2009**, *106*.

(33) Morales, E. H.; Diebold, U. *Applied Physics Letters* **2009**, *95*.

(34) Payne, D. J.; Egdell, R. G.; Walsh, A.; Watson, G. W.; Guo, J.; Glans, P. A.; Learmonth, T.; Smith, K. E. *Phys. Rev. Lett.* **2006**, *96*, 157403.

(35) Walsh, A.; Watson, G. W. *J. Solid State Chem.* **2005**, *178*, 1422.

(36) Walsh, A.; Watson, G. W. *Phys. Rev. B* **2004**, *70*, 235114.

(37) Egdell, R. G.; Rebane, J.; Walker, T. J.; Law, D. S. L. *Phys. Rev. B* **1999**, *59*, 1792.

(38) Egdell, R. G.; Walker, T. J.; Beamson, G. *Journal of Electron Spectroscopy and Related Phenomena* **2003**, *128*, 59.

(39) Korber, C.; Krishnakumar, V.; Klein, A.; Panaccione, G.; Torelli, P.; Walsh, A.; Da Silva, J. L. F.; Wei, S. H.; Egdell, R. G.; Payne, D. J. *Physical Review B*, *81*.

(40) Vinodgopal, K.; Wynkoop, D. E.; Kamat, P. V. *Environmental Science & Technology* **1996**, *30*, 1660.

(41) Nasr, C.; Vinodgopal, K.; Fisher, L.; Hotchandani, S.; Chattopadhyay, A. K.; Kamat, P. V. *Journal of Physical Chemistry* **1996**, *100*, 8436.

Chapter 8: Structural and electronic properties of anatase $Sn_xTi_{1-x}O_2$ films epitaxially grown on $SrTiO_3$ (001)

8.1 Introduction

TiO_2 and SnO_2 both adopt the tetragonal rutile structure, although the lattice parameters for SnO_2 (a = 4.737 Å, c = 3.360 Å) are somewhat bigger than those for TiO_2 (a = 4.594 Å, c = 2.959 Å). As discussed in chapter 7, Sn doping in solid solution samples prepared by low temperature sol-gel as well as hydrothermal routes promotes the anatase-to-rutile phase transformation at much lower temperatures than in pure TiO_2.[1-4] However, of the various polymorphs of TiO_2, anatase shows the best ultraviolet photocatalytic activity, probably due to its high electron mobility which facilitates separation of electron-hole pairs.[5]

Mobility is strongly dependent on crystal quality as grain boundaries and defects act as scattering centres. The high crystallinity which can be found in epitaxially grown thin film may potentially enhance the photocatalytic performance of TiO_2. Epitaxial anatase TiO_2 thin films have been grown by a number of vacuum based techniques such as molecular beam epitaxy, RF sputtering and pulsed laser deposition.[6-8] While these synthesis methods are well-suited to basic research, large scale applications of such films are of limited potential due to the high cost of film growth. Epitaxial films of anatase TiO_2 have also been prepared by wet chemical methods based on hydrothermal and sol-gel synthesis. These approaches are far less expensive than the physical deposition methods discussed above and yet can provide high quality films.[9-11] $SrTiO_3$ (001) and $LaAlO_3$ (001) single crystals are ideal substrates for a preferential epitaxial

growth of anatase TiO_2 due to the smaller lattice mismatch between the anatase TiO_2 lattice *a* parameter and that of the substrates as compared with the mismatch with rutile. Using $SrTiO_3$ (001) (a = 3.905 Å) as the substrate, the lattice mismatch with an anatase (001) ($a = b$ = 3.784 Å, c = 9.514 Å) epilayer is about 3.1% whereas with rutile TiO_2 it is about 9%.[12]

This chapter deals with the preparation of epitaxial anatase $Sn_xTi_{1-x}O_2$ on $SrTiO_3$ (001) substrates by means of a simple sol-gel method. Anatase $Sn_xTi_{1-x}O_2$ films grow epitaxially on the substrate and retain the anatase structure for sintereing temperatures up to 900ºC and doping levels up to 15%. A study of the electronic structure of anatase Sn-doped TiO_2 by means of photoelectron spectroscopy reveals that the unlike rutile samples studied in the previous chapters, Sn doping in anatase TiO_2 leads to a monotonic increase of the band gap . Although an increase of the band gap is not helpful toward visible light photocatalysis, it was shown in the previous chapter that the visible light activity of rutile Sn-doped TiO_2 is mainly determined by electronic states associated with Sn(II) ions on the surface of the solid rather than reduction of the bulk bandgap. Therefore anatase $Sn_xTi_{1-x}O_2$ is of some interest as a potential catalytic material.

8.2 Experimental Section

8.2.1 Preparation of the films

Samples were prepared by a sol-gel method. Titanium (IV) isopropoxide (Aldrich, 97%) and an appropriate amount of tin (IV) tert-butoxide (Aldrich, 99.99%) were dissolved in isopropanol (Fischer Scientific, analytical grade) to give 25cm^3 of a

solution with 0.33 M Ti concentration, which was acidified using HNO_3 (HNO_3/Ti molar ratio 0.15). The resulting solution was used to dip coat $SrTiO_3$(001) substrates in a 25 cm^3 wide neck flask. The substrates were withdrawn from the alkoxide solution using a motor drive at a pulling rate of 3.5 mm/min. The impregnated substrates were immediately placed in flowing N_2 gas saturated with H_2O at room temperature, so that the mixed alkoxides were hydrolysed on the $SrTiO_3$(001) (STO(001)) surface. By varying the numbers of dip-hydrolysis cycles the thickness of the film could be controlled reproducibly. The amorphous film products of the hydrolysis were calcined at temperatures ranging from 700 °C up to 1000 °C to form epitaxial films of Sn-doped anatase TiO_2.

8.2.2 Characterization

X-ray Diffraction (XRD) was carried out on a Panalytical instrument using monochromated Cu $K_{\alpha 1}$ radiation. The sample was placed such that the film was just tangential to the focusing circle in the standard Bragg-Brentano geometry. The patterns were calibrated with the STO(001) reflection at 2θ = 46.472º. AFM images were recorded *ex situ* with a Digital Instruments Multimode SPM instrument. This was operated in contact mode with a 'J' scanner having a lateral range of approximately 100 μm and a vertical range of 6 μm. Silicon nitride probes (Nascatec GmbH model NST NCHFR), with a thin coating of gold to act as a mirror for the laser beam, were used. Calibration of the AFM was accomplished by scanning a 10 mm pitch 200 nm 3D reference from Digital Instruments. Digital Nanoscope software (version 5.12) was used to analyse and process the AFM topographic images. All the images were treated with the 'flatten' command and are presented using one of the standard colour palettes

of the Nanoscope software. Specimens for cross-sectional TEM were prepared by cutting and mechanical grinding down to 5–10 μm, followed by thinning to electron transparency by Ar ion beam milling using a Gatan 691 Precision Ion Polishing System (PIPS). Cross-sectional TEM images were collected using a JEOL3000F microscope operating at 300 keV. Digital Micrograph image software was used to process the TEM images. Bragg filtering was applied to the TEM images in order to remove some of the background noise and contrast adjustment was applied uniformly across the images where necessary to enhance the display quality. High-resolution X-ray photoemission spectra (XPS) were recorded in a Scienta ESCA 300 spectrometer located at Daresbury Laboratory, UK, which incorporated a rotating anode Al K_α ($h\nu$ =1486.6 eV) X-ray source. The X-ray source was run with 200 mA emission current and 14 kV anode bias, whereas the analyzer operated at 150 eV pass energy with 0.8 mm slits. Gaussian convolution of the analyzer resolution with a linewidth of 260 meV for the monochromated X-ray source gives an effective instrument resolution of 450 meV.

8.3 Results and discussion

8.3.1 Epitaxial growth of undoped TiO_2 by sol-gel routes

Figure 8.1 shows 5 μm x 5 μm AFM images of an undoped TiO_2 sample obtained after 2 dip/hydrolysis cycles and calcination at 700 °C and 1000 °C. After calcination at 700 °C a rough but continuous film was obtained. However, the film broke upon further annealing at 1000 °C to form a striking array of square edged box-like structures with a fairly small size distribution. From the known bulk crystallographic directions of the substrate it may be inferred that square particles are all oriented with edges parallel to the [100] and [010] directions of the $SrTiO_3$ substrate. Analysis of the AFM images

indicate the square-shaped structures have an average height of approximately 15 nm and edge length of around 150 nm. These observations indicate that the originally flat film suffered a dewetting process upon high temperature annealing that led to the formation of self-assambled array of square-shaped nanoislands. M. Coll et.al.[13] reported a similar dewetting process for (001) heteroepitaxial $YBa_2Cu_3O_7$ films, grown from trifluoroacetate precursors on $SrTiO_3$(001) and $LaAlO_3$ (001). These authors proposed the process to be a consequence of the relaxation of strain due to the lattice mismatch with the substrates. The sample initially grows in a metastable continuous film that breaks down as soon as kinetic barriers to dewetting can be overcome. Strain due to lattice mismatch has also been assigned as the cause of dewetting process in molecular systems.[14,15] The molecule 3,4,9,10-perylene tetracarboxylic dianhydride (PTCDA) deposited on NaCl(001) surfaces grows as monolayer islands with a p3x3 epitaxy at low coverage, which partially break into bulk-like crystallites at higher coverage. Calculations show the p3x3 epitaxy to be incompatible with a multilayer crystal of PTCDA. Consequently, the growth of additional layers results in an adaptation of the interface structure forcing a dewetting transition.[14]

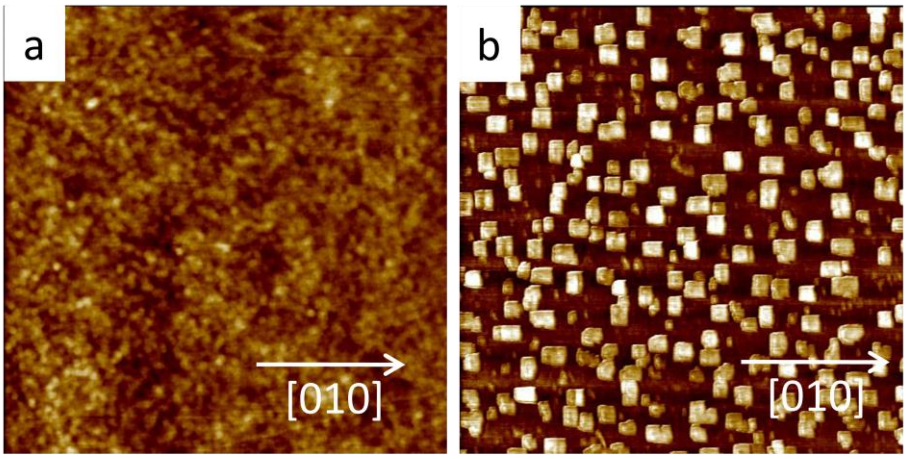


Figure 8.1. 5 μm x 5 μm AFM images of undoped TiO_2 sample obtained after two dip-hydrolysis cycles calcined at (a) 700°C and (b) 1000ºC.

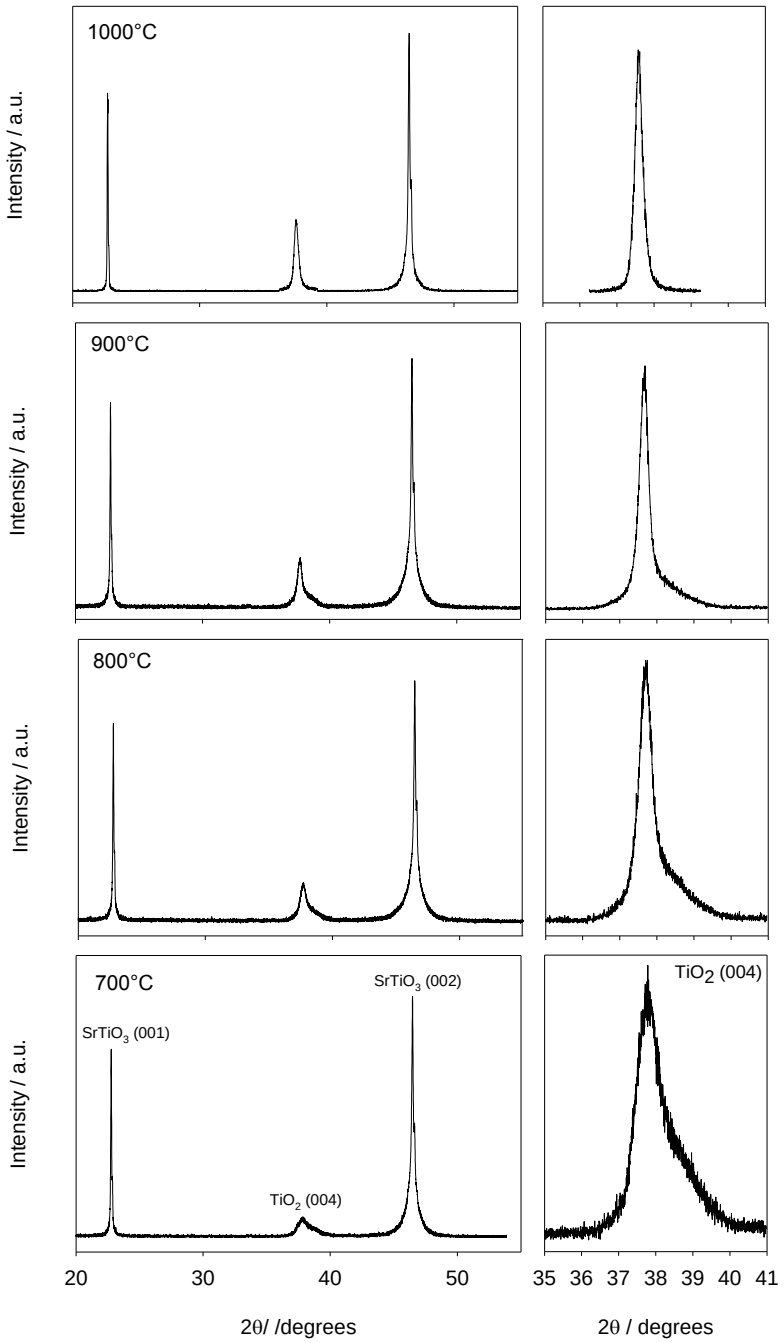


Figure 8.2. Out-of-plane XRD pattern of a TiO_2 film obtained after two dip-hydrolysis cycles calcined at temperatures from 700°C to 1000ºC. Intensities in XRD patterns in this chapter are presented on a logarithmic scale.

Figure 8.2 shows the out of plane XRD patterns of the films calcined between 700°C

and 1000 °C. Aside from the $SrTiO_3$(001) and $SrTiO_3$(002) reflections from the substrate, the only diffraction peak can be seen in the pattern is the only the anatase (004)peak. This indicates crystal growth with the anatase c axis normal to the substrate surface, so that film and substrate have the epitaxial relationship:

$$(001)_{TiO_2} \,||\, (001)_{STO}$$

Detail of the anatase (004) XRD peak are shown in the right hand side panels of figure 8.2. It can be seen that for samples calcined at lower temperatures the anatase (004) diffraction peak shows strong asymmetry that gradually disappears as the sample is annealed at higher temperatures. It can also be seen in figure 8.2 that there is a continuous shift towards lower Bragg angle upon increasing the annealing temperature. From the measured anatase (004) XRD peak position, the out-of-plane *d*-spacing (d_{001}) was calculated and plotted versus annealing temperature as shown in figure 8.3.

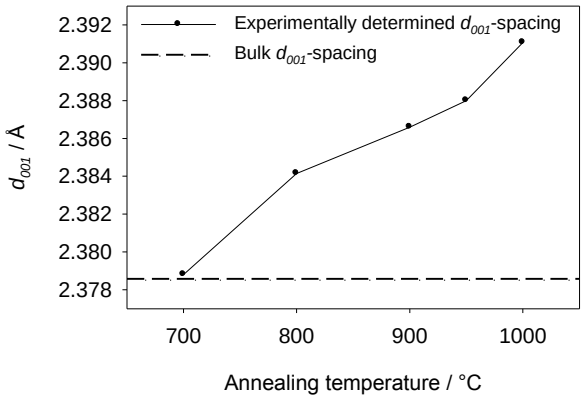


Figure 8.3. Experimentally determined d_{001}-spacing of anatase TiO_2 film obtained after two dip-hydrolysis in the range of annealing temperature 700°C to 1000°C.

There is a monotonic increase of d_{001} upon increasing the annealing temperature, tending to a constant value at high temperature. The change in *d* spacing has an unusual behaviour. In principle, it could be explained on the basis that the TiO_2 film is placed

under tensile stress due to the 3.1% mismatch between the STO substrate and the TiO_2 epilayer, which is released as the system approaches a thermodynamic regimen at higher temperatures. Tensile stress gives rise to a lateral expansion (in-plane), which in turn leads to a decrease in the interatomic separations normal to the surface from its relaxed value. In this case however the d_{001} for samples is larger than that found in free standing powders, whose value is also indicated in figure 8.3. This observation has been reported in previous wet chemistry preparations of TiO_2 heteroepitaxial films on $LaAlO_3$ and $SrTiO_3$ substrates.[9-11] Jung et.al. suggested the strain relaxation consequent upon higher temperature annealing is due to the incorporation of oxygen and the concomitant annihilation of oxygen vacancies. However, strain due to oxygen vacancy seems unlikely to be the origin of this behaviour since surface chemical analysis of continuous films (XPS spectrum free from Sr signals) by means of XPS show that the Ti:O ratio is 1:2 regardless of the annealing temperature. A more detailed study that includes direct determination of in-plane lattice parameters is needed to settle this issue.

Figure 8.4 shows a cross sectional HRTEM image of an undoped TiO_2 film (2 dips) after annealing at 1000 °C. The image confirms that the sample has grown with the anatase (001) axis normal to the substrate surface. The image also reveals a reasonably sharp interface and lateral registry so that:

$$(001)_{TiO_2} \,||\, (001)_{STO}$$

$$(010)_{TiO_2} \,||\, (010)_{STO}$$

The top surface of the anatase island is parallel to the susbtrate and is of (001) orientation. However there are well developed sloping side facets which may be identified as supporting (103) surfaces. In a study of anatase (001) surface reconstructions, Herman et.al.[16] found that the (1 × 1) surface reconstructs into a two-

domain (1 × 4) microfaceted surface upon sputtering and annealing. This surface exposes both (103) and ($\bar{1}$03) facets. Microfacets with (103) surfaces have been also reported to be present on (001) surfaces of anatase nanocrystals.[17] It is interesting to note therefore that facets on anatase (001) are dominated by {103} surfaces rather than {101} surfaces, which are generally presumed to have a lower surface energy.[18,19]

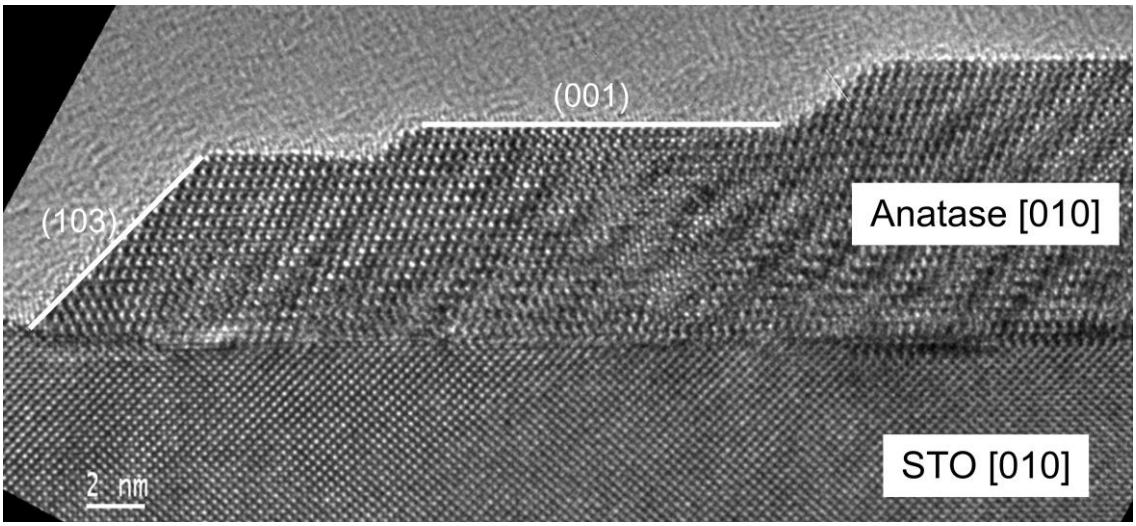


Figure 8.4. Cross sectional HRTEM image of an individual island down the [010] crystal direction of the substrate.

The epitaxial relationship between the anatase TiO_2 islands and the substrate is confirmed by selected area electron diffraction carried out in the HRTEM. Figure 8.5 shows electron diffraction patterns from a slice of the sample taken down the [010] direction for both the $SrTiO_3$ (figure 8.5a) and for the TiO_2 epilayer (figure 8.5b). The diffraction patterns firmly establish the azimuthal orientation of the islands relative to the substrate, which clearly confirms an in-plane epitaxial relationship between film and substrate

$$[100]_{TiO_2} \,||\, [100]_{STO}.$$

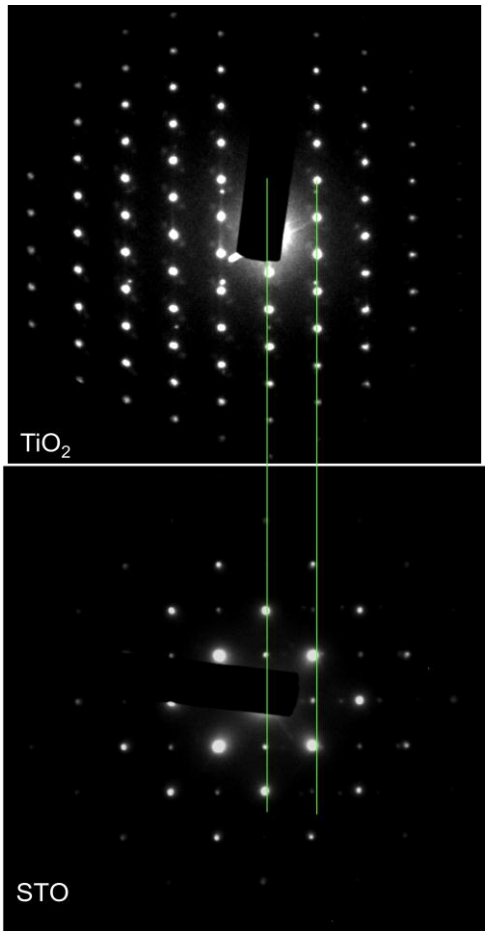


Figure 8.5. Selected area electron diffraction patterns from the TiO_2 epilayer down [010] direction (top) and from the $SrTiO_3$ substrate down [010] direction (bottom).

Figure 8.6 shows a 5 μm x 5 μm AFM images of a sample obtained after 8 cycles of dipping / hydrolysis and calcination at 1000°C. Similar to the thinner films, square-shaped nanostructures with edges parallel to [100] and [010] crystal directions of the substrate are found. This may be related to the existence of an in-plane epitaxial relationship the same as that found for the thinner films

$$[100]_{TiO_2} \,||\, [100]_{STO}.$$

However, no complete dewetting of the surface of the substrate was observed for this film. The greater thickness stabilises the formation of a continuous film although both films have the same lattice mismatch with the substrate. Based on a free energy analysis, Coll *et al.* have developed a model which shows that for a given interfacial energy above a critical film thickness a discontinuous dewetted film structure is less stable than the continuous film structure.[13]

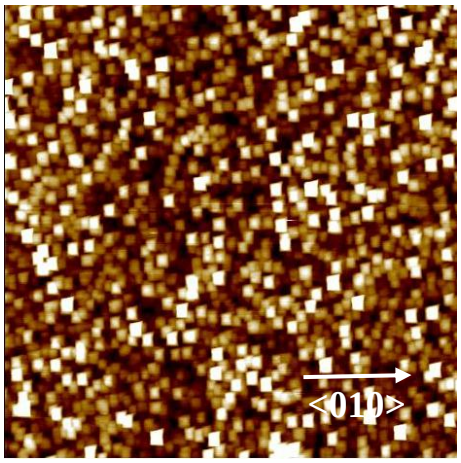


Figure 8.6. 5 μm x 5 μm AFM image of a TiO_2 film calcined at 1000ºC.

Figure 8.7a shows the out-of-plane X-ray diffraction pattern of a TiO_2 film calcined at 1000°C. As with the thinner nanoisland film, aside from the STO (001) and STO (002) reflections from the substrate, only the anatase (004) diffraction peak can be seen in the pattern.This indicates exclusive crystal growth along the c axis direction so that film and substrate have the epitaxial relationship

$$(001)_{TiO_2} \,||\, (001)_{STO}.$$

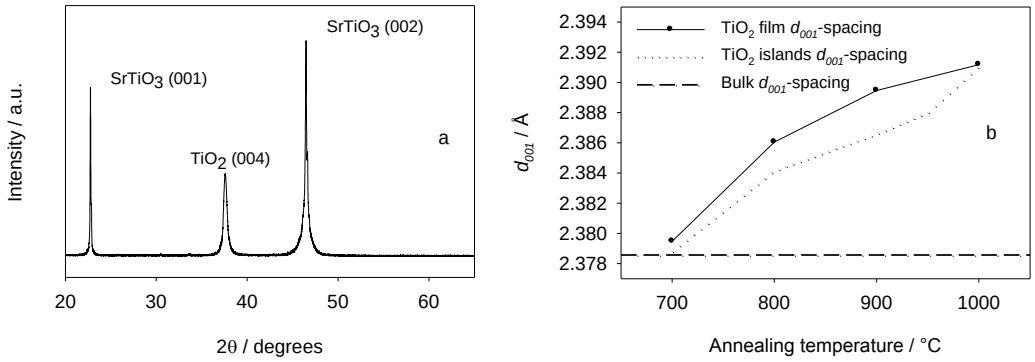


Figure 8.7. (a) Out-of-plane XRD pattern of a TiO_2 film calcined at 1000ºC. (b) Experimentally determined d_{001}-spacing of anatase TiO_2 film and nanoisland at different annealing temperature.

For this sample the anatase d_{001}-spacing also showed a dependence on the annealing temperature, as shown in figure 8.7b. Moreover, the d_{001}-spacing was greater than that found for the TiO_2 nanoisland film at all annealing temperature up to 1000°C, at which temperature the d_{001}-spacings converged on the same value.

8.3.2 Tin incorporation in anatase epitaxial TiO_2

(a) Characterization of the epitaxial growth.

Figure 8.8 shows AFM images of Sn-doped anatase films annealed at 800 ºC with Sn doping concentrations of 5% and 10% as well as an image of an undoped sample. Samples were prepared with 8 dips to ensure the complete covering of the substrate. Incorporation of Sn seems not bring major modifications to the morphology of the films and both images for the doped samples show similar structure to that found for pure TiO_2 films: as with the undoped film, the substrate is completely covered by an array of squared shaped islands with a small size distribution and with edges parallel to the [100] and [010] directions of the $SrTiO_3$. This suggests the existence of the epitaxial

relationship between solid solutions and substrate

$$[100]_{Sn_xTi_{1-x}O_2} || \ [100]_{STO}.$$

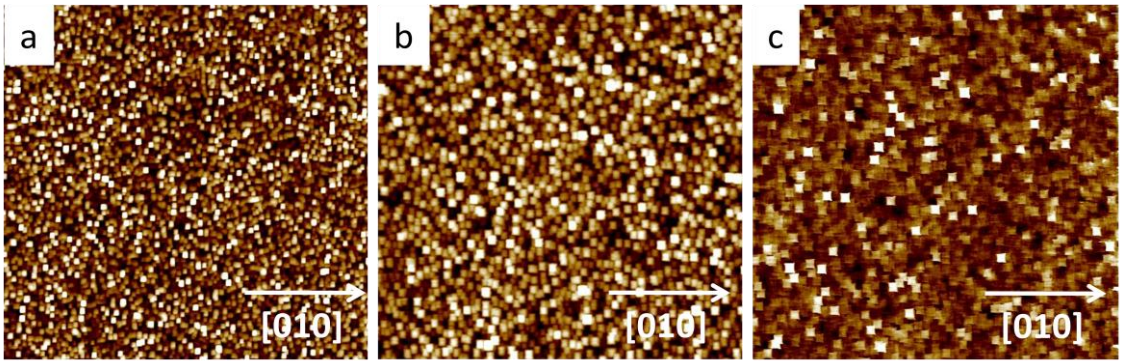


Figure 8.8. 5 μm x 5 μm AFM images of Sn-doped anatase samples calcined at 800°C with doping level of (a) 0% (b) 5% and (c) 10%.

Figure 8.9a shows X-ray diffraction patterns of $Sn_xTi_{1-x}O_2$ films annealed at 800ºC over the range of concentration studied. As for the pure TiO_2 films the patterns all contain (001) and (002) reflections from the $SrTiO_3$ substrate along with an anatase (004) diffraction peak. This indicates exclusive growth of the anatase phase along the c axis for all samples so that substrate and Sn-doped films have the crystal relation

$$(001)_{Sn_xTi_{1-x}O_2} \ || \ (001)_{STO}.$$

A shift of the anatase (004) diffraction peak toward lower 2θ angles with increasing Sn content was observed, which is a consequence of the expansion of the TiO_2 unit cell due to substitutional incorporation of Sn onto Ti sites, as previously discussed in chapters 6 and 7.[20-22] From the position of the anatase (004) diffraction peak, the out of pane lattice parameter *c* was calculated. Figure 8.9b shows a plot of the values of *c* as a function of x for $Sn_xTi_{1-x}O_2$. A monotonic increase of the c parameter upon increasing the Sn concentration suggests effective substitutional incorporation of Sn atoms onto Ti

sites up to a Sn doping level of 15%.

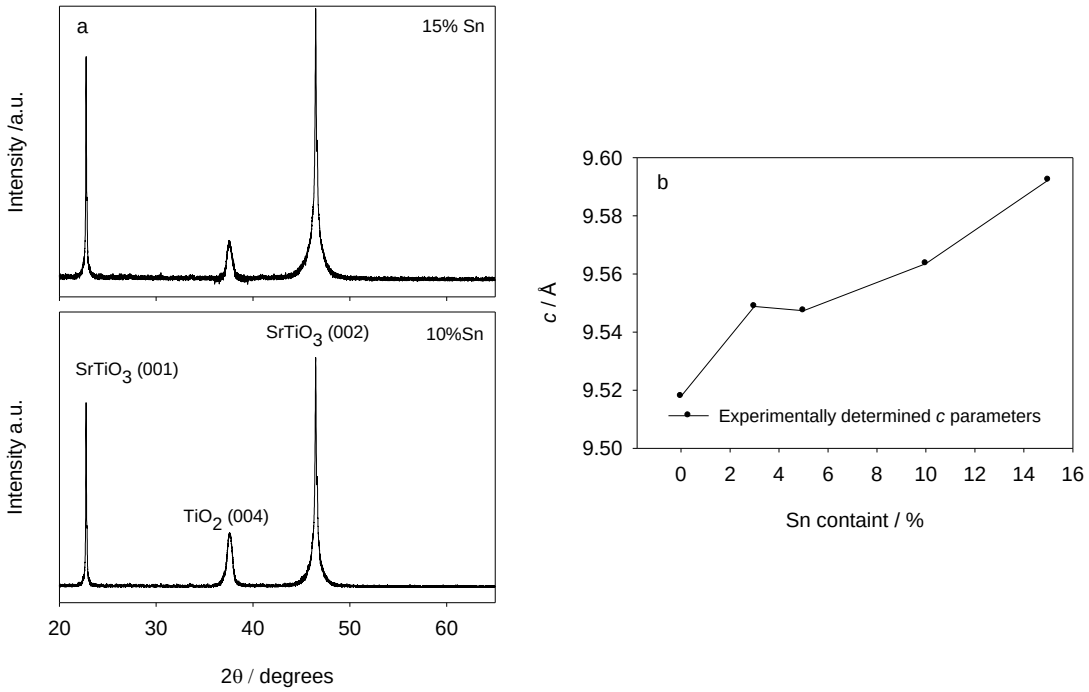


Figure 8.9. (a) out of plane XRD patterns of doped samples with tin concentration of 10% and 15%. (b) experimentally determined anatase *c* parameter of doped samples clacined at 800C in the range of concentration studied

(b) Sn concentrations on anatase $Sn_xTi_{1-x}O_2$ surfaces

As discussed in chapters 6 and 7, high temperature "shake and bake" and sol-gel preparations of free standing rutile $Sn_xTi_{1-x}O_2$ solid solutions yield samples characterized by a pronounced Sn surface segregation as gauged by a Sn 3*d*/Ti 2*p* peak intensity ratio bigger than expected from the bulk doping level. When dealing with powder samples it is however not possible to explore variations in peak intensities with electron take-off angle. This limitation does not apply to epitaxial thin films. Figure 8.10 shows the Sn 3*d* and Ti 2*p* regions in XPS of the 3% Sn-doped anatase TiO_2 at two different electron take off angles. After correction of core line intensities by atomic sensitivity factors, the data for 90° take off angle give an effective surface concentration

x = 0.055 that is just under a factor of 2 higher than the bulk concentration. At 20 ° take off angle a higher value = 0.092 is found. This provides clear evidence that Sn segregation takes place over a length range that is smaller than the electron inelastic mean free path length.

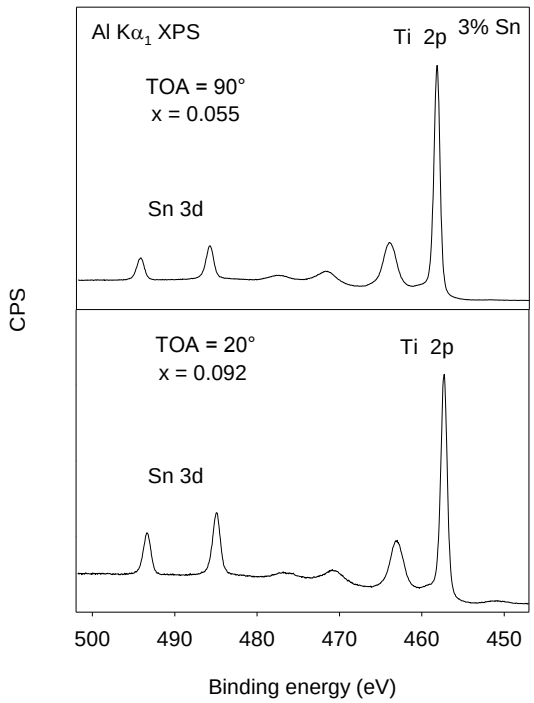


Figure 810. X-Ray photoemission spectra of the Sn 3d and Ti 2p core lines of a 3% Sn-doped sample annealed at 800°C at take off angles of 90°(top panel) and 20°(bottom panel).

(c) Limits of stabilization of epitaxial anatase

Figure 8.11 shows out of plane XRD patterns of samples calcined at 1000 ºC for 1 hour. It can be seen that the intensity of the anatase (004) peak decreases significantly in intensity, and rutile (110) and (111) peaks appear in the pattern. This indicates that the anatase TiO_2 films have begun to transform into rutile which is no longer in a single epitaxial relationship with the substrate.

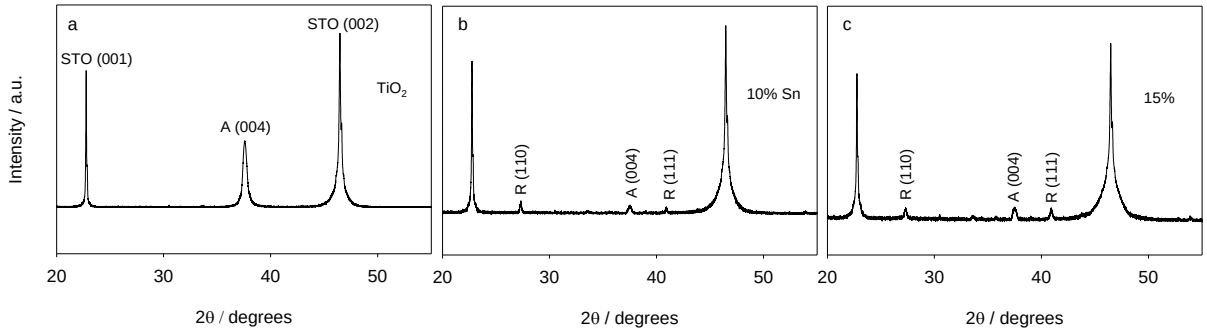


Figure 8.11. Out of pane XRD patterns of Sn-doped samples calcined at 1000°C with doping level of (a) 0% (b) 10% and (c) 15%. A = anatase; R = rutile.

Figure 8.12 shows AFM images of samples with Sn doping levels of 10% and 15% annealed at 1000ºC as well as an image of an undoped sample. In contrast to the undoped sample, the oriented square-shaped islands associated with epitaxial growth transform at 1000°C into an irregular array of randomly oriented grains. This can be taken as a signature of appearance of the rutile phase, whose lattice mismatch is too large to maintain the epitaxial relationship with the substrate.

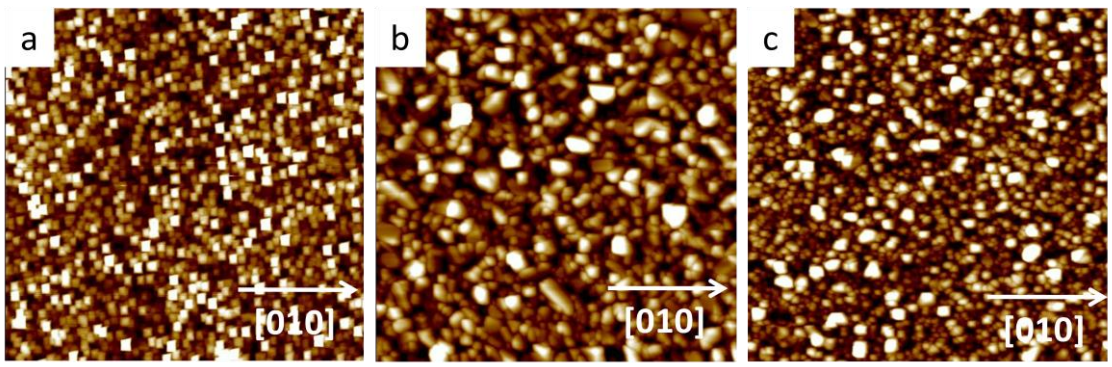


Figure 8.12. 5 μm x 5 μm AFM images of Sn-doped samples calcined at 1000°C with doping level of (a) 0% (b) 10% and (c) 15%.

Overall there are several factors that influence epitaxial stabilization. Based on simple

thermodynamic consierations, the propensity for epitaxial stabilization increases with (a) a decrease of the free energy difference between "metastable" and "stable" phases in the bulk, (b) decreasing film thickness, (c) decrease of epitaxial mismatch between the epilayer phase and the substrate, (d) decreasing shear and elastic moduli of the growing material, and (e) the ability of the growing material to form a periodic multiple-domain structure.[12] Since the lattice constant of $SrTiO_3$ is somewhat larger than the *a* parameter of anatase TiO_2, an increase of the lattice constant due to Sn-doping improve epitaxial matching between the anatase phase and the substrate. However, the intrinsic instability of the Sn-doped anatase is also important in limiting the range of stability of Sn-doped anatase epilayers. Further work is needed in order to clarify how other parameters affect the destabilization of the Sn-doped anatase phase at high temperatures.

8.3.3 The influence of Sn doping on electronic structure of anatase TiO_2: a valence band XPS study.

Valence band photoelectron spectra of TiO_2 and several Sn-doped TiO_2 epitaxial films are shown in figure 8.13. A weak peak at the bottom of the valence band (binding energy 10.5 eV relative to the Fermi energy) grows in intensity with Sn doping in a way similar to that found in spectra of doped rutile samples discussed in chapter 6 and 7. This peak is associated with states with pronounced Sn 5*s* character, hybridised with O 2*p* states.[23-25] Although the free cation Sn^{4+} has an electron configuration $5s^05p^0$, SnO_2 is highly covalent with strong mixing between occupied O 2*p* states and nominally empty Sn 5*s* states, introducing Sn 5*s* character toward the bottom of the valence band. There is also a decrease in spectral weight upon Sn doping at a binding energy of 7.5 eV. This binding energy is where there is maximum Ti 3*d* contribution to the valence band through hybridisation with O 2*p* states.[35] The changes in the valence band spectra

can be linked with the introduction of Sn derived states and the removal of Ti derived states that occurs upon substitutional replacement of Ti by Sn.

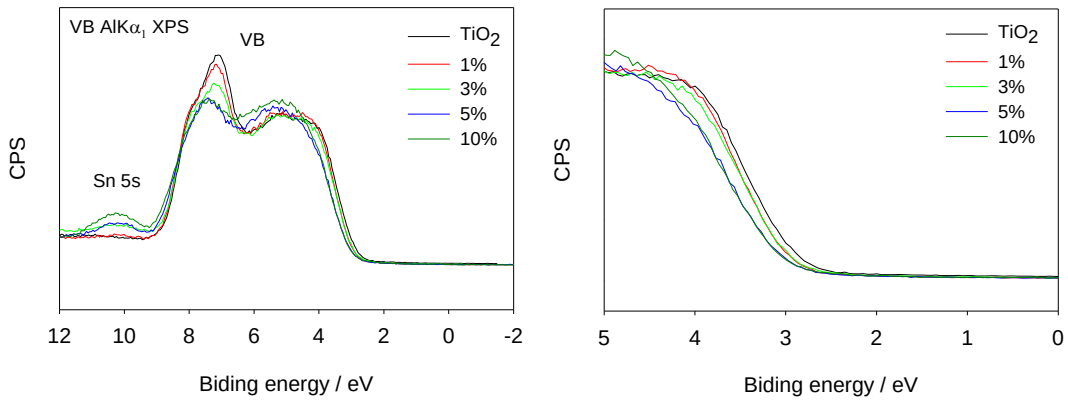


Figure 8.13.Valence band photoelectron spectra of TiO_2 and Sn-doped $_{TiO2}$ samples (Sn concentrations 1%, 3%, 5% and 10%).

The most interesting change on the valence band XPS spectrum upon Sn doping is a shift the valence band onset towards higher binding energy, which increases as the Sn doping level increases. This shift is in the opposite direction to that found in Sn-doped rutile TiO_2. A difference between the two polymorphs of TiO_2 was found by Long *et. al.*[26] who used density functional theory to investigate the electronic structure of Sn doped TiO_2. They found that the band gap increased by 0.06 eV when one Ti ion was replaced by Sn in an anatase $2 \times 2 \times 2$ supercell (i.e. 1 Ti in every 16) to give a material with 6.25 % Sn doping. In contrast, when a similar substitution was made in a rutile supercell, there was a decrease of the band gap of 0.12 eV as discussed previously in chapter 6 and 7.

8.4 Conclusions

It has been developed a simple a low cost sol-gel method based on dip coating to

prepare epitaxial TiO_2-anatase (001) thin films on $SrTiO_3$(001). Very thin films of TiO_2 prepared using this method suffered strain-induced dewetting upon annealing at high temperatures, that leads to the formation of self-assembled square-shaped nanostructure. Unlike free standing polycrystalline anatase, where crystallite morphology is dominated by low energy (101) surfaces, the (001) oriented islands exhibit (103) side facets.

The work reported in this chapter establishes that epitaxial stabilization of the anatase phase of TiO_2 films grown on $SrTiO_3$ (001) substrate is allows preparation of Sn-doped anatase TiO_2 films with Sn doping levels up to 15% that are stable to temperatures of at least 800 °C. Although free standing polycrystalline $Sn_xTi_{1-x}O_2$ samples are stable only in the rutile phase, films on STO (001) films grow exclusively in the anatase phase with the epitaxial relationship $(001)_{TiO_2} \,||\, (001)_{STO}$ and $[100]_{TiO_2} \,||\, [100]_{STO}$. This allowed the experimental study of the effects of Sn-doping on electronic structure of anatase TiO_2 by means of X-ray photoelectron spectroscopy. Valence band photoemission spectroscopy showed that, unlike the case of the rutile phase, Sn-doping in anatase TiO_2 leads to a monotonic shift of the valence band maximum towards higher binding energy. This arises from an increase of the band gap with Sn-doping, in agreement with theoretical calculations.

Two factors must be considered to understand the differences between rutile and anatase polymorphs. On the one hand the valence band in SnO_2 lies further below the vacuum level than in TiO_2 and pure electronic effects will tend to lead to bandgap widening with Sn doping in TiO_2. On the other hand the internal strain associated with replacement of Ti by larger Sn cations will lead to expansion of the lattice. In general lattice expansion leads to a reduction in the bandgaps of oxides as both the Madelung

potential and the strengths of bonding interactions are reduced. It may be further speculated that these strain induced effects predominate in Sn doping of rutile at low doping levels but are less important in the anatase phase owing to the initially greater volume of the unit cell. Further theoretical work is needed to explore these ideas further.

8.5 References

(1) Mahanty, S.; Roy, S.; Sen, S. *Journal of Crystal Growth* **2004**, *261*, 77.

(2) Cao, Y. Q.; He, T.; Chen, Y. M.; Cao, Y. A. *Journal of Physical Chemistry C* **2010**, *114*, 3627.

(3) Sui, R. H.; Young, J. L.; Berlinguette, C. P. *Journal of Materials Chemistry* **2010**, *20*, 498.

(4) Cao, Y. Q.; He, T.; Zhao, L. S.; Wang, E. J.; Yang, W. S.; Cao, Y. A. *Journal of Physical Chemistry C* **2009**, *113*, 18121.

(5) Diebold, U. *Surface Science Reports* **2003**, *48*, 53.

(6) Jellison, G. E.; Boatner, L. A.; Budai, J. D.; Jeong, B. S.; Norton, D. P. *Journal of Applied Physics* **2003**, *93*, 9537.

(7) Murakami, M.; Matsumoto, Y.; Nakajima, K.; Makino, T.; Segawa, Y.; Chikyow, T.; Ahmet, P.; Kawasaki, M.; Koinuma, H. *Applied Physics Letters* **2001**, *78*, 2664.

(8) Park, B. H.; Huang, J. Y.; Li, L. S.; Jia, Q. X. *Applied Physics Letters* **2002**, *80*, 1174.

(9) Zhang, Z. M. *Journal of Materials Research* **2005**, *20*, 292.

(10) Chan, K. Y. S.; Goh, G. K. L. *Journal of the Electrochemical Society* **2009**, *156*, D231.

(11) Jung, H. S.; Lee, J. K.; Lee, J.; Kang, B. S.; Jia, Q.; Nastasi, M. *Journal of Physical Chemistry C* **2008**, *112*, 4205.

(12) Gorbenko, O. Y.; Samoilenkov, S. V.; Graboy, I. E.; Kaul, A. R. *Chemistry of Materials* **2002**, *14*, 4026.

(13) Coll, M.; Gazquez, J.; Pomar, A.; Puig, T.; Sandiumenge, F.; Obradors, X. *Physical Review B* **2006**, *73*, 8.

(14) Burke, S. A.; Ji, W.; Mativetsky, J. M.; Topple, J. M.; Fostner, S.; Gao, H. J.; Guo, H.; Grutter, P. *Physical Review Letters* **2008**, *100*, 4.

(15) Burke, S. A.; Topple, J. M.; Grutter, P. *Journal of Physics-Condensed Matter* **2009**, *21*, 423101 .

(16) Herman, G. S.; Sievers, M. R.; Gao, Y. *Physical Review Letters* **2000**, *84*, 3354.

(17) Gao, Y.; Elder, S. A. *Materials Letters* **2000**, *44*, 228.

(18) Olson, C. L.; Nelson, J.; Islam, M. S. *The Journal of Physical Chemistry B*

2006, *110*, 9995.

(19) Zhao, Z. Y.; Li, Z. S.; Zou, Z. G. *Journal of Physics-Condensed Matter* **2010**, *22*, 175008 .

(20) Hirata, T.; Ishioka, K.; Kitajima, M.; Doi, H. *Physical Review B* **1996**, *53*, 8442.

(21) Lin, J.; Yu, J. C.; Lo, D.; Lam, S. K. *Journal of Catalysis* **1999**, *183*, 368.

(22) Uchiyama, H.; Imai, H. *Chemical Communication* **2005**, 6014.

(23) Egdell, R. G.; Rebane, J.; Walker, T. J.; Law, D. S. L. *Phys. Rev. B* **1999**, *59*, 1792.

(24) Cox, P. A.; Egdell, R. G.; Harding, C.; Patterson, W. R.; Tavener, P. J. *Surface Science* **1982**, *123*, 179.

(25) Egdell, R. G.; Walker, T. J.; Beamson, G. *Journal of Electron Spectroscopy and Related Phenomena* **2003**, *128*, 59.

(26) Long, R.; Dai, Y.; Huang, B. *Journal of Physical Chemistry C* **2009**, *113*, 650.

Chapter 9: Concluding remarks

This thesis has attempted to further understanding of the mechanisms of visible light absorption in doped TiO_2 and to assess the potential of these doped materials as visible light photocatalysts. We have combined photoelectron spectroscopy with a series of other spectroscopic techniques and also performed simple photocatalytic tests. Both anion and cation doping was explored. Specifically nitrogen, rhodium and tin doping were studied. In this chapter an overview of the results and suggestions for further studies are given.

9.1 Visible light absorption versus visible light photocatalysis

Absorption of visible light by a photocatalyst is of course crucial for it to be active under visible light irradiation. However, transfer of electrons and holes generated by photoexcitation to species adsorbed on the solid is as important as the photoexcitation step itself for the photocatalytic process.[1-2]

Nitrogen-doped TiO_2 samples studied in chapter 4 had both visible light absorption and photocatalytic activity. It was determined that a paramagnetic nitrogen species NO_O^x is a product of photoexcitation of $NO_O^{'}$. The fact that the paramagnetic species can be detected at all can be correlated to the photocatalytic activity. The steady state concentration of electrons in the conduction band and the NO_O^x holes seen in EPR will be inversely related to the electron–hole recombination rate. The photocatalytic activity also depends on the steady state concentration of electrons and holes under visible light illumination, thus providing a link between the intensity of the EPR signal and the photocatalytic performance. Indeed, the concentration of the paramagnetic nitrogen

species could be well correlated to the photocatalytic performance of the samples. On the other hand, for Rh/Sb codoped TiO_2 paramagnetic species the product of the photoexcitation cannot be detected by EPR experiments.[3] This suggests that the recombination rate for N-doped samples is lower than that for Rh/Sb-codoped samples. Despite the fact that visible light absorption induced by doping with transition metals may be stronger than that obtained by doping with nitrogen, these results suggests that the case of the anionic doping may be more beneficial for visible light photocatalysis.

For the Sn-doped TiO_2 system studied in chapters 6 to 8, a tail of states in the bandgap was attributed to surface states arising from Sn^{2+} ions in surface and grain boundary interface sites and the associated lone-pair like O 2*p* + Sn 5*s* + Sn 5*p* hybrid state. Photoexcitation of electrons from this state into the conduction band occurs in the visible region and the electron / hole pair generated can take part of redox reactions with species adsorbed on the solid surface. As describe in chapter 7, Sn-doped TiO_2 samples prepared by sol-gel methods had a higher photocatalytic activity than that of the N-doped TiO_2 samples studied in chapter 4. The location of the centre responsible of the visible absorption at the surface of the solid may be the key for a higher photocatalytic performance. As the electron / hole pairs are formed on the surface of the doped TiO_2, they are readily available for photocatalysis so that recombination effects are less problematic. This result shows the importance of the availability of the photogenerated electron / hole pairs at the surface of the solid to promote redox reactions. Sn-doped TiO_2 had the weakest absorption in the visible region of all the samples studied, and yet was shown to have the best photocatalytic performance. It seems to be desirable to enhance the doping close to the surface of the solid in the synthesis of doped titania photocatalysts.

9.2 Areas for future work

The research performed in this thesis addressed important fundamental issues regarding visible light absorption and photocatalysis of doped titania-based materials. It has been shown how an understanding of the mechanism of visible light absorption can lead to the preparation of solids with imporoved photocatalytic properties. There are however some practical considerations on the development of catalyst for practical applications. One of the major objectives of research in heterogeneous catalysis is the correlation of catalytic performance with the structure and composition of the catalyst.[4] Photocatalysis of TiO_2 doped with transition metals has been studied for a very long time and well-established theories on the photocatalytic mechanism have been developed.[2] Similarly, N-doped TiO_2 is a system that has gained much attention since it was first suggested to be a visible light responding photocatalyst.[5] EPR studies and detailed analysis of the photocatalytic decomposition of dyes have led to a reasonable understanding of the underlying photocatalytic mechanisms on N-doped TiO_2.[6-7] On the other hand, Sn-doped TiO_2 had never been reported as a potential visible light photocatalyst and there is still scope for further research in the practical development of this system. In particular a new project in the Egdell group is in exploration of Sn-doped TiO_2 as a catalyst for inactivation of Escherichia coli and other bacteria under irradiation with visible light: previous work in this field has been mainly restricted to ultraviolet photoactivity[8-14]. Initial results using a simple slurry reactor are encouraging.

The method for the preparation of TiO_2 epitaxial films developed in this thesis provides a cheap and convenient way of preparing thin film samples. The epitaxial growth of oxide like SnO_2 and In_2O_3 by sol-gel methods is under further investigation in the

Egdell group.

The sol-gel preparation method is not only useful for fundamental materials science research but also for practical applications in areas such as water purification. Indeed some preliminary investigations of "upscaling" were made. Polycrystalline films of Sn-doped TiO_2 on a Ti substrate with a size of 10 cm × 10 cm were successfully prepared using the dip coating procedure. These films were then subject to a field test carried out by Abengoa Solar, who operate a research facility south of Seville in Spain. The test involved the photocatalytic degradation of methyl orange dye using solar irradiation as the light source. The Abengoa test system is shown in the photographs below.

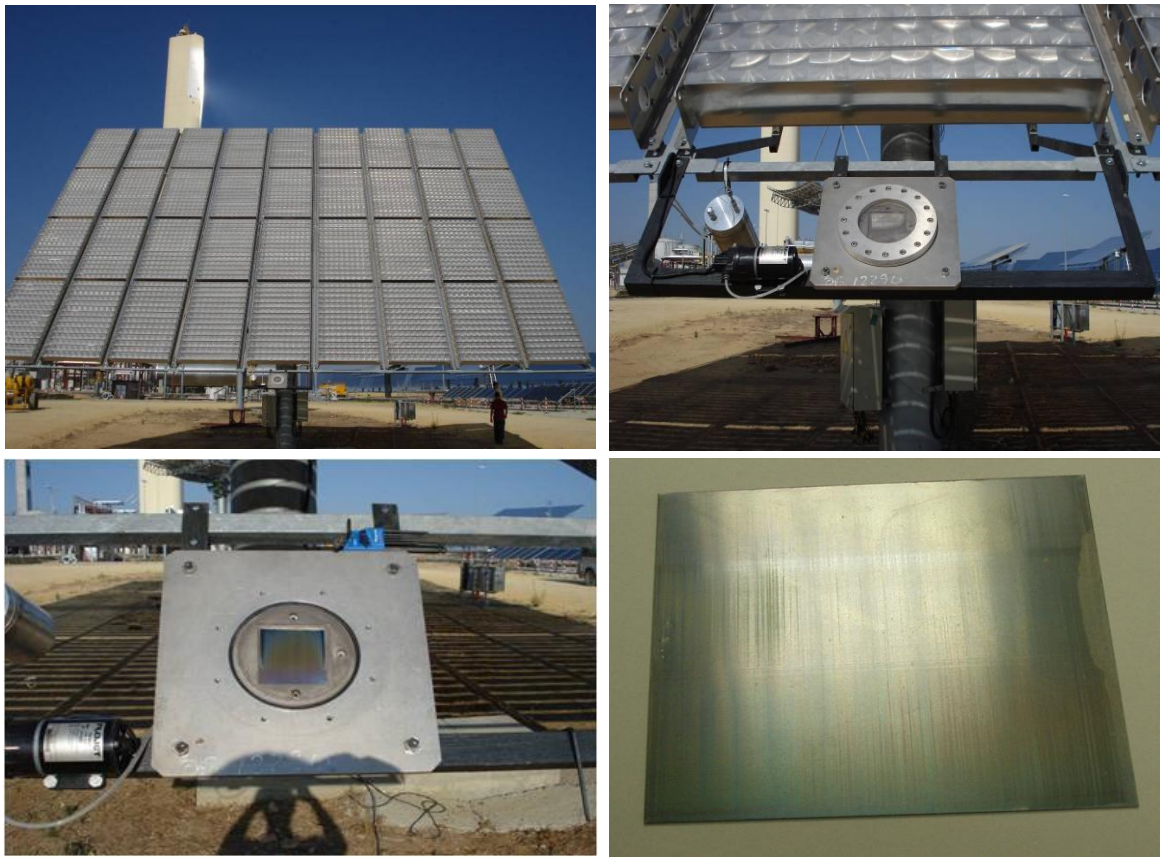


Figure 9.1 Photographs of field test apparatus at Abengoa Solar facility near Seville. The bottom right photograph shows a 10 cm × 10 cm Sn-doped TiO_2 film prepared by dip coating a sheet of Ti metal.

A cell containing the 10 cm × 10 cm film is attached to a solar tracker device otherwise used to test solar cells and a solution of methyl orange is pumped across the film in a flow system. The tracker is equipped with a power meter that records the solar power continuously. Figure 9.2 shows the irradiation energy as a function of time over a 5 days test period. The solar irradiance varies smoothly on a 24 hour cycle with a maximum power of about 1000 W/m^2 at midday – downward dips correspond to the (few) occasions when cloud passes across the sun.

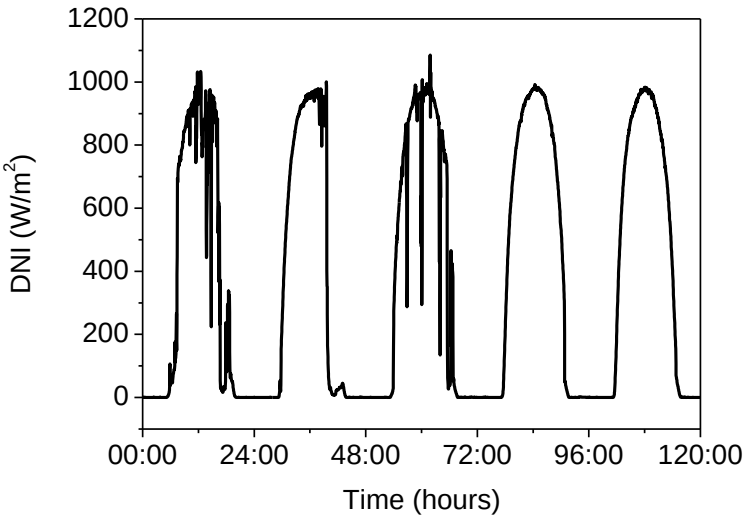


Figure 9.2. Solar power density as a function of time at the Abengoa installation near Seville, Spain.

Figure 9.3 shows the concentration of the dye as a function of irradiation energy. The encouraging results show that Sn-doped TiO_2 photocatalysts are active under field conditions of real solar irradiation. This vindicates the laboratory-based studies of this system reported in chapter 7. It is also clear that preparation of thin films by sol gel methods is easily scalable. Abengoa are investigating further up-scaling for waste water treatment.

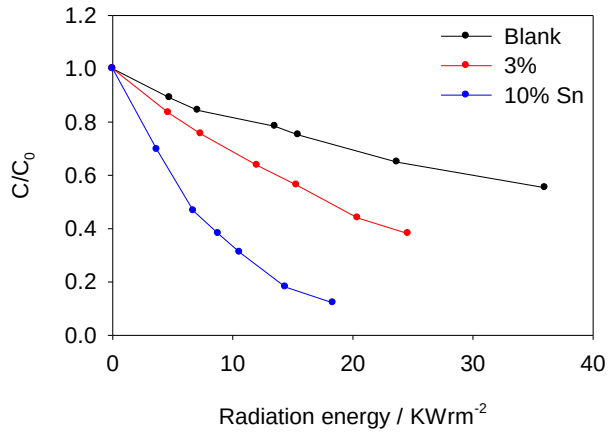


Figure 9.3. Photocatalytic degradation of methyl orange dye during a field test near Seville as a function of the total energy of solar radiation falling on Sn doped TiO_2 films. The dip coated sol-gel films had been annealed at 600 °C for 1 hour. The blank result was obtained using a nominally uncoated sheet of Ti metal, although it should be realised that this will be coated with native oxide.

9.3 References

(1) Linsebigler, A. L.; Lu, G. Q.; Yates, J. T. *Chemical Reviews* **1995**, *95*, 735.

(2) Ni, M.; Leung, M. K. H.; Leung, D. Y. C.; Sumathy, K. *Renewable & Sustainable Energy Reviews* **2007**, *11*, 401.

(3) Niishiro, R.; Konta, R.; Kato, H.; Chun, W. J.; Asakura, K.; Kudo, A. *J. Phys. Chem. C* **2007**, *111*, 17420.

(4) Bond, G. C. *Catal. Rev.-Sci. Eng.* **2008**, *50*, 532.

(5) Asahi, R.; Morikawa, T.; Ohwaki, T.; Aoki, K.; Taga, Y. *Science* **2001**, *293*, 269.

(6) Livraghi, S.; Paganini, M. C.; Giamello, E.; Selloni, A.; Di Valentin, C.; Pacchioni, G. *Journal of the American Chemical Society* **2006**, *128*, 15666.

(7) Wang, J.; Tafen, D. N.; Lewis, J. P.; Hong, Z. L.; Manivannan, A.; Zhi, M. J.; Li, M.; Wu, N. Q. *Journal of the American Chemical Society* **2009**, *131*, 12290.

(8) Sontakke, S.; Modak, J.; Madras, G. *Chem. Eng. J.* **2010**, *165*, 225.

(9) van Grieken, R.; Marugan, J.; Pablos, C.; Furones, L.; Lopez, A. *Applied Catalysis B-Environmental* **2010**, *100*, 212.

(10) Chen, C. Y.; Wu, L. C.; Chen, H. Y.; Chung, Y. C. *Water Air Soil Pollut.* **2010**, *212*, 231.

(11) Liu, P.; Duan, W. L.; Wang, Q. S. I.; Li, X. *Colloids and Surfaces B-Biointerfaces* **2010**, *78*, 171.

(12) Backhaus, K.; Marugan, J.; van Grieken, R.; Sordo, C. *Water Sci. Technol.* **2010**, *61*, 2355.

(13) Sordo, C.; Van Grieken, R.; Marugan, J.; Fernandez-Ibanez, P. *Water Sci. Technol.* **2010**, *61*, 507.

(14) Alrousan, D. M. A.; Dunlop, P. S. M.; McMurray, T. A.; Byrne, J. A. *Water Res.* **2009**, *43*, 47.